

**USING INDUCED SIGNALS TO DEVELOP A POSITION-SENSITIVE
MICROCHANNEL PLATE DETECTOR**

Bryan Blake Wiggins

Submitted to the faculty of the University Graduate School in partial fulfillment of the requirements for the degree Doctor of Philosophy in the Department of Chemistry,
Indiana University
December 2017

ProQuest Number: 10686059

All rights reserved

INFORMATION TO ALL USERS

The quality of this reproduction is dependent upon the quality of the copy submitted.

In the unlikely event that the author did not send a complete manuscript and there are missing pages, these will be noted. Also, if material had to be removed, a note will indicate the deletion.



ProQuest 10686059

Published by ProQuest LLC (2017). Copyright of the Dissertation is held by the Author.

All rights reserved.

This work is protected against unauthorized copying under Title 17, United States Code
Microform Edition © ProQuest LLC.

ProQuest LLC.
789 East Eisenhower Parkway
P.O. Box 1346
Ann Arbor, MI 48106 – 1346

Accepted by the Graduate Faculty, Indiana University, in partial fulfillment of the requirements for the degree of Doctor of Philosophy.

Doctoral Committee:

Romualdo T. de Souza, Ph.D., Chair

James P. Reilly, Ph.D.

Gary M. Hieftje, Ph.D.

Stephen C. Jacobson, Ph.D.

December 6, 2017

Copyright 2017
Bryan Blake Wiggins

To the bright memory of my best friend Michael Peltier, whose light continues to inspire
my curiosity.

Acknowledgements

Like a dwarf standing on the shoulders of giants, so have my advances to the field of imaging been made. These contributions would not have been possible without the guidance by my research advisor Dr. Romualdo de Souza who took in a nascent scientist and taught him to really “go for the jugular” when approaching a scientific problem. I have had the pleasure of learning so much about analysis and programming from Dr. Sylvie Hudan, wire winding from Keith Solberg and Alan Eads, and several scientific debates with Dr. Varinderjit Singh and Justin Vadas. I would like to thank the IU nuclear chemistry group in general, but especially Eric Richardson, Davinder Siwal, and Zarya deSouza for directly contributing to the work presented. All of my detector construction and electronics development of my novel detector were performed at the Mechanical Instrument Services and Electronic Instrument Services. I especially want to thank Tom Smith and Jeremy Boshears for all of their training in mechanical design. Andy Alexander designed several circuit boards for my project and Dave Bancroft spearheaded the development of a new data acquisition system for our neutron imaging application. I am reminded of the phrase “that it takes a village”, which is truly the case in the sciences. I appreciate all of the work of my village not only in the results I will show but also in their development in me as a scientist. I would also like to point out all the emotional support given to me by my lovely wife, Katie Wiggins, and from all of my friends.

Bryan Blake Wiggins
USING INDUCED SIGNALS TO DEVELOP A POSITION-SENSITIVE
MICROCHANNEL PLATE DETECTOR

A novel concept to provide position-sensitivity to a microchannel plate (MCP) is described. While several designs exist to make MCPs position sensitive, all these designs are based upon collection of the electrons. In contrast, this approach utilizes an induced signal as the electron cloud emanates from an MCP and passes a wire plane. We demonstrate the validity of the concept by constructing a device that provides single electron detection with 98 μm position resolution (FWHM) over an area of 50 mm \times 50 mm. The characteristics of the detector are described through both bench-top tests and simulation. After characterization of the detector, the sense wire detector was utilized for slow-neutron radiography. Furthermore, we utilized our knowledge of position-sensitive techniques to realize a beam-imaging MCP detector useful for radioactive beam facilities.

Romualdo T. de Souza, Ph.D., Chair

James P. Reilly, Ph.D.

Gary M. Hieftje, Ph.D.

Stephen C. Jacobson, Ph.D.

Contents

| | |
|------------------------------------------------------------------------------------------------|-------------|
| Acceptance Page | ii |
| Copyright | iii |
| Dedication | iv |
| Acknowledgements | v |
| Abstract | vi |
| List of Figures | x |
| List of Tables | xiii |
| Abbreviations | xiv |
| 1 Detection of photons, electrons, and ions by MCPs | 1 |
| 1.1 Introduction to the induced signal approach | 1 |
| 1.2 Motivation for a MCP detector | 3 |
| 1.3 Detection of photons, electrons, and ions by MCPs | 4 |
| 1.4 The fundamental principles of image intensifiers, electron multipliers, and MCPs | 5 |
| 1.5 Motivation for a PS-MCP | 10 |
| 1.6 Existing approaches to position sensitivity to MCP detectors | 16 |
| 1.6.1 Multi-anode detector | 18 |
| 1.6.2 Cross-strip anode detector | 20 |
| 1.6.3 Resistive anode detector | 21 |
| 1.6.4 Medipix2/Timepix CMOS detector | 23 |
| 1.6.5 Helical delay-line detector | 24 |
| 1.6.6 Conclusions | 26 |
| 2 Exploring the Spatial Resolution of PS-MCP Detectors | 28 |
| 2.1 The induced signal approach | 28 |
| 2.1.1 Sensing an electron avalanche in a gas detector | 28 |
| 2.1.2 The MCP-SW detector v1.0 | 31 |
| 2.1.3 Individual wire readout | 37 |
| 2.1.4 Design and construction of a wire winder and vacuum test station | 38 |
| 2.1.4.1 Wire winder | 39 |
| 2.1.4.2 Vacuum test station | 42 |
| 2.1.5 Achieving high spatial resolution with the MCP-SW detector v2.0 | 47 |
| 2.1.5.1 Experimental setup and description of MCP-SW v2.0 . . | 47 |

| | | |
|----------|-----------------------------------------------------------------------------------------|------------|
| 2.1.5.2 | Measuring the spatial resolution of the MCP-SW detector | 52 |
| 2.1.5.3 | Measuring the spatial resolution of the MCP-SW detector with 5 and 2 GS/s digitization | 58 |
| 2.1.5.4 | Measuring the spatial resolution of the MCP-SW detector using 0.5ns/tap delay boards | 61 |
| 2.2 | Resistive anode technology | 62 |
| 2.2.1 | Prior work with resistive anodes | 62 |
| 2.2.2 | Spatial resolution with the standard charge division method | 63 |
| 2.2.3 | Using pulse shape analysis to improve the spatial resolution | 73 |
| 2.2.3.1 | Experimental setup | 73 |
| 2.2.3.2 | Signal risetime analysis | 75 |
| 2.3 | The multi-strip anode | 80 |
| 3 | Some applications of position-sensitive MCP detectors | 85 |
| 3.1 | Slow neutron radiography | 85 |
| 3.1.1 | Motivation | 85 |
| 3.1.2 | Overview of modern neutron radiography | 90 |
| 3.1.3 | Radiography vacuum station | 93 |
| 3.1.4 | Experimental setup | 94 |
| 3.1.5 | The neutron source | 96 |
| 3.1.6 | First neutron radiographs | 100 |
| 3.1.7 | Neutron data acquisition | 102 |
| 3.1.8 | Second measurements of neutron radiographs | 107 |
| 3.2 | Beam Imaging using a position-sensitive E×B detector | 113 |
| 3.2.1 | Motivation | 113 |
| 3.2.2 | Experimental setup | 114 |
| 3.2.3 | Measuring the spatial resolution of the E×B MCP detector | 116 |
| 3.2.4 | Intrinsic spatial resolution of E×B MCP detector | 120 |
| 3.2.5 | Approved experiments using the E×B MCP detector | 121 |
| 4 | Simulations to understand detector performance | 123 |
| 4.1 | Geometric factors impacting the MCP electron-cloud size | 123 |
| 4.2 | Calculating the growth of the MCP electron cloud | 125 |
| 4.3 | Factors influencing the spatial resolution of the MCP-SW detector | 129 |
| 4.4 | Understanding the spatial resolution of the MCP-SW detector with a differential readout | 132 |
| 4.5 | Simulating the spatial resolution of the E×B detector | 134 |
| 4.5.1 | Mapping the magnetic field | 134 |
| 4.5.2 | Simulating the spatial resolution | 137 |
| 5 | Conclusions | 139 |
| 5.1 | The MCP-SW detector | 139 |

| | | |
|----------|--------------------------------------------------|------------|
| 5.2 | The MCP-RA detector | 141 |
| 5.3 | Beam imaging | 142 |
| 5.4 | Neutron radiography | 144 |
| 5.5 | Outlook | 145 |
| | | |
| A | Signal processing for the resistive anode | 148 |
| B | Wire winding manual | 152 |
| B.1 | To use the wire winder | 152 |
| B.2 | Troubleshooting the wire winder | 161 |
| C | Delay board characterization | 163 |
| D | Electronics Diagrams | 168 |
| E | Program directories | 174 |
| | | |
| | Bibliography | 181 |
| | Curriculum Vitae | |

List of Figures

| | | |
|------|----------------------------------------------------------------|----|
| 1.1 | Induced signal and anode waveform | 2 |
| 1.2 | MCP operation | 6 |
| 1.3 | MCP fabrication | 10 |
| 1.4 | ALS bunch distribution | 12 |
| 1.5 | Resolution vs cost for PS-MCPs | 16 |
| 1.6 | Multi-strip anode schematic | 19 |
| 1.7 | Cross-strip anode schematic | 21 |
| 1.8 | Resistive anode schematic | 22 |
| 1.9 | Medipix2/Timepix schematic | 23 |
| 1.10 | Helical delay line anode schematic | 25 |
| | | |
| 2.1 | Schematic diagram of a PPAC/MWPC detector | 29 |
| 2.2 | Cartoon of delay line concept | 30 |
| 2.3 | Induced signal approach concept | 32 |
| 2.4 | MCP-SW detector v1.0 | 33 |
| 2.5 | Induced signal waveforms | 34 |
| 2.6 | Photograph of mask | 34 |
| 2.7 | Time correlation for MCP-SW v1.0 | 35 |
| 2.8 | FFT spectrum for induced signals | 36 |
| 2.9 | Position spectrum for MCP-SW v1.0 | 36 |
| 2.10 | Inherent induced signal waveforms | 37 |
| 2.11 | Wire winder | 39 |
| 2.12 | Sense wire PCB | 41 |
| 2.13 | Vacuum chamber schematic | 42 |
| 2.14 | Vacuum chamber CAD and photo | 43 |
| 2.15 | Cryopump cooldown time | 44 |
| 2.16 | Vacuum station pumpdown time | 45 |
| 2.17 | Vacuum station resting block | 46 |
| 2.18 | PS-MCP detector on resting block | 46 |
| 2.19 | Cartoon of MCP-SW concept | 48 |
| 2.20 | MCP-SW v2.0 setup | 49 |
| 2.21 | Photograph of SW PCB with delay line readout | 49 |
| 2.22 | Raw position spectrum for MCP-SW v2.0 detector | 53 |
| 2.23 | Total charge distribution for MCP-SW v2.0 detector | 54 |
| 2.24 | Digital signal processing for MCP-SW v2.0 detector | 56 |
| 2.25 | Optimized position spectrum for MCP-SW v2.0 detector | 57 |
| 2.26 | Waveforms of middle events for each delay board | 59 |
| 2.27 | Waveforms of edge events for each delay board | 59 |
| 2.28 | Linearity improvements using new delay boards | 60 |

| | | |
|------|--------------------------------------------------------|-----|
| 2.29 | Resolution using new delay boards | 60 |
| 2.30 | MCP-RA detector setup | 64 |
| 2.31 | Total charge distribution for MCP-RA | 65 |
| 2.32 | Raw position spectrum for MCP-RA detector | 66 |
| 2.33 | Charge correlation for MCP-RA | 67 |
| 2.34 | RA schematic | 67 |
| 2.35 | Resolution vs position for MCP-RA | 69 |
| 2.36 | Resolution vs ΔV for MCP-RA | 71 |
| 2.37 | Schematic of RA with waveforms | 75 |
| 2.38 | Risetime correlation for MCP-RA | 76 |
| 2.39 | Risetime vs position for MCP-RA | 78 |
| 2.40 | Resolution vs slit no. for MCP-RA | 80 |
| 2.41 | MA with delay line schematic | 80 |
| 2.42 | MA photograph | 81 |
| 2.43 | MCP-MA detector setup | 82 |
| 2.44 | Position spectrum for MCP-MA | 83 |
| | | |
| 3.1 | Neutron radiograph of a bullet | 89 |
| 3.2 | RVS schematic | 92 |
| 3.3 | RVS photograph | 94 |
| 3.4 | Setup for MCP-SW for neutron radiography | 95 |
| 3.5 | Neutron capture in boron-MCP | 95 |
| 3.6 | CAD of the LENS floor plan | 98 |
| 3.7 | LENS beam structure | 99 |
| 3.8 | First 2D image with slow neutrons | 100 |
| 3.9 | Neutron data acquisition | 102 |
| 3.10 | NDAQ flowchart | 105 |
| 3.11 | 2D image using an α -source | 106 |
| 3.12 | Microscope image of Cd mask | 107 |
| 3.13 | 2D raw and gated images for NRad2017 | 108 |
| 3.14 | 1D neutron radiograph | 109 |
| 3.15 | MCP-E \times B setup | 114 |
| 3.16 | Time correlation for MCP-E \times B | 116 |
| 3.17 | Position spectrum for MCP-E \times B | 118 |
| 3.18 | Resolution vs position for MCP-E \times B | 119 |
| 3.19 | Position spectrum of central slit for MCP-E \times B | 120 |
| | | |
| 4.1 | Simulated activated pores for MCP | 124 |
| 4.2 | Radial growth vs time for MCP | 127 |
| 4.3 | Charge density distribution for MCP | 128 |
| 4.4 | Simulated spatial resolution for MCP-SW | 131 |
| 4.5 | Maxwell 2D simulations for MCP-SW | 132 |

| | | |
|------|---------------------------------------------------------------------|-----|
| 4.6 | Measured magnetic field for MCP-E×B | 135 |
| 4.7 | SIMION simulation for MCP-E×B | 136 |
| 4.8 | SIMION simulations for MCP-E×B | 137 |
| | | |
| B.1 | Wire winder components | 152 |
| B.2 | How tape should be overlaid | 153 |
| B.3 | How tape should be overlaid | 153 |
| B.4 | Tensioner | 156 |
| B.5 | Mountable Plate | 157 |
| B.6 | Affixing the wire | 157 |
| B.7 | Epoxy placement | 159 |
| | | |
| C.1 | Time delay for delay boards | 163 |
| C.2 | Risetime Determination for delay board characterization | 164 |
| C.3 | Risetime for delay boards | 164 |
| C.4 | Attenuation for delay boards | 165 |
| C.5 | Time delay for delay + SW boards | 166 |
| C.6 | Risetime for delay + SW boards | 166 |
| C.7 | Attenuation for delay + SW boards | 167 |
| | | |
| D.1 | Electronics diagram for MCP-SW 2GS/s | 168 |
| D.2 | Electronics diagram for MCP-SW 10GS/s | 169 |
| D.3 | Electronics diagram for MCP-SW 20GS/s | 169 |
| D.4 | Electronics diagram for MCP-RA charge division | 170 |
| D.5 | Electronics diagram for MCP-RA pulse shape analysis | 170 |
| D.6 | Electronics diagram for MCP-MAnode | 171 |
| D.7 | Electronics diagram for neutron radiography 2016 run | 171 |
| D.8 | Electronics diagram for neutron DAQ pulser testing | 172 |
| D.9 | Electronics diagram for neutron radiography 2017 run | 172 |
| D.10 | Electronics diagram for MCP-E×B | 173 |
| D.11 | Electronics diagram for 50ns delay board characterization | 173 |

List of Tables

| | | |
|-----|-----------------------------------------------------------------------------|-----|
| 1.1 | Detection efficiencies for MCPs | 5 |
| 1.2 | Composition of MCP glass | 8 |
| 1.3 | Advantages and Disadvantages of PS-MCP detectors | 17 |
| 2.1 | Spatial resolution summary for MCP-SW v1.0 | 35 |
| 2.2 | Spatial resolution summary for MCP-SW v2.0 | 56 |
| 3.1 | Detection efficiencies for thermal, cold, and ultra-cold neutrons | 89 |
| 3.2 | Spatial resolution summary for MCP-SW in neutron radiography | 111 |
| 3.3 | Spatial resolution summary for MCP-E×B | 120 |
| 5.1 | Spatial resolution summary of PS-MCP detectors | 139 |

Abbreviations

| | |
|---------------|-------------------------------------------------------------------------------------------------|
| ALS | A dvanced L ight S ource |
| ADC | A nalog-to- D igital C onverter |
| ASIC | A pplication S pecific I ntegrated C ircuit |
| AT-TPC | A ctive T arget- T ime P rojection C hamber |
| CANS | C ompact A ccelerator-driven N eutron S ources |
| CCD | C harge- C oupled D evice |
| CFD | C onstant F raction D iscriminator |
| CSA | C harge S ensitive A mplifier |
| DAQ | D ata A cquisition |
| DARHT | D ual- A xis R adiographic H ydrodynamic T est |
| DOF-MS | D istance-of- F light M ass S pectrometry |
| DPR | D ouble P ulse R ejection |
| DTL | D rift T ube L INAC |
| FFT | F ast F ourier T ransform |
| FPGA | F ield P rogrammable G ate A rray |
| FRET | F luorescence R esonance E nergy T ransfer |
| FWHM | F ull W idth H alf M ax |
| HVPS | H igh V oltage P ower S upply |
| ICANS | I nternational C ollaboration of A dvanced N eutron S ources |
| LANSCÉ | L os A lamos N eutron S cience C enter |
| LENS | L ow E nergy N eutron S ource |
| MA | M ulti-strip A node |
| MCP | M icrochannel P late |
| MIEZE | M odulated I ntensity with Z ero E ffort |
| MIS | M oderator I maging S tation |
| MWPC | M ulti- W ire P roportional C ounter |
| NCNR | N IST C enter for N eutron R esearch |

| | |
|---------------|------------------------------------------------------|
| NIST | National Institute of Science and Technology |
| NSCL | National Superconducting Cyclotron Laboratory |
| PCB | Printed Circuit Board |
| PET | Positron Emission Tomography |
| PMT | Photomultiplier Tube |
| PPAC | Parallel Plate Avalanche Counter |
| PSI | Paul Scherrer Institut |
| PS-MCP | Position-Sensitive Microchannel Plate |
| QDC | Charge-to-Digital Converter |
| RA | Resistive Anode |
| RT | Risetime |
| RVS | Radiography Vacuum Station |
| S/N | Signal-to-Noise |
| SANS | Small Angle Neutron Scattering |
| SBD | Surface Barrier Detector |
| SiPM | Silicon Photomultiplier |
| SPM | Scanning Probe Microscopy |
| STM | Scanning Tunneling Microscopy |
| SW | Sense Wires |
| TCSPC | Time Correlated Single Photon Counting |
| TDC | Time-to-Digital Converter |
| TIRF | Total Internal Reflection |
| TOF | Time-of-Flight |
| TOF-MS | Time-of-Flight Mass Spectrometry |
| UCANS | Union of CANS facilities |

Chapter 1

Detection of photons, electrons, and ions by MCPs

1.1 Introduction to the induced signal approach

In this thesis a recently developed, novel approach [1] is explored in which the position of the incident particle is determined by sensing the electron cloud as it emanates from a MCP stack. The bipolar nature of the induced signals provides a unique signal to exploit. By coupling a sense wire plane to a delay line a position resolution of 466 μm FWHM was achieved in the first generation detector. While this first generation detector demonstrated that the concept behind the approach was valid, half-millimeter spatial resolution is not competitive with existing technology. The design, development, and optimization of a second generation detector that can achieve spatial resolutions to the level of 98 μm FWHM is explored. This second generation detector is competitive with other existing technologies.

Microchannel plates (MCPs) are routinely used in the detection of photons, electrons, and ions. Due to their high amplification and excellent timing characteristics they are particularly useful in the detection of a single photon, electron, or ion. In addition to sub-nanosecond time resolution, MCP detectors can also provide position resolution making them useful in many imaging applications. Imaging of photons, electrons, or ions plays a major role in many areas of chemistry, biology, and physics. As the detection of a single electron represents the ultimate in sensitivity, we utilize electrons to establish the position resolution of the induced signal approach. Improving the spatial and temporal resolution with which one detects the incident particle is thus of prime importance. Due to their high amplification and sub-nanosecond temporal resolution, MCPs are often used to detect single electrons or ions. When coupled to a photocathode or doped with CsI

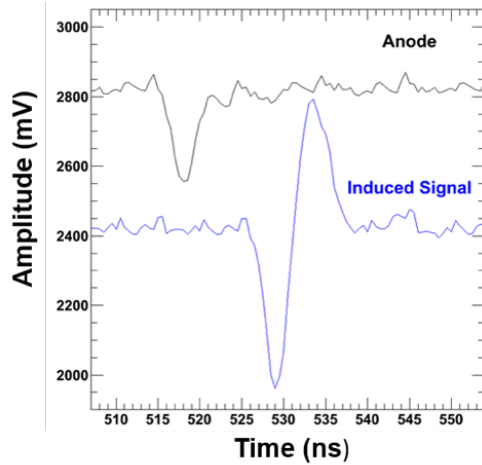


FIGURE 1.1: Trace of an induced signal on the sense wire plane along with an anode signal.

they can also be used to detect individual photons, and when doped with Gd or B they can be used to detect slow neutrons. To date only a few methods exist to provide position sensitivity to an MCP detector.

In the novel approach developed prior to this thesis, the electron cloud emanating from an MCP stack is sensed by a sense wire plane [1, 2]. A typical amplified (gain = 30), induced signal on the sense wire plane is presented in Fig. 1.1 along with the corresponding anode signal. As expected, the anode signal is a negative, unipolar pulse corresponding to the collection of the electron cloud. In contrast to the anode signal, the induced signal has an inherent bipolar nature. As the electron cloud approaches the sense wire plane a negative lobe is observed due to electrons in the wires being repelled by the charge cloud. When the electron cloud recedes from the sense wire plane, the electrons return to the wires, which results in a positive signal. The zero-crossing point corresponds to the time at which the centroid of the charge cloud passes by the sense wire plane. This intrinsic bipolar nature and symmetry of the induced signal could provide an inherent advantage over a unipolar signal. The design, construction, and performance of a second generation novel position-sensitive MCP is described. Simulations to understand the factors limiting the spatial resolution of the approach are investigated. This newly

developed sense wire detector is utilized in a neutron radiography measurement and the performance of the detector is presented.

1.2 Motivation for a MCP detector

Microchannel plate photomultiplier (MCP-PMT) detectors offer an excellent means of detecting scintillation light. These detectors have the characteristics of high gain, excellent timing resolution, a compact size, are largely insensitive to magnetic fields, provide sensitivity to a variety of different particles, and offer low power consumption. As a result, they offer advantages over traditional photomultiplier tubes and avalanche photodiodes. Providing position sensitivity in the earliest MCP-PMT detectors typically involved segmentation of the anode to provide a multi-anode device [3]. At present, designs of 2×2 , 4×4 , and 8×8 are available in a 2 in. \times 2 in. MCP-PMT [4]. With increasing granularity however, the electronic needs for readout of the detector grow dramatically. In addition, with an increased number of anodes the number of signals fed through the glass envelope of the MCP-PMT increases dramatically. As damage of even a single feedthrough will compromise the vacuum of the MCP-PMT, a large number of anodes becomes increasingly problematic. Moreover, the discrete nature of the segmentation can inherently limit the position resolution of the device even if analysis techniques such as charge centroiding are employed. This thesis seeks to describe the first step towards an MCP-PMT, which is to develop the position-sensitive MCP for the MCP-PMT. Integration of a photocathode and vacuum envelope will not be discussed.

Another technology used to sense scintillation light is a silicon photomultiplier, SiPM. This device consists of linked avalanche photodiodes and provides a gain of 10^6 , with a timing resolution of 100 ps in a compact form factor, and is largely insensitive to magnetic fields. Despite these characteristics which make them promising, at present

segmented devices have a limited granularity of approximately $3\text{ mm}\times 3\text{ mm}$ [5]. Moreover, they are also subject to optical cross-talk between adjacent elements [6]. Another disadvantage of the SiPM system is the need for cooling in order to achieve optimal performance due to a significant dark current background. Each $3\text{ mm}\times 3\text{ mm}$ element consists of approximately 5000 cells. Thus the area of each cell is approximately $1800\text{ }\mu\text{m}^2$. In comparison the pore of a recently available $5\text{ }\mu\text{m}$ pore MCP measures approximately $20\text{ }\mu\text{m}^2$ thus in principle allowing better spatial resolution. Moreover, the discrete nature of the SiPM cells means that tiling a large area with SiPM becomes extremely intensive in readout electronics.

1.3 Detection of photons, electrons, and ions by MCPs

A MCP can be used as a detector of electrons, ions, photons, or neutrons. For all incident particles, other than electrons, the incident particle is first converted into an electron either through the photoelectric effect or a nuclear reaction and the resulting electron is amplified. MCPs were originally developed for image intensification, and are still being used in night-vision goggles [7]. Their usage has expanded over the past three decades and several scientific disciplines presently employ MCPs. Table 1.1 depicts the wide range of energies of incident particles of that can be detected by a MCP along with the efficiency of detection. Table 1.1 lists 0.2-2 keV electrons as one of the highest detection efficiencies, hence it is particularly productive to focus on the detection of electrons. The detection of a single electron represents the ultimate in sensitivity. As a result, detection of a single electron with position sensitivity is the primary focus of the present research.

TABLE 1.1: Detection efficiencies of microchannel plates [8–10].

| Type of Radiation | Detection Efficiency (%) | |
|-----------------------------------------------------------------------|--------------------------|-------|
| Electrons | 0.2 - 2 keV | 50-85 |
| | 2 -50 keV | 10-60 |
| Positive ions (H ⁺ , He ⁺ , A ⁺) | 0.5 - 2 keV | 5-85 |
| | 2 - 50 keV | 60-85 |
| Thermal Neutrons | 50 - 200 keV | 4-60 |
| | 0 - 25 meV | 14-78 |
| uv Radiation | 300 - 1100 Å | 5-15 |
| | 1100 - 1500Å | 1-5 |
| Soft X-rays | 2 - 0.50 Å | 5-15 |
| Diagnostic X-rays | 0.12 - 0.20 Å | 1 |

1.4 The fundamental principles of image intensifiers, electron multipliers, and MCPs

To describe the operating principles of a MCP, it is important to first understand the technology leading up to their development; namely, image intensifiers and electron multipliers. Image intensifiers exploit the photoelectric effect by converting photons to electrons. In its simplest form, an image intensifier is two electrodes that are connected to an external power supply and placed under vacuum. An image is focused onto the photocathode, and each illuminated area generates electrons that go on to be accelerated by the electric field between the two electrodes. The electrons follow approximately straight flight paths and impinge upon the anode last, where the electrons are collected. The spatial resolution is well preserved when the photocathode and anode are close to one another. One can achieve amplification by increasing the bias, but one is limited to a certain max voltage when charge begins to arc through the evacuated gap. Without amplification, the image intensifier is limited with one incident photon yielding only one electron in the anode, so the electron gain is dependent on the intensity of light.

Electron multipliers, on the other hand, take advantage of metal electrodes called

dynodes that are progressively biased to higher potentials so as to direct the electron flight path. An electron impinging on a dynode liberates several low energy electrons in the material. These electrons are accelerated by the potential difference and when they strike the subsequent dynode they liberate more electrons. This process is repeated down the length of the electron multiplier. This successive multiplication at the dynodes leads to an exponential growth in electric charge at the output of the electron multiplier. The electron multiplier yields high gain but at the expense of spatial resolution. Due to the geometry of the dynodes, the electron flight path is not straight down the length of the electron multiplier. MCPs marry the high spatial resolution of the image intensifier with the high gain of electron multipliers. It was the development of the continuous-channel electron multiplier that allowed for the creation of MCPs, where the continuous-channel electron multiplier acts like an electron multiplier assembled of dynodes.

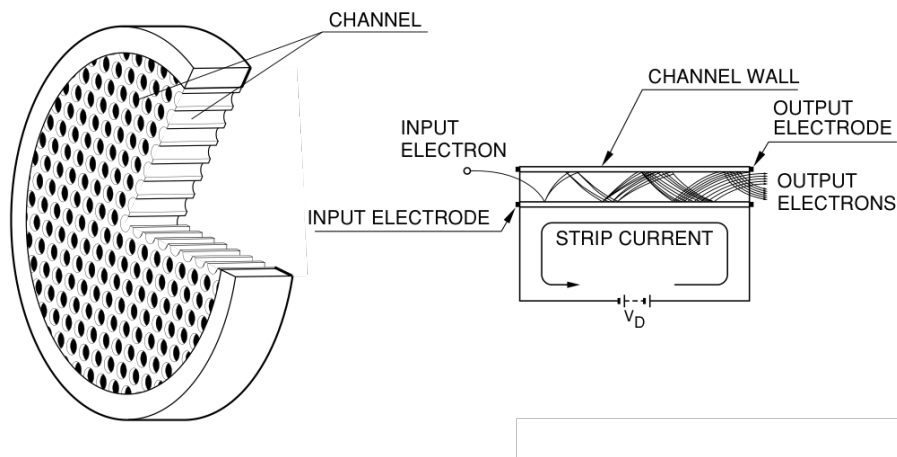


FIGURE 1.2: Cross-sectional view of MCP with operating principles shown in one channel [11].

Each MCP is composed of millions of miniature, continuous electron multipliers (typically 2-10 μm in diameter) that are oriented parallel to one another. A cross-sectional view of an MCP is presented in Fig. 1.2. Each channel surface is treated to act as a secondary electron emitter, so that each channel acts as an independent electron multiplier.

A differential voltage is applied to initialize electron amplification in each channel. Amplification begins when a particle with sufficient energy impinges on the channel surface. When the particle impacts the walls of the channels, it ejects two or more electrons, which are then accelerated and go on to eject more electrons. This process repeats itself several times down the length of the channel. A typical amplification of approximately 10^3 - 10^4 for each incident electron is achieved for one MCP. This secondary emission process is depicted in Fig. 1.2. Hence, the impinging particle results in a cascade effect, also known as an electron avalanche, at the output of the channel. The maximum gain of a single MCP is determined by space charge effects, which limit the amplification process.

To increase the gain beyond that of a single MCP, it is possible to stack multiple plates together. The total gain of electrons is then additionally determined by the orientation and number of MCPs in the system. Common arrangement of MCPs includes the Chevron stack consisting of two MCPs, and the Z-Stack consisting of three MCPs. The Chevron and Z-Stack arrangements refer to the orientation of the channels in one MCP as compared to another. The relative positioning of the MCP channels increases the overall electron gain, but reduces spatial resolution somewhat due to the dispersion of the electron cloud as it enters more channels. Spatial resolution is also hindered by the electrostatic repulsion between electrons upon departure from the rear of the MCPs. The overall gain of the MCP can be calculated by the expression below, where G is the gain factor that is determined from the secondary emissive characteristics of the channel material and l/d is the length to diameter ratio of the channel [12].

$$g = e^{G(\frac{l}{d})} \tag{1.1}$$

Leaded glass is typically used for the channel because of its desirable gain factor. Table 1.2 lists the composition of the leaded glass material. This material is chosen for its

desirable secondary emission qualities as well as its semi-conductor nature, which allows for the replenishment of charge, from an external power supply, following an electron avalanche event. A drawback to glass is its hydrophilicity, which can cause channels to bow and break at atmospheric pressure. Consequently, MCPs are stored under vacuum to extend their lifetime. Over the input and output surfaces of the MCP Inconel, Ni-Cr, or Cr is deposited onto the surface to form electrodes. The penetration depth of this pore end spoiling is typically the pore diameter multiplied by a factor between 0.5 and 2 [12]. Some applications use an even deeper pore end spoiling depth so as to collimate the output electrons.

TABLE 1.2: Elemental composition of Corning 8161 glass that is used to fabricate MCPs [13].

| Z | Element | Weight Percent |
|----|---------|----------------|
| 82 | Pb | 47.8 |
| 8 | O | 25.8 |
| 14 | Si | 18.2 |
| 19 | K | 4.2 |
| 37 | Rb | 1.8 |
| 56 | Ba | 1.3 |
| 33 | As | 0.4 |
| 55 | Cs | 0.2 |
| 11 | Na | 0.1 |

*Density = 4.0 g/cm³

The channels of an MCP are tilted such that the incident particle is likely to bombard the inner wall of the channel surface, as opposed to traveling straight through the channel. Typically the optimal channel bias angle ranges from 5° and 15° [12]. Straight channel multipliers typically operate at gains of 10³ to 10⁵ [7]. However, straight channel multipliers have an upper limit set by the onset of ion feedback. As the gain increases, so does the likelihood that positive ions will be generated at the high-density charge region at the output of the MCP. These ions are produced from a collision between a residual gas molecule in the channel (or chamber) and an electron. Such positively charged ions

can drift up the channels of the MCP. Operating MCPs at a pressure below 5×10^{-6} torr minimizes ion feedback. Stacked MCPs are oriented so that the bias angles provide a sufficiently large directional change so as to reduce the likelihood that positive ions produced at the back surface will reach the front surface of the MCP. The pulse height distribution of a single MCP, with a single electron incident on the front of the MCP, is an exponential function [12]. However, when using stacked MCPs the gain becomes saturated due to the space charge effect. The result of the space charge effect on the pulse height distribution is a peak that forms in the distribution.

The formation and transit time of the electron avalanche is on the order of 100 ps [12]. The MCP signal is thus inherently fast in nature with a small associated jitter, and can be as fast as a nanosecond [14]. One limitation of this type of detector is saturation following an event in a channel. After generation of a pulse, the recovery time of a channel can take up to milliseconds. Nonetheless, due to the large number of channels (typically several million) present in an MCP, the detector can sustain a high rate of 10^6 Hertz [12].

Conventional MCP fabrication begins with a glass tube with a solid, acid-etchable core. The glass is heated in a zone furnace and drawn using fiberoptic techniques. Individual fibers are then stacked together in a hexagonal array, heated, and drawn again. These multi-fibrous capillaries are stacked and then fused together into a boule. The fused rod is sliced into thin wafers about a millimeter thick and then the surface of each wafer is polished. The solid core of the wafer is dissolved in hot acid, and the plate is heated in hydrogen gas so as to reduce the lead oxide and give the glass surface the required electrical conductivity. A metal film is evaporated on both the front and back surfaces of the wafer so that an electrical connection can be made to all of the pores. The fabrication process is illustrated in Fig. 1.3.

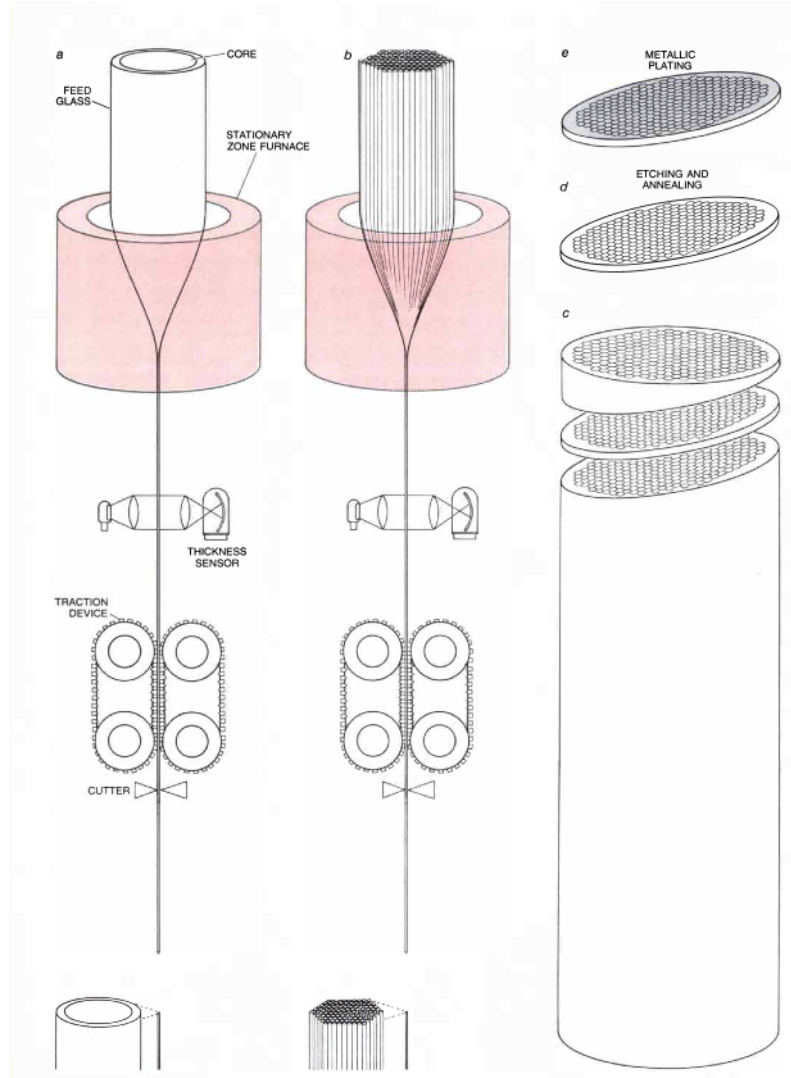


FIGURE 1.3: Illustration of the conventional two-draw process, which is used to fabricate MCPs [15].

1.5 Motivation for a PS-MCP

Measurement techniques involving improved radiation and particle detection methods in terms of temporal and spatial resolution could be developed through the development of this position-sensitive MCP (PS-MCP) detector. This development could impact advanced diagnostic techniques relevant to proton, X-ray, and other radiographic techniques. For example, to non-destructively assess an unknown material, both photons

(X-rays) and neutrons are often used. These two probes are complementary with X-rays offering sensitivity to high Z , structured materials and neutrons more sensitive to low Z , disordered materials. Measurement of the scattered particle whether photon or neutron involves its detection in space and time, hence both spatial and temporal resolution are important characteristics of any detection system. MCPs are unique in that they are sensitive to a variety of particles including X-Rays and thermal neutrons (with B or Gd dopants), and thus development of a PS-MCP detector could impact both of these complementary radiographies.

One of the most advanced imaging endeavors is the Dual-Axis Radiographic Hydrodynamic Test facility (DARHT) in which an imploding mock-pit is imaged during detonation. X-rays are converted to visible light by fast scintillators of lutetium orthosilicate (LSO) arranged in a mosaic of 1 mm diameter crystals [16]. Imaging the visible light is achieved by high quality CCD cameras. Another venue for imaging in stewardship science is in the interdiction of sensitive nuclear materials at border crossings. However deployment of advanced spectroscopic portals for primary inspection at points of entry was not supported based on their performance [17]. Improving effectiveness while reducing cost is a key issue. The PS-MCP presented has the advantages of being a low cost alternative with the potential to scale large areas. Furthermore, it is based on one of the fastest timing detectors available, the MCP, and therefore could achieve the required throughput of inspection at points of entry.

Other techniques that could benefit from an improved PS-MCP (position-sensitive MCP) detector includes but is not limited to: slow neutron radiography [18], fast neutron radiography [19], beam imaging at radioactive beam facilities [20, 21], Cherenkov ring imaging [22], time-of-flight positron emission tomography (PET) [23], time correlated single photon counting (TCSPC) [24], three dimensional atom probe techniques

[25], phase imaging ion cyclotron resonance [26], time-of-flight applications in mass spectrometry [27], and time-resolved fluorescence lifetime imaging microscopy [28]. Position and temporal sensitivity is clearly important in a wide array of analytical applications, thus the development of a novel type of PS-MCP detector with unique characteristics could have a broad impact.

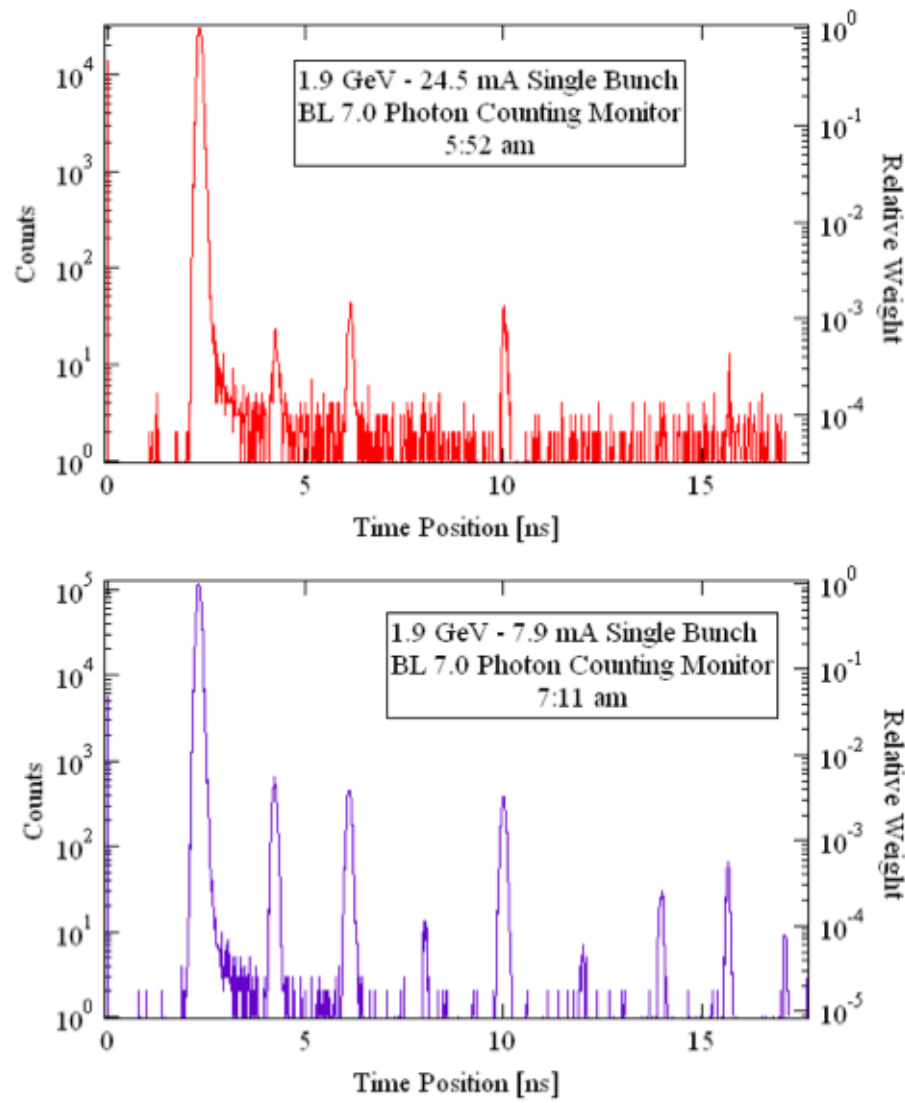


FIGURE 1.4: ALS bunch population measurements using a PS-MCP detector. Top panel) situation right after injection, bottom panel) situation after 76 min.[29].

One application that required an MCP based imaging detector was performed at the Advanced Light Source (ALS) of the Lawrence Berkeley National Laboratory [29]. An PS-MCP was necessary due to the inherently fast timing characteristics of the MCP. In their experimental setup, a sample of was bombarded with a pulsed monochromatic beam of X-Rays, and the scattered photons were measured using a PS-MCP detector. The beam consisted of 18 ps (RMS) photon bunches spaced by 2 ns. The goal was to optimize the bunch population by mitigating the diffusion of electrons between bunches with injection of a single burst of photons. The ALS bunch population is presented in Fig. 1.4. The top panel shows the bunch population right after 25 mA electrons are injected into a single bunch, and corresponds to the highest peak. Other peaks, termed “parasite” bunches, have a relative amplitude of $\sim 0.1\%$ with respect to the main peak. These parasite bunches and are due to the imperfect operation of the injector. The bottom panel shows the population for the same RF buckets after 79 min. The total current dropped from 24.5 mA to 7.9 mA, while the relative population in the parasites is increased and their relative amplitude is now $\sim 1\%$ of the main peak. This information was used to measure the diffusion coefficient and lead to a bunch cleaning procedure that needs to be performed every ~ 30 s. The new bunch cleaning procedure is currently being utilized at ALS. From this example, one can see how vital a role PS-MCP detectors can play in the development of beam facilities.

Many applications rely on the simultaneous measurement of both position and time of a particle (electron, photon, or ion). Many imaging applications demand such a simultaneous measurement. For example, PET relies on position information to verify that the gamma rays detected were annihilation gamma rays (determined by the characteristic 180° difference in angle) and temporal information to verify that the gamma rays originated from the same event. We have opted to investigate the development of this detector with low-intensity fluxes. If one can achieve reasonable spatial resolution with

a low flux of particles over a short exposure time then this can translate to lower dosing requirements for methods like PET. A lower dose mitigates unwanted side effects for patients.

There are many cutting edge types of research for single molecule fluorescence. The applications range from single molecule tracking in live cells using total internal reflection (TIRF) microscopy to studies of macromolecule conformation or enzyme activity using single-molecule fluorescence resonance energy transfer (FRET). Performance optimization of these measurements is achieved through detector and fluorescent probe development. When using quantum dots, a bright and stable fluorescent probe, in the the imaging of live cells the EMCCD camera is typically employed [30]. One limitation of EMCCD cameras is the readout rate. Each pixel is readout sequentially, which is the inherent bottleneck of the approach. For a 512×512 pixel detector, it takes 26.2 ms to digitize a frame (assuming ~ 100 ns/pixel) [30]. The frame rate is limited to 30 fps when the time of the computer is taken into account. These detectors lack the capability of detecting the evolution of the fluorescence lifetime of a single particle along its trajectory. However, a detector with improved time resolution could track this time evolution. A PS-MCP has already been demonstrated for this application and is noted for its ability to detect, localize, and time-tag every photon individually [30].

The only significant difference between our experimental setup and that of a MCP-PMT is the absence of photocathode in our setup. Thus, a PS-MCP with enhanced capabilities could provide the means to further the development of improved MCP-PMTs. Furthermore, the innovative ideas could also be employed to further the area of TCSPC. A common problem faced in photon counting is if you have too many photons incident on the detector in close temporal proximity, then the signal peaks will overlap and counting error arises. Improved temporal resolution would help to minimize counting error and

perhaps improve the detection limits of TCSPC. A specific example that utilized PS-MCPs was in the incorporation of the MCP into a phototube where it was coupled to an X-Ray scintillator to form a photon counting X-Ray detector [31]. This approach has found a niche in the field of protein crystallography. Some other applications include short-wavelength astrophysical observations such as observation of O^+ and He^+ emission from the upper atmosphere [32].

Another analytical technique where a position-sensitive MCP can be utilized is in time-of-flight mass spectrometry (TOF-MS). It is simultaneous measurement of position and time of a particle that gives rise as another means of determining a particles velocity vector. A common challenge faced in TOF-MS occurs when two or more molecules arrive simultaneously on a detector. Certain PS-MCP detectors not only allow you to distinguish such events but allow the two particles to be resolved. For example, one group incorporated a multi-anode (quadrant division) detector in an electrospray ionization-TOF instrument to reduce the dead time of their time-to-digital converter (TDC) [33]. This lead to a ~ 2.5 times increase in counting efficiency of their TDC based data acquisition system without compromising mass resolution. This multi-anode was also utilized as a diagnostic tool for the optimization of ion transmission. A more complex multi-anode system incorporated for mass spectrometry was developed for matrix assisted laser desorption ionization TOF [34]. This system incorporated 100 anodes and a TDC based data acquisition system to measure the spatial distribution of peptides.

Perhaps a more appropriate technique in mass spectrometry is one that requires measurement of the spatial distribution of ions. Such a technique is distance-of-flight mass spectrometry (DOF-MS) [35]. In this technique, ions exit the source with m/z -dependent velocities. At a given time, their mass-dependent locations are measured. A position-sensitive element is required in DOF-MS, and the MCP-SW detector described in this work could be utilized for this purpose.

1.6 Existing approaches to position sensitivity to MCP detectors

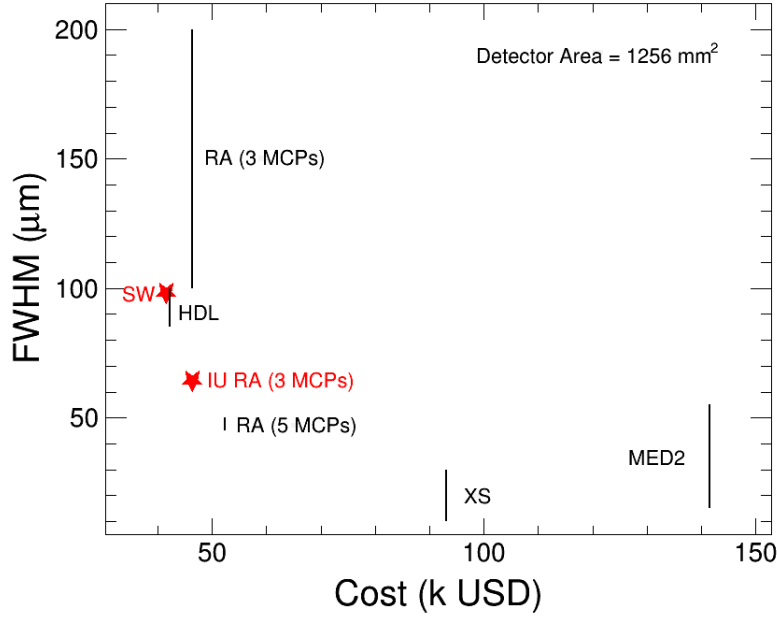


FIGURE 1.5: Resolution vs cost for various PS-MCPs. Prices based from commercial detectors from Quantar [36], RoentDek [37], Sensor Sciences [38], and X-Spectrum [39] on July 31, 2017.

A few methods already exist to provide position sensitivity to a MCP. In contrast to existing technology where the electron cloud is collected, the electron cloud induces a signal on the wire harp as it emanates from the MCP stack. The goal of the project is to understand the factors governing the spatial resolution attainable and to fabricate a detector that provides single electron detection with sub-millimeter spatial resolution.

The major approaches to make a MCP position sensitive are partitioned into the following classes: the multi-anode [40], the cross-strip anode [41], resistive anode [42–44], the Timepix2/Medipix CMOS detector [18, 45], and helical wire delay line [31, 46]. The dependence of resolution as a function of cost is presented for each category of PS-MCP for an active area of 1256 mm² in Fig. 1.5. The expected anti-correlation between spatial resolution achieved and the cost of the unit is observed. The Timepix2/Medipix has

TABLE 1.3: Summary of the advantages and disadvantages of various PS-MCP detectors.

| PS-MCP Detector | Advantages | Disadvantages |
|--------------------|-----------------------------------------------------------------------------------------------------------------------|--------------------------------------------------------------------|
| Multi-Anode | Fast signal Multi-hits Resolution 25-50 μm | Cost of readout electronics Cross-talk between anodes |
| Resistive Anode | Resolution 50–100 μm Simplicity of readout Low power | Relatively slow signal Multi-hits Rate limited <100kHz |
| Cross-Strip Anode | Fast signal Resolution 10–20 μm Uses chevron MCP Multi-hits | Cost of readout electronics High power |
| Helical Delay Line | Fast signal Resolution 85–100 μm Can tile large areas Simplicity of readout | Fragility of single wound wire Atten./dispers. in delay |
| Medipix2/Timepix | Resolution 15–55 μm Uniform spatial response Low power (1 W/chip) | High cost Small active area Cost prohibits tiling large area |
| Induced Signal | Fast signal Resolution 98 μm Simplicity of readout Multi-hits Can tile large areas Low cost | Atten./dispers. in delay |

the best resolution for the highest cost, while the induced signal approach has the worst resolution but the lowest cost. Pricing is based off commercial technologies in every case but the induced signal approach, which is still in the prototype phase. Furthermore, the majority of the price of the induced signal approach is in the DAQ. We are presently using state-of-the-art high speed digitizers, which results in the price of the DAQ being \sim \$29k. Furthermore, every year the price of high speed digitizers decreases, which favors the affordability of this approach. The cost of the induced signal approach could be mitigated by replacing the high speed digitizers with a mix of analog and digital electronics. Such an approach could reduce the cost significantly although the position resolution may suffer somewhat. Moreover, the induced signal approach is particularly well suited to tiling a

large area. Most of the cost of the approach is in the DAQ currently, which digitizes the entire waveforms. It is even possible to reduce this price with use of a CFD and TDC readout scheme. Since the price is mostly in the DAQ, using a larger MCP format is particularly appealing because the majority of the price increase would be in the MCP itself. Furthermore, there would be a small increase in price if more delay boards are needed per dimension to accommodate the larger area. There are commercially available 75 mm MCPs for \sim \\$11k, and custom orders can be accommodated for 100 mm MCPs for \sim \\$27k [4]. The approach and results described in this thesis can provide sub-100 μ m resolution for a 100 mm \times 100 mm with the only increased cost coming from the MCP itself. Researchers at Argonne National Laboratory and University of California at Berkeley are presently working on developing larger format MCPs as large as 20 cm, which this approach would largely benefit from [47]. The same scalability argument cannot be applied to the Medipix2 detector. Moreover, unlike the Medipix2 detector, scaling the sense wire approach has the added benefit of no dead area between elements.

As there is no ideal detector suitable for every application, one must consider the relative advantages and disadvantages of each approach. For example, a resistive anode would not be suitable in an application where the particle flux exceeds 100 kHz and the Timepix2/Medipix detector would not be suitable for tiling a large area. In the remainder of this section, these different approaches are briefly described so that the present induced signal approach can be distinguished from them. A generalized table summarizing the relative merits and drawbacks of each approach is presented in Table 1.3.

1.6.1 Multi-anode detector

The multi-anode approach simply replaces a single anode with multiple anodes, which are independently readout. Consequently, spatial resolution is determined by the number and geometry of anodes [48]. In addition to this fundamental limitation, a further

drawback of the multi-anode approach is the cross-talk that arises between adjacent anodes. Simply put, cross-talk represents the signal produced on an anode due to the presence of a signal on a neighboring anode. Cross-talk has been well characterized in multi-anode designs. As cross-talk increases with increasing segmentation, it represents a fundamental limitation of this approach. One of the simplest examples of the multi-anode approach is the Four-Quadrant Anode, as shown in Fig. 1.6. The multi-anode approach has inherently fast charge collection speeds and high resolution on the order of 10–25 μm have been achieved [40, 49]. However, the image distortion in these detectors has been described as severe [40]. Also, it can be expensive to have readout electronics for each anode as the segmentation increases. Designs of 64 independent anodes (8×8) are considered state-of-the-art. We have mitigated the dense electronics of multi-anode systems by coupling a multi-anode to a delay line readout. We did this to construct a beam imaging detector, and more detail about this detector can be found in Section 3.2.

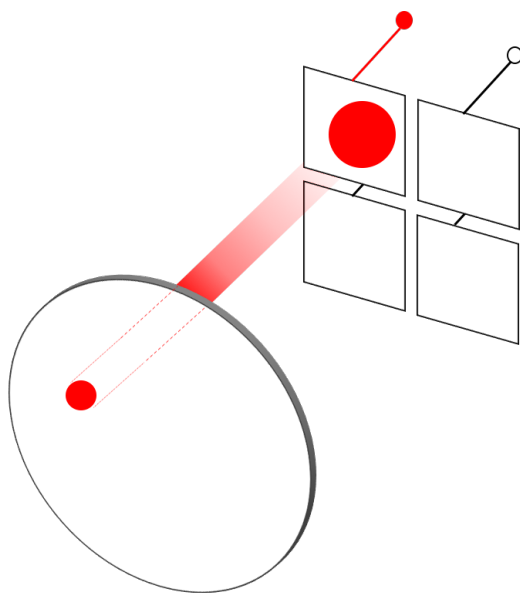


FIGURE 1.6: Schematic drawing of an electron cloud impinging upon a four-quadrant anode.

1.6.2 Cross-strip anode detector

The cross strip anode is composed of a plane of parallel strips, which is overlaid orthogonal to an identical strip plane; as shown in Fig. 1.7. The two planes are electrically isolated from each other by a ceramic, insulation layer. This layer which provides isolation still allows electrons to reach the lower strips. The resulting grid collects the impinging electron cloud from the MCP on its surface. The charge is readout on the wire strips (usually 5 strips) by coupling the strips to an amplifier and analog-to-digital converter (ADC). When employing the cross strip anode method, high accuracy precision events with low MCP gain are common [41]. This position accuracy is the result of the capacitance load being much lower on the strip channels as compared to the high capacitance load on delay lines; where the delay line load arises from the noise on the high-speed amplifier [41]. Consequently, the cross strip only requires two stacked MCPs as compared to other techniques where a higher gain is needed. The use of fewer plates reduces wear on the detector since a lower gain pulse is propagating through the MCP channels. Also, the spatial resolution is slightly improved because the electron pulse is less distributed in the channels in the Chevron stack as compared to the Z-Stack. The best resolution reported is 10 μm FWHM [41], but is a fairly expensive approach relative to other technologies (see Fig. 1.5). While silicon processing technology enables the fabrication of the strips, it is one of the major reasons why the cost of detector fabrication is so high. Moreover, use of silicon processing leads to an inflexibility of changing design features. For example, change of a strip pitch requires a new design with the cross-strip anode, whereas changing wire pitch in the induced signal method is simple. Another disadvantage of this approach is the complexity of the electronics seem ASICs have to be employed for the readout of each strip.

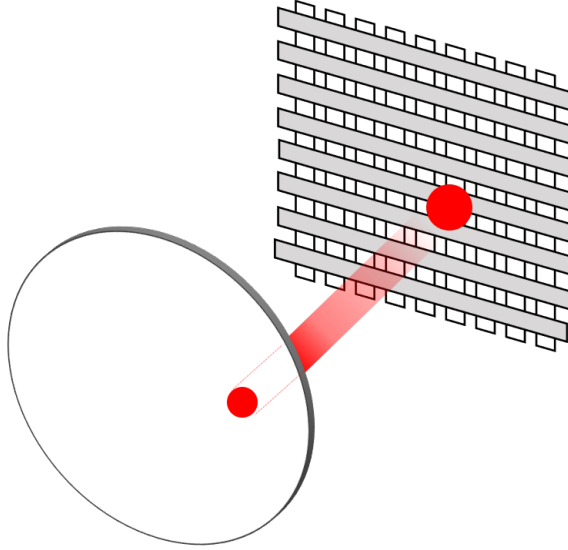


FIGURE 1.7: Schematic drawing of cross strip (XS) readout detector.

1.6.3 Resistive anode detector

The principal advantage of the resistive anode approach is the simplicity within the anode itself and the associated electronics. In this approach, the anode collects the electron cloud at the four corner electrodes. A schematic drawing of the resistive anode is shown in Fig. 1.8. In this approach, the position of the centroid of the charge cloud can be determined by recording either the relative time or relative charge at the four collection electrodes. The position can be determined by using the following formulas [42]:

$$X = \frac{Q_1 + Q_4}{Q_1 + Q_2 + Q_3 + Q_4} \quad (1.2)$$

$$Y = \frac{Q_1 + Q_2}{Q_1 + Q_2 + Q_3 + Q_4} \quad (1.3)$$

where Q_i is the charge detected at the i^{th} corner of the sheet.

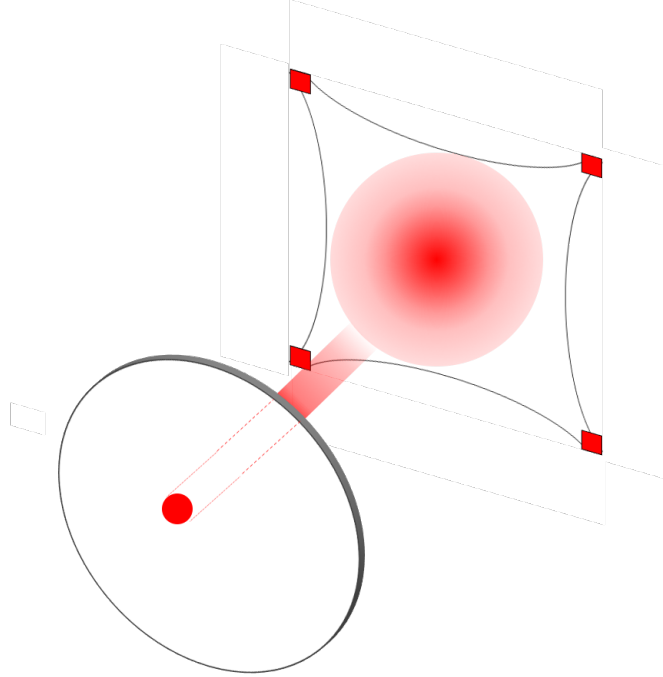


FIGURE 1.8: Schematic drawing of an electron cloud from an MCP impinging upon a resistive anode. Charge (Q1, Q2, Q3, and Q4) is collected at the four-collection electrodes, which are located at the corners. The resistive anode has a reverse pincushion design to help facilitate proper charge propagation and collection at the corners.

The RC characteristics of the anode, which is largely due to the high resistance of the sheet, typically $0.5 \text{ M}\Omega$, limits the maximum rate the detector is capable of [48]. Even if one is using the charge division approach, there is a significant time jitter at each of the four resistive anode signals [48]. This timing slew is inherent to charge propagation systems, where there is a transmission delay across the anode. The timing jitter affects the sampling of the peak amplitude of the resistive anode signals, and consequently affects the spatial resolution [48]. Quantar Technology quotes a spatial resolution of $100 - 200 \mu\text{m}$ FWHM [50]. However, to achieve $50 \mu\text{m}$ FWHM spatial resolution with a resistive anode requires the use of complex MCP arrangements and retarding potentials [51–53]. Thus, one could get decent spatial resolution in this technique, and realize a larger sensor at lower cost than say the Medipix2/Timepix detector. But this approach is limited to

count rates lower than 100 kHz due to the large resistance of the anode and suffers from non-negligible image distortions at the edges.

1.6.4 Medipix2/Timepix CMOS detector

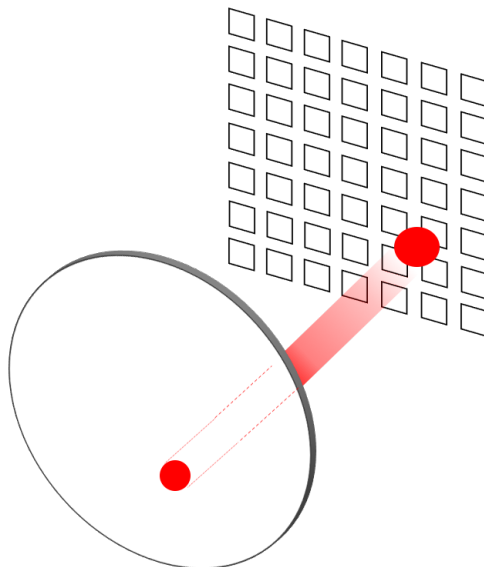


FIGURE 1.9: Schematic drawing of Medipix2/Timepix detector.

The Medipix2/Timepix is a CMOS pixel detector consisting of 256×256 individual elements that can each work in single photon counting mode. A schematic drawing of the Medipix2/Timepix CMOS detector is shown in Fig. 1.9. These pixels are based on $0.25 \mu\text{m}$ CMOS technology and measure $55 \mu\text{m} \times 55 \mu\text{m}$. Each pixel is connected to a charge preamplifier before the signal is split and discriminated by two separate discriminators. Use of both discriminators provides a low and high energy threshold. When the Medipix2/Timepix CMOS readout is coupled to an MCP, the approach can achieve an impressive 15 to $55 \mu\text{m}$ FWHM spatial resolution. The detector itself can operate at high counting rates exceeding 100 MHz/cm^2 and achieve a spatial resolution of $55 \mu\text{m}$ [47]. When coupled to an MCP, the maximum count rate is dictated by the MCP, where rates of $\sim 2\text{-}3 \text{ MHz}$ with resolution of $\sim 15 \mu\text{m}$ have been demonstrated [18].

Simultaneous events can be detected with this approach up to $\sim 25\text{k}$ cps. This detector can operate at low gains (10^4 - 10^5), which will lead to an extended lifetime of the MCP. Low noise characteristics of < 100 electrons RMS are associated with this readout [54]. There is also low power consumption associated with this device of ~ 1 W/chip, which makes this detector viable for astrophysical observations. There is a very uniform readout, which leads to very little image distortions even at the edges. However, these advantages come at a high cost (see Fig. 1.5) for detection over only a small area ($14 \times 14 \text{ mm}^2$ per chip) [18, 45]. This high cost for a detector precludes tiling a large area with multiple detectors although a small system of 4 chips ($28 \text{ mm} \times 28 \text{ mm}$) has been implemented.

1.6.5 Helical delay-line detector

In the helical delay line anode method, a helical delay line acts as the anode providing a measure of the position in one-dimension. The operating principle behind the helical delay line strategy is shown in Fig. 1.10. In this approach, an electron cloud output from an MCP stack is collected on a coiled wire that also serves as a delay line. The signal transverses along the transmission line, splits at the junction (Kirchhoff's Law), and is measured for each end of the delay line. Due to the fact that the signal traverses a different distance to reach the two ends of the delay line, the signal arrives at the two ends of the delay line at different times. It is the timing difference ($t_1 - t_2$) between both ends of the delay line, which is used to find the incident position of the electron cloud. This timing difference is taken with respect to back of the MCP signal as time = 0. The total time ($t_1 + t_2$) is also used as a check for valid signals, because the delay line is a constant distance, therefore propagation time. By placing two independent helical delay lines in an orthogonal orientation, one can determine the position of the charge cloud in two dimensions. There is also a second helical wire wound adjacent to the signal wire.

This secondary wire acts as a reference wire and it used to reject noise common to both the signal wire and reference wire.

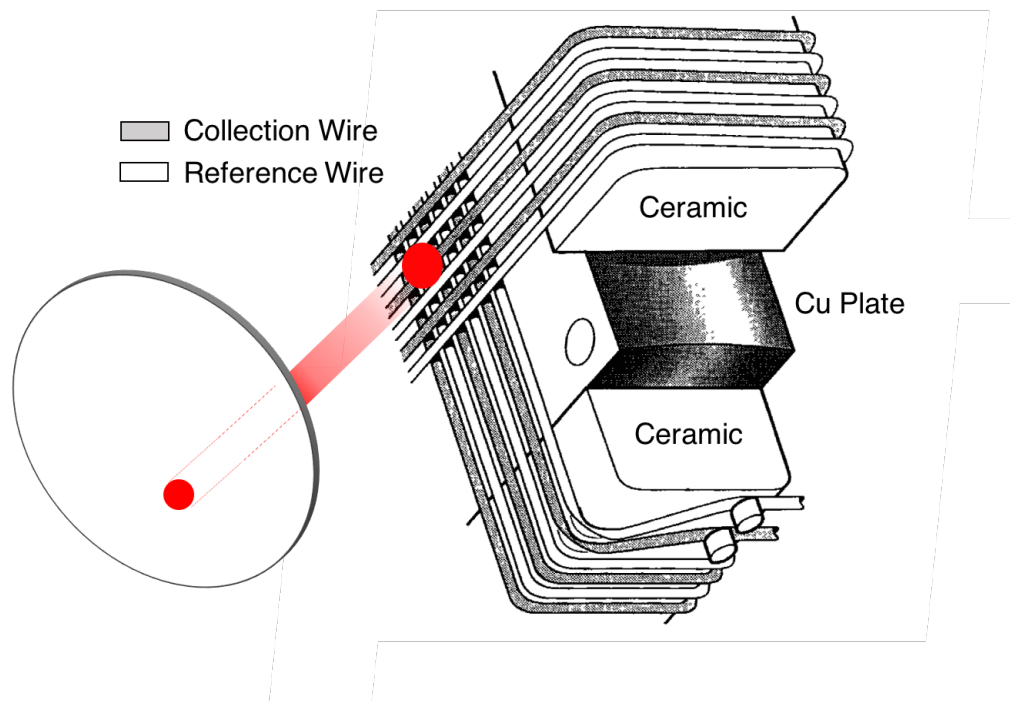


FIGURE 1.10: Schematic drawing of the helical-wire delay-line readout [31]. The charge cloud from the MCP is incident on the meander-shaped transmission line, and the signals at each end of the delay line are readout.

One advantage of this approach is that it does not depend on uniform gain across the MCP surface, as long as the signal-to-noise ratio is sufficient [55]. The approach is also not very sensitive to the quality of the MCPs, for the electron cloud can spread more and the centroid determination will be unaffected [55]. The position resolution is determined by the channel-to-channel spacing in the MCP and the best spatial resolution reported is $85 \mu\text{m}$ and the time resolution is below 1 ns [46, 55]. The helical delay line method requires relatively low readout electronics as compared to multi-anode anode approach, where one needs readout electronics for each anode; thus, the helical delay-line approach is favorable for tiling large active areas because it is less expensive to do so. Also, the helical delay-line approach has been applied to analyze position and timing information

for particles at the 1 MHz rate and multi-hit events can be collected and analyzed at the 20 kHz rate [55].

The inherent difficulty is that the helical wire anode is rather fragile and sensitive to tension changes during the baking process. The helical delay line has an anode that is created from a single wire winding, while the sense wire plane (in the induced signal approach) consists of individual sense wires. These sense wires do not consist of a single winding and thus constitute a less fragile mechanical structure.

1.6.6 Conclusions

In this chapter, the main approaches used to make an MCP position-sensitive have been presented. Now that the existing technologies have been briefly discussed, similarities and differences between the existing approaches and the induced signal approach can be discussed. The induced signal approach is inherently different from other technologies, as the electron cloud emanating from an MCP is sensed rather than collected. This inherent difference means that the signal amplitude is ~ 10 times smaller than in the direct collection of the electrons. Nonetheless, the unique induced signal shape compensates for this reduced signal amplitude. While both the Medipix2/Timepix and resistive anode rely on charge integration to measure the position of the incident particle, some of the most exciting advances in electronics are being made in the domain of high speed sampling and processing of signals. We therefore opted to investigate the limit of spatial resolution that could be achieved with high speed digital sampling of the induced signals. In the present work, we demonstrate that the induced signal approach provides a low cost alternative with competitive spatial resolution as compared to existing technologies. The low cost of this induced signal approach makes the coverage of large areas feasible by using multiple detectors each capable of sustaining a high rate.

All the approaches have a common aspect. They rely on charge centroiding to achieve the optimal resolution. For example, in the helical delay line approach the charge cloud from the MCP incident on the delay line was as large as 1.5 cm [31]. This limits the ability of the detector to measure the particles at small relative distance. This fundamental limitation is a defining characteristic we propose to overcome with the new design. In this work, we seek to develop a detector with single-electron sensitivity, sub-millimeter position resolution, sub-nanosecond time resolution, and the capability of resolving two spatially separated, simultaneous electron events.

Chapter 2

Exploring the Spatial Resolution of PS-MCP Detectors

2.1 The induced signal approach

In this chapter the design, development, and performance of a PS-MCP using the induced signal approach is described. The initial concept of the induced signal method is presented along with details of the first generation detector. Tools necessary to understanding this project are detailed. In addition to the induced signal detector, the implementation of pulse shape analyses in a resistive anode and a multistrip/delay line anode detector are also discussed.

2.1.1 Sensing an electron avalanche in a gas detector

The idea for the novel PS-MCP detector evolved from work done with parallel plate avalanche counters (PPAC) and multi-wire proportional counters (MWPC) in the 1990's by the Indiana University Nuclear Chemistry Group. Gaseous detectors have a long and fruitful history in high energy and nuclear physics experiments. The MWPC was first introduced in 1968 by G. Charpak and co-workers [56], while the PPAC was introduced by G. Charpak and F. Sauli 1978 [57]. In 1992, Charpak was awarded Nobel Prize in physics “for his invention and development of particle detectors, in particular the multiwire proportional chamber” [58]. A schematic drawing of the hybrid gas detector developed at Indiana University is shown in Fig. 2.1. The detector is partitioned into two distinct regions, where one region operates as a multi-wire proportional counter while the other region operates as a parallel-plate avalanche counter. During normal operation, the detector is placed within a common volume of gas. The main components of the detector

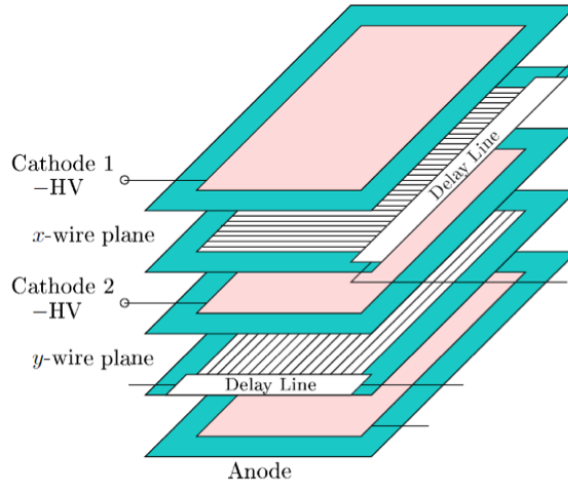


FIGURE 2.1: Schematic diagram of the hybrid gas detector PPAC/MWPC (Parallel Plate Avalanche Counter / Multi-Wire Proportional Counter). The delay-line signals are shown above (namely x_L , x_R , y_U , and y_D) and are used to determine position [59].

include: one anode, two cathodes, and two wire planes. The MWPC region consists of two aluminized mylar foils (cathode 1 and 2) with a wire harp in between (x-wire plane); while, the PPAC region consists of one aluminized mylar foil (cathode 2) and anode with a wire harp in between (y-wire plane). Each wire harp is made out of $50 \mu\text{m}$ copper beryllium wires with a pitch of 2.54 mm [59]. Each wire is connected at one end to a tap of a delay line (passive LC delay chips– Rhombus Industries model TZB12-5). The PPAC region has wires stretched in the orthogonal direction (y-wire plane) with respect to the MWPC region, such that the combination of the position information in both regions provides two-dimensional position information. It was development of the PPAC that spurred the novel PS-MCP detector idea.

Under normal operating conditions in gas chambers, molecules are ionized and the ions and electrons produced are accelerated through the gas by use of an applied electric field. For sufficiently high electric fields, the kinetic energy acquired by the electrons is above the ionization energy of the gas. As the electrons move toward the anode, they collide with additional gas molecules, thus resulting in secondary ionization. In an

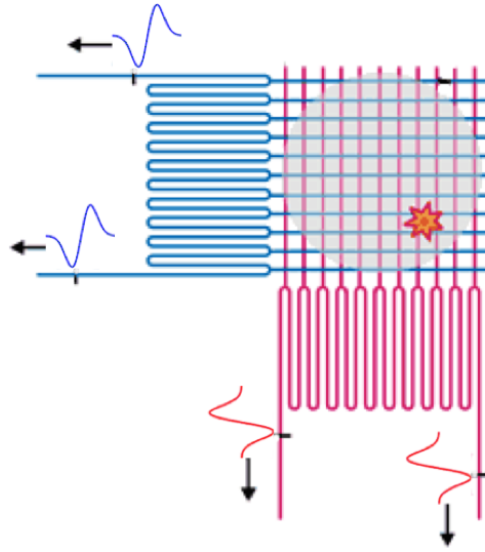


FIGURE 2.2: Delay line concept, which is used to obtain position information wire planes [60].

avalanche counter, the secondary electrons are accelerated, collide, and produce tertiary electrons. This amplification process is described by the Townsend Avalanche. As the avalanche passes by the wire plane it induces a current on the wires. This current pulse flows from the delay line connected to the wire plane. It is the tapping of the induced signal to a delay line, which allows for the encoding of the position of the electron cloud.

In Fig. 2.2 the concept of the delay line approach is indicated. The cartoon explosion is the point of incidence of the electron cloud on the sense wires. One can see how each wire harp is tapped into a serpentine delay line. The two colors in Fig. 2.2 represent the two independent wire planes, which together form a two-dimensional grid. The charged pulse, incident on the wire harps, propagates through the wires until the pulse arrives at the delay line. When the pulse reaches the delay line, the signal splits because here the current can flow in two directions. In other words the current has reached a junction and abides by Kirchhoff's Junction Law. Thus, the signal has split at this junction and there is a simultaneous propagation to the two terminations of the delay line. It is the time difference between the arrivals of signal to each of the ends of the delay line that can be

utilized to find the initial position of the electron pulse. In the delay line method, all wires are connected in tandem, which in turn leads to the decrease in number of channels needed to gain position information from the system.

2.1.2 The MCP-SW detector v1.0

It was proposed that the same approach used in the sense wire plane of the PPAC detector could be utilized to develop a PS-MCP. The aim is to provide detection of a single electron, which when amplified by an MCP stack induces a signal on a sense wire plane and allows for collection of an electron cloud on the anode.

The test setup is housed in a vacuum chamber, with a typical pressure 1×10^{-7} torr, in order to operate the MCPs. The MCP Z-Stack, purchased from Photonis (APD 3 40/12/10/12 D 60:1), has an active area of 40 mm, $12 \mu\text{m}$ center-to-center pore spacing, $10 \mu\text{m}$ pore diameter, $12^\circ \pm 1^\circ$ bias angle, and 60:1 length to diameter ratio. The sense wire plane is a printed circuit board (PCB) with an outer dimension of 14 cm x 14 cm. Au-W wires, $25 \mu\text{m}$ in diameter, are strung across a 50 mm x 50 mm hole in the PCB. The wires have a pitch of 1 mm. To wind the wires we utilized a large $\sim 1.5 \text{ m} \times 1.5 \text{ m}$ wire winder at Indiana University Cyclotron Facility. Its operation required supervision by a technician. In the test setup, a photon or single electron impinges upon an MCP where it is amplified to an electron cloud, the electron cloud is accelerated past the sense wire plane, and then the electron cloud is collected on the anode. This concept is illustrated in Fig. 2.3. The spacing between the back surface of MCP stack and the front sense wire plane is 12.7 mm, and the spacing between the back of the sense wire plane and the anode is 10.9 mm.

The experimental setup for testing the PS-MCP is displayed in Fig. 2.4. In this test setup, α -particles are emitted from a ^{226}Ra α -source towards the surface of the electron

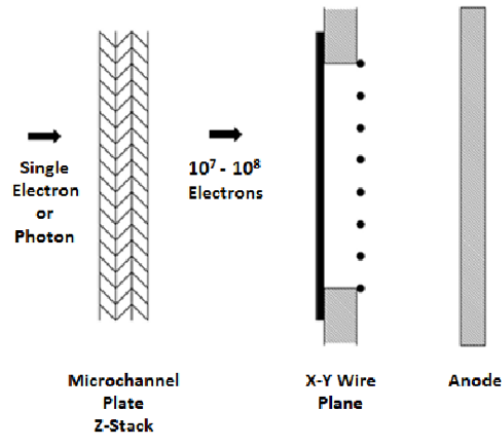


FIGURE 2.3: Cross-sectional view the PS-MCP Detector [1].

emission foil ($0.5 \mu\text{m}$ thick mylar foil with 12 nm of gold evaporated onto its front surface). The gold surface on the foil allows a voltage to be applied to the foil. After passing through the electron emission foil the α -particle is detected in a surface-barrier silicon detector situated behind the foil. Detection of the α -particle allows one to trigger the data acquisition system only on detected electrons coincident with the α -particle. Passage of the α -particle through the electron emission foil results in ejection of an electron. The ejected electron is accelerated by a potential difference between the accelerating wire harp and electron emission foil towards the MCP Z-Stack. The electron is then incident on the front of the MCP, where it is amplified to a gain of 10^7 - 10^8 electrons [1]. This electron cloud then passes through two wire harps. The wire harps are orthogonal to one another, so that position can be extracted for both the x and y dimensions. As the electron cloud passes the wire planes it induces a signal onto the wires.

Each wire in the wire plane is connected to a tap of a delay line, as shown in Fig. 2.2. Once the signal arrives at the delay-line junction, the signal splits and propagates to each end of the delay line. The propagation time to each end of the delay line depends on the position of the wire sensing the signal. One can get an improved position resolution by utilizing the timing difference between the two ends of the delay line. The signal induced by passage of the electron cloud splits when it reaches the delay line. The time of arrival

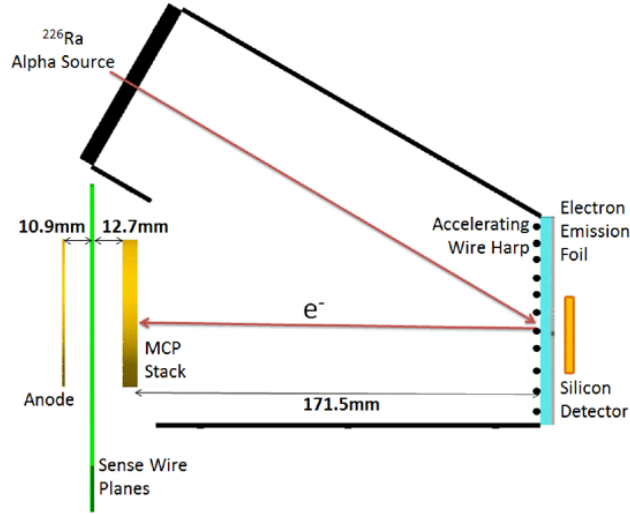


FIGURE 2.4: Experimental setup for testing PS-MCP Detector v1.0 [1].

of the induced pulse at either end of the delay line depends on which wire the induced signal was present on. Thus, position information is encoded as a time difference by the delay line. The second wire harp and its associated delay line provide position in the orthogonal direction. Arrival of the electron cloud at the anode provides a timing signal for the detection of the particle.

Typical signals are shown in Fig. 2.5 where the red and blue traces correspond to the induced signals observed at the two ends of the same delay line. The signals were digitized using a 12/14 bit CAEN v1729a waveform digitizer. This digitizer has a sampling frequency of 2 GS/s and an analog bandwidth of 300 MHz. The induced signals were amplified by a $\times 30$ low noise amplifier prior to being digitized. As is clearly evident, in contrast to the unipolar shape of the anode signal, the induced signal has a bipolar shape. The anode has a negative, unipolar signal because the anode collects negatively charged electrons. The signal from the output of the MCP Z-Stack (not shown) looks identical to the anode signal except it is positive in polarity. The negative lobe of the induced signal corresponds to the approach of the electron cloud to the sense wires and the positive lobe corresponds to the recession of the electron cloud from the sense wires. The zero-crossing point is the time at which the centroid of the charge cloud passes the

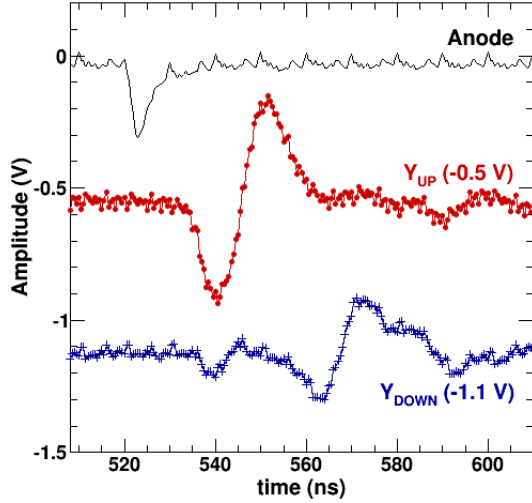


FIGURE 2.5: Signals for two ends of the delay line (red and blue traces) and the anode signal (black trace). Note that the induced signal has been amplified by a low noise RF amplifier (LNA-530, RFBay Inc.). Applied biases include: -1000V on the electron emission foil, 0V on the accelerating grid wires and MCP Z-Stack entrance, +2950V on the MCP Z-Stack exit, +3050V on the sense wires, and +3150V on the anode [1].

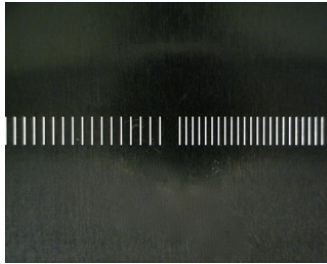


FIGURE 2.6: Potomac Photonics Mask with $50\ \mu\text{m}$ wide and 0.1in tall slits. The mask is made out of 0.003in stainless steel shim stock. The center-to-center spacing of the slits is 0.6mm and 0.9mm respectively [61].

wire plane. The typical transition time from minimum to maximum is 8-10 ns. As the transition from negative to positive values is well defined it can be used to determine the time the electron cloud passes the wire plane.

To determine the intrinsic, spatial resolution of the detector, a 0.003 in thick stainless steel mask with a well-known pattern of slits was placed between the electron-emission foil and the MCP. The mask was placed 0.15 in in front of the MCP Z-Stack entrance. The mask, fabricated by laser micromachinery, is displayed in Fig. 2.6. It has slits that

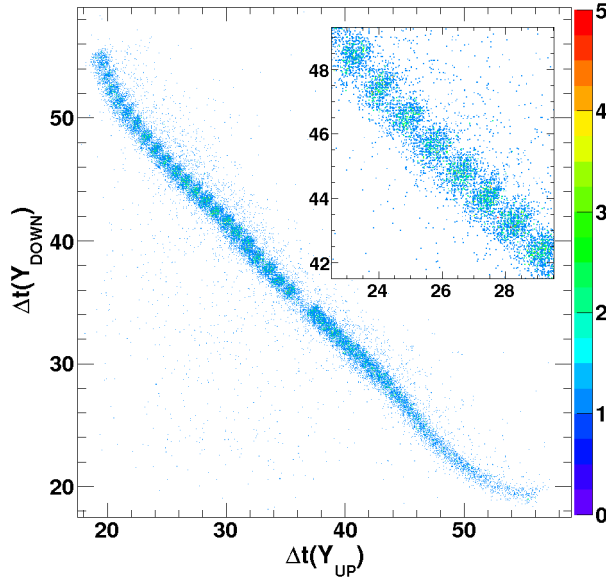


FIGURE 2.7: Two-dimensional time correlation between two ends of the delay line while the MCP front entrance is masked. Both $\Delta t(Y_{UP})$ and $\Delta t(Y_{DOWN})$ are time differences between the anode signal and the zero point crossing of the induced signal [1].

are $50 \mu\text{m}$ wide and 0.1 in long. After extracting the time for each end of the delay line relative to the anode signal, the correlation between the time of one end and the other end is constructed. This time correlation is shown in Fig. 2.7. This allows one to determine the position of each incident particle.

TABLE 2.1: Position resolution that follows each successive improvement to the position resolution [1].

| Step | FWHM (μm) |
|------------------------------------------|------------------------|
| 1. Raw | 526 |
| 2. FFT + Double pulse rejection (DPR) | 475 |
| 3. FFT + DPR + Transition time selection | 466 |

The time correlation exhibits peaks (clearly visible in the inset of Fig. 2.7, with each peak corresponding to a given slit in the mask). By projecting onto the line defined by the observed peaks, one obtains the position for each incident ion. The position resolution obtained is $526 \mu\text{m}$. To improve the resolution, the raw signal is processed by a Fast Fourier Transform (FFT) algorithm, and frequencies above 150 MHz were rejected. The

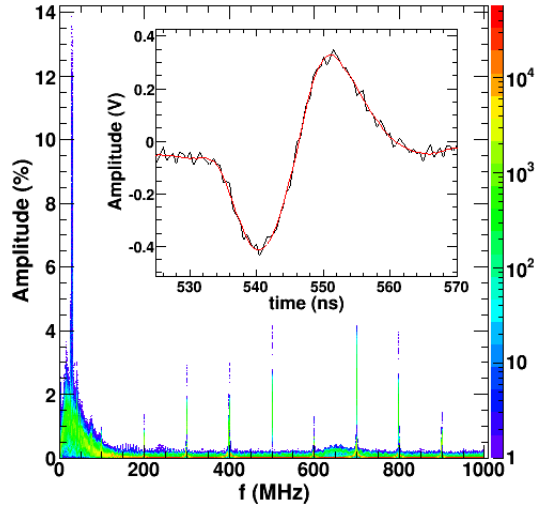


FIGURE 2.8: Two-dimensional histogram of signal amplitude vs. frequency for 30,000 Yup signals. The inset shows the raw induced signal (black) and the FFT filtered signal (red). The envelope extending out to 150 MHz are the dominant components of the induced signal, while the peaks occurring every 100 MHz after 200 MHz are noise [1].

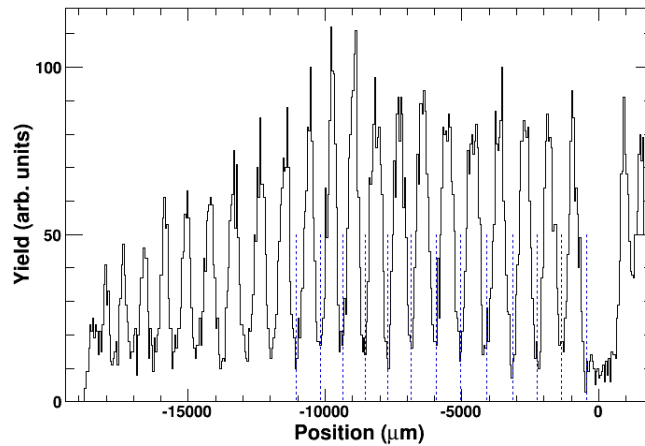


FIGURE 2.9: One-dimensional position spectra of electrons incident on Potomac Photonics mask with 50 μm wide slits. The induced signals has been processed by a FFT filter. The blue dashed lines show the minima of the peaks [61].

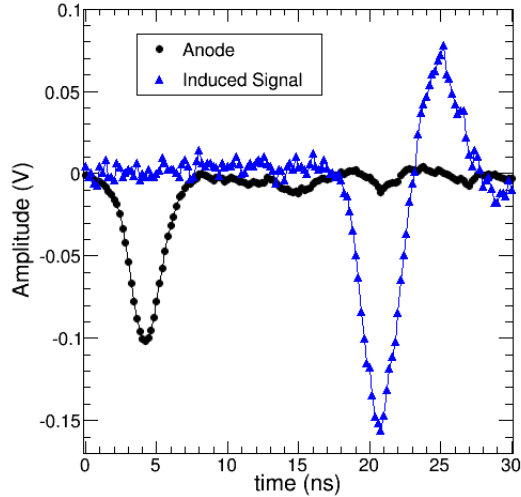


FIGURE 2.10: Typical digitized waveforms for the anode and induced signals from the single wire board. Note that the induced signal has been amplified by a low noise RF amplifier (LNA-530, RFbay Inc.).

red trace, displayed in the inset of Fig. 2.8, corresponds to the inverse Fourier Transform after this filtering of its frequencies. A one-dimensional position spectrum is depicted in Fig. 2.9.

The resolution is further improved by rejecting atypically wide anode-signal pulses, or double triggers from the MCP. In addition, the transition time from the minima to maxima on the induced signals is analyzed, and signals with a transition time of 3 ns or less are rejected. The resulting position resolution is $466 \mu\text{m}$. These improvements in the position resolution are summarized in Table 2.1.

2.1.3 Individual wire readout

As just described, it has been demonstrated that the MCP-sense wire (MCP-SW) detector v1.0 can achieve a spatial resolution as low as $466 \mu\text{m}$. However, one puzzle in characterizing the performance of the prototype detector was the variation in transition times observed in the signals. While typical transition times of 8-10 ns were measured,

transition times as fast as 4 ns were also observed. To disentangle the inherent characteristics of the induced signal from any distortions due to the delay line in which the signal propagates, we built a single wire readout. This sense wire plane was not tapped to a delay line, rather individual wires were independently read out for a limited number of wires. Typical signals observed for this individual wire readout configuration are shown in Fig. 2.10. From this test, rise times of the inherent signals could be measured in the absence of signal dispersion (or other distortion) from the delay line. The signals in Fig. 2.10 were taken with a digital oscilloscope (Tektronix TDS 3054C/ 500 MHz bandwidth) linked to the single wire board. The transition time from the minimum peak to the maximum peak is approximately 4 ns, which is faster than the typical reported transition times to 8-10 ns [1]. The rise time of the induced signal was approximately 2 ns, which is pertinent information to the inherent nature of the induced signal on the sense wire plane.

To understand the variation in transition times for detector v1.0, we built a single wire readout PCB. The single wire board demonstrated much of the variation in transition times is due to signal dispersion (or distortion) in the delay line. This reduction in the transition time and more importantly the reduction in its variability, suggested that an improvement in position resolution could be achieved with a second generation detector. Prior to developing such a detector, it was necessary to develop essential “tools” to aid the project. The two central “tools” developed were a dedicated wire winder and high vacuum test station. These “tools” are discussed in the sections to follow.

2.1.4 Design and construction of a wire winder and vacuum test station

In order to efficiently produce sense wire planes it was necessary to construct a compact wire winder dedicated to the project. Testing different detector designs required

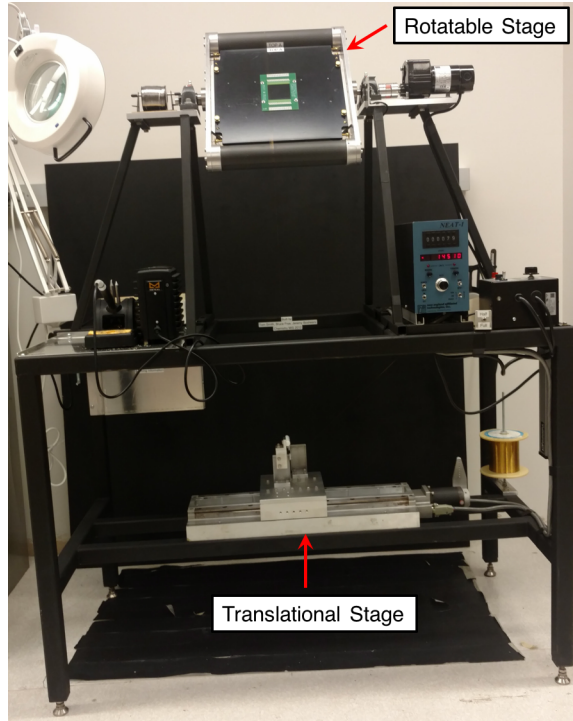


FIGURE 2.11: The wire winder with its major components labeled.

development of a dedicated vacuum test station. The development of these tools, necessary for the project, is summarized in this section.

2.1.4.1 Wire winder

The purpose of constructing a wire winder is to be able to self-sufficiently create wire harps, which provide the sense wire plane central to the detector design. In the past, winding of wire planes relied on a technician external from our research group. Based on the availability of this technician and the wire winding machine, there were often delays in realizing a new sense wire plane. Furthermore, the wire winder that the technician used was oversized ($\sim 1.5 \text{ m} \times 1.5 \text{ m}$), and thus wasted a considerable amount of an expensive wire (\$1600/spool).

To overcome this obstacle in the project we developed a compact, efficient wire winder that is dedicated to the project. A photograph of the wire winder with its rotational and translational stages labeled is displayed in Fig. 2.11. The wire winder is composed of a rotatable, vertical stage with an active area of 25 cm x 28 cm, which coils a wire around its surface. The wire typically used is a 25.4 μm diameter, 99.95% tungsten wire with 0.127-0.254 μm of nickel plating and 0.254-0.508 μm of gold plating. A motor drives the rotatable stage to rotate in a clockwise direction. Once the stage makes one complete revolution, a metal interrupter disrupts the light path of phototransistor-photodiode assembly mounted adjacent to the stage. The phototransistor is biased so as to produce a beam of infrared (IR) light that is sensed by an adjacent photodiode. Disruption of the IR light by the small interrupter causes a voltage drop in the photodiode. The pulse propagates from the photodiode to the Neat-1 Preset Indexer. The preset indexer controls a stepper motor that moves a predetermined number of steps when it receives a pulse. The shaft of the stepper motor is coupled to a precision lead screw that is connected to a translation stage. Translational movement of this stage engages the wire feed mechanism. The wire leading up to the rotatable stage moves in tandem with the stepper motor, so when one full revolution the stepper motor moves the set number of steps. This predetermined number of steps corresponds to the desired wire-to-wire spacing. The minimum wire spacing we are able to wind is approximately 200 μm , which is based on the minimum step size of our stepper motor and the diameter of the wire used.

It is important that tension remain constant in the wire, so that the overlaid wire will be uniformly laid. Otherwise, the accuracy of the wire pitch will be compromised. Thus, the wire must be unwound from the spool and through a tensioner (Fisher Baker Corp. "Cat's Meow" Whisker Despooler). The tensioner maintains a constant tension on the wire being unwound from the spool and prevents against the effect of "ballooning" or rapid acceleration and de-acceleration when a wire is unwrapped from the wire spool.

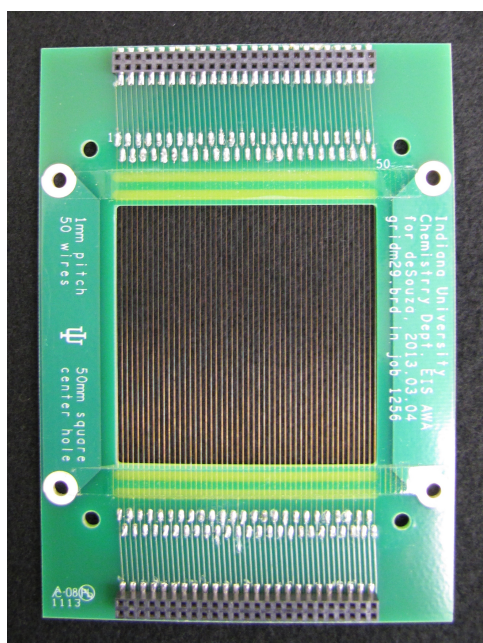


FIGURE 2.12: A photograph of a second generation sense wire PCB.

Once the wire is coiled around the rotatable stage to cover the desired spacing, a plate may be raised up so that the wires are just above a PCB. The plate is raised by unscrewing the screws connecting the plate to the rotatable stage, and then screwing the same screws into a series of adjacent holes. The screws merely push against a metal surface to be raised up. Once the plate has been raised such that the wires are just above the surface of a printed circuit board, one can epoxy the wires to the PCB. Epoxy (Miller-Stephenson Epon 828 and Versamid 140) with low outgassing properties was chosen because our sense wire planes will be put in a vacuum chamber. After the epoxy cures, attaching the wires to the PCB, one can solder the wires to the appropriate pads on the PCB. A photograph of a second generation sense wire PCB, which had its wires wound using the dedicated wire winder, is depicted in Fig. 2.12.

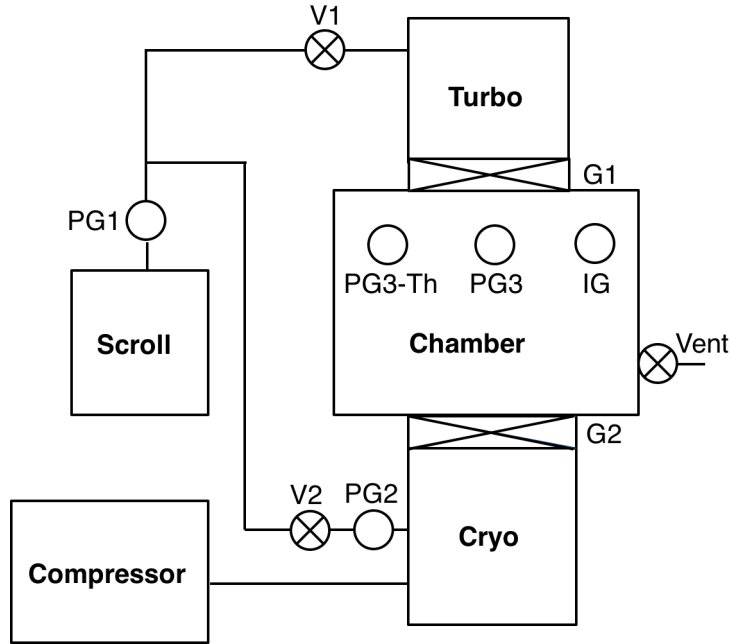


FIGURE 2.13: Schematic drawing of the vacuum test station. The vacuum is monitored by pressure gauges (PG1, PG2, PG3, and PG3-Th) and a hot-filament ionization gauge (IG). Gas flow is controlled by the manual valves (V1 and V2), gate valves (G1 and G2), and a vent valve (Vent).

2.1.4.2 Vacuum test station

A high vacuum test station was designed and constructed specifically for this project. All of the work presented in Section 2.1.2 and 2.1.3 was performed in another vacuum chamber. Main drawbacks of the old vacuum chamber included: (a) it was an oil-based system and (b) it was inefficient for insertion and removal of the detector. Use of an oil-free based system is problematic as it reduces , which the lifetime of the MCPs. The vacuum station designed for this project was chosen to be oil-free and capable of maintaining a pressure of $< 10^{-7}$ torr over an extended period of several months. Moreover, the new vacuum test station is designed so that insertion and removal of the detector is an efficient and safe process and requires only a single individual.

As previously described, the operation of MCPs requires high vacuum with a pressure below 5×10^{-6} torr. Moreover, due to the hydrophilic nature of the MCP plates,

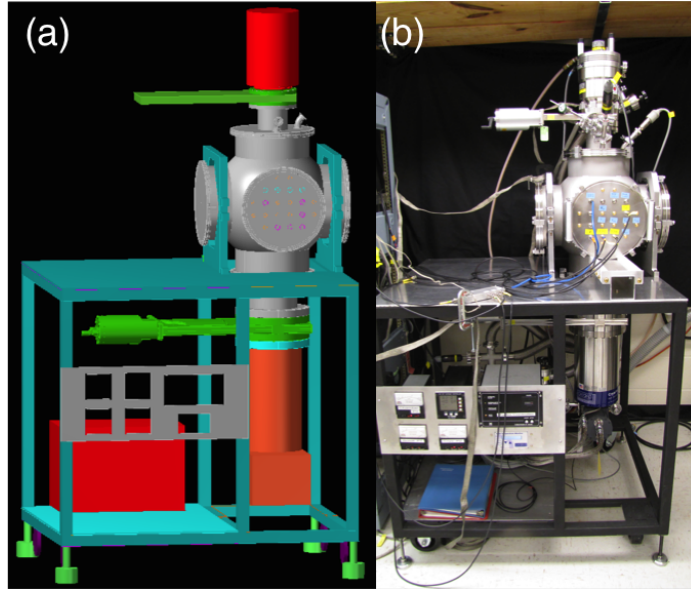


FIGURE 2.14: Panel a) CAD drawing of the proposed vacuum test station. Panel b) Photograph of the implemented vacuum test station.

their storage when not in use also requires a good vacuum environment. The vacuum test station is composed of the following major components: ISO250 six-way cross, scroll pump (Edwards nXDS15i 100l240V), turbomolecular pump (Oerlikon Leybold TMP 360 CSVG), and cryogenic pump (Austin Scientific Cryoplex 8 and Model 125 Compressor). A schematic drawing of the vacuum test station is shown in Fig. 2.13. The scroll pump is used to establish rough vacuum in the chamber, and to back the turbomolecular pump (turbopump) during its operation. Once the chamber has been roughed out to a pressure of less than 100 mtorr, the turbopump is used to evacuate the chamber to high vacuum. After the turbo pump has evacuated the chamber to a pressure of approximately 2×10^{-5} torr, the cryogenic pump (cryopump) is used and the turbopump is valved off from the chamber and is allowed to spin down. This limited use of the turbopump not only improves the noise characteristics of the test chamber, but also extends the lifetime of the turbopump. Under normal operating conditions, a cryopump evacuates the vacuum test station to a pressure as low as 4.0×10^{-8} torr. A photograph and CAD drawing of the vacuum test station can be seen in Fig. 2.14. To monitor the pressure, we use a

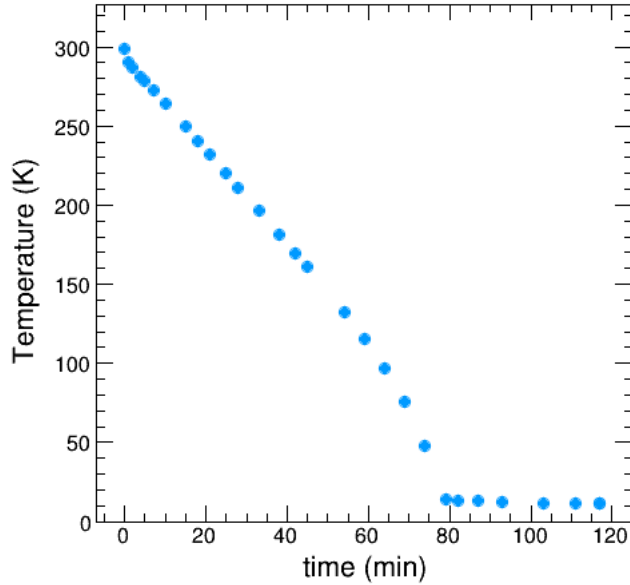


FIGURE 2.15: Time required for cool down of cryogenic pump.

combination of Pirani thermal conductivity sensors (HPS Products Series 315 Pressure Sensor), an extended-range Pirani thermal conductivity sensor (Thyracont VSR53DL), and one hot-filament ionization gauge (HPS Products 10047) in the chamber.

The time required for cryopump cool down is 1 hour and 20 minutes, as shown in Fig. 2.15. Pump down curves were measured with our PS-MCP detector inside the vacuum test station. We varied (a) the conditions for how long the chamber and detector were at atmospheric pressure, as well as (b) whether we vented the chamber with air or nitrogen. Furthermore, pump down curves for the chamber can be seen in Fig. 2.16. The longer the chamber is at atmospheric pressure, the longer it will take to re-establish high vacuum in the chamber. While at atmospheric pressure or while venting with air, water vapor adsorbs to the chamber walls. The best practice is to have the chamber at atmospheric pressure for as little time as possible, so that there is less time for water vapor to adsorb to the chamber walls. To minimize wear and tear on the cryogenic pump, we pump down to the low 10^{-5} torr regime with the turbopump before switching to the cryogenic pump. Venting with nitrogen is cleaner than using air from the room

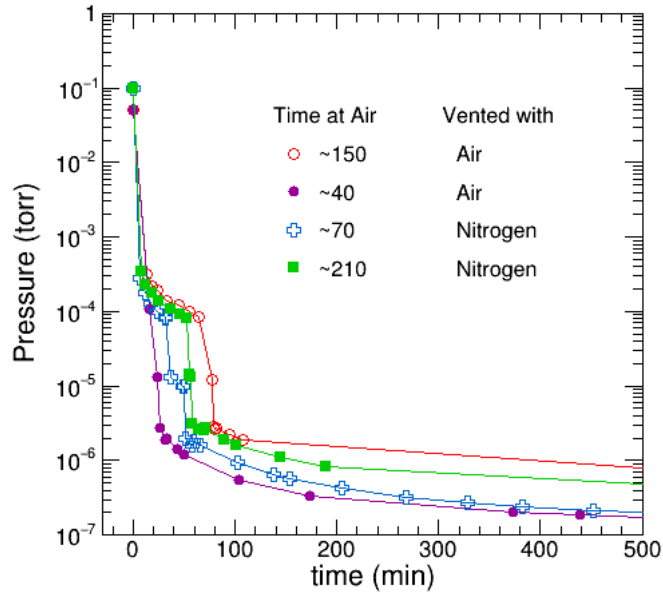


FIGURE 2.16: Pump down curves under multiple conditions. The time at air is the time the vacuum test station was at atmospheric pressure. Air or nitrogen was used to vent the vacuum test station.

and reduces absorption of water vapor onto the chamber walls. We make modifications to our detector as often as multiple times a week and this requires breaking vacuum; so, minimizing pump down time is important. As a result, we typically vent with industrial grade nitrogen (Airgas NI 300). One can see from the Fig. 2.16 that when the chamber is at air for a long time, venting with nitrogen is preferred. We have found that when you are 40 min. at air, there is little difference between pump down time for nitrogen and air.

In this detector development project, as we often make changes to our detector, it is important to have an efficient system for moving our detector in and out of vacuum. A significant amount of effort was expended in designing the test station to ensure easy access to the detector. The front flange of the chamber has a shelf screwed to it and the PS-MCP detector is secured to this shelf. If we have a minor change to make to the detector, we can simply vent the chamber, and pull the detector out onto its resting block, and make the change as shown in Fig. 2.17. Even changes requiring total access to the detector are not difficult to realize. The detector is easily slid out of the vacuum chamber

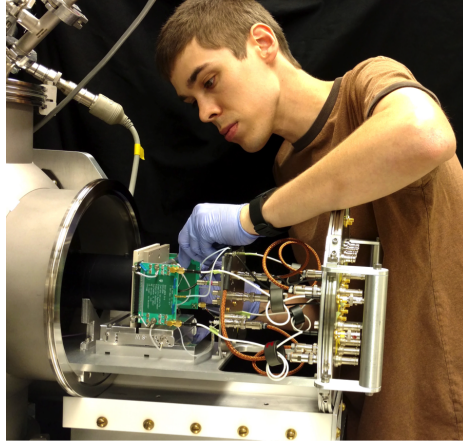


FIGURE 2.17: Close up of Blake Wiggins making a small change to the PS-MCP Detector while the detector is placed on its resting block.

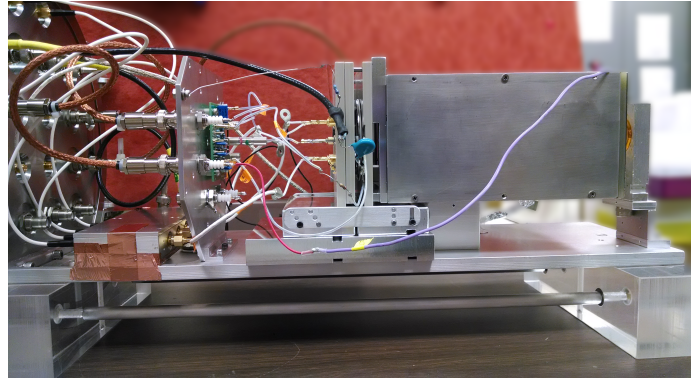


FIGURE 2.18: Side view of PS-MCP detector. The detector is resting in its plexiglass resting block on the lab bench top.

and stabilized on the bench top within a plexiglass holder. This holder facilitates working with the detector on bench top as can be seen in Fig. 2.18. Typically only one individual is necessary to remove the detector from vacuum, work on the detector, and re-insert it into the vacuum test station. It typically takes 4 hours between the start of pumping on our chamber to when we can bias our detector.

2.1.5 Achieving high spatial resolution with the MCP-SW detector v2.0

A second generation MCP-SW detector using the induced signal approach has been realized. To assess the spatial resolution, the masked detector was illuminated by electrons. The initial, measured spatial resolution of $276 \mu\text{m}$ FWHM was improved by requiring a minimum signal amplitude on the anode and by employing digital signal processing techniques. The resulting measured spatial resolution of $119 \mu\text{m}$ FWHM corresponds to an intrinsic resolution of $98 \mu\text{m}$ FWHM when the effect of the finite slit width is deconvoluted. This measurement is a substantial improvement from the previously reported spatial resolution of $466 \mu\text{m}$ FWHM using the MCP-SW v1.0 detector in Section 2.1.2. To understand the factors that limit the measured resolution, the performance of the detector is simulated (see Section 4.3).

2.1.5.1 Experimental setup and description of MCP-SW v2.0

The overall concept for the induced signal approach is illustrated in Fig. 2.19. An electron of sufficient energy impinges on the front of a MCP and ejects an initial electron. This electron is amplified by a MCP Z-stack to an electron cloud consisting of $1 \times 10^7 - 1 \times 10^8$ electrons. This electron cloud is accelerated past a sense wire harp, which consists of parallel wires mounted on a PCB. The induced signals are inherently bipolar, where the negative and positive lobes of the induced signal correspond to the approach and recession of the electron cloud relative to the sense wires respectively. The zero-crossing point in the induced signal is the time at which the centroid of the electron cloud passes the wire harp. As indicated in Fig. 2.19, the electron cloud sensed by the wires propagates to the delay line where the signal splits. The time difference between the two signals arriving at the ends of the delay line is related to the position of the electron cloud. When the electron cloud is closer to the top of the detector, as indicated in Fig. 2.19, the arrival of the Y_{up}

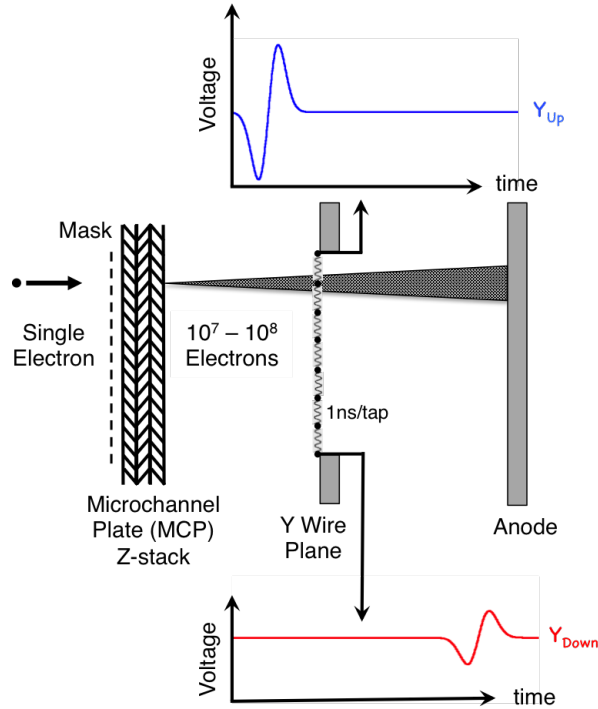


FIGURE 2.19: Cartoon illustrating the concept used in the induced signal MCP-SW detector.

signal precedes that of the Y_{down} signal. Consequently, the Y_{up} signal is less attenuated and experiences less dispersion in the delay line as compared to Y_{down} . After passing the wire harp, the electron cloud is collected on a stainless steel anode. This metal anode preserves the excellent timing properties associated with non-position sensitive MCPs, and will be used as a reference time in the subsequent analysis.

There were several changes in the transition from the MCP-SW detector v1.0 to v2.0. A schematic drawing of the experimental setup of the MCP-SW detector v2.0 is shown in Fig. 2.20. A surface barrier detector (SBD) (Ortec TO-020-300-300-S) was replaced with a PMT (Burle 8575), where each acts as detector for α -particles. We opted to use a readily available PMT because it had a larger active area than the SBD. Note that the SBD has an active diameter of 20 mm, the PMT has an active diameter of 50.8 mm, and the MCP has an active diameter of 40 mm. Moreover, the PMT was mounted

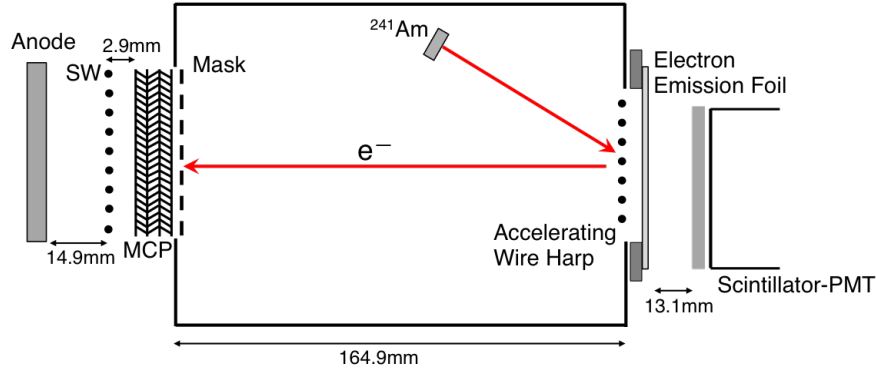


FIGURE 2.20: Experimental setup used to test the position sensitivity of the MCP-SW detector.

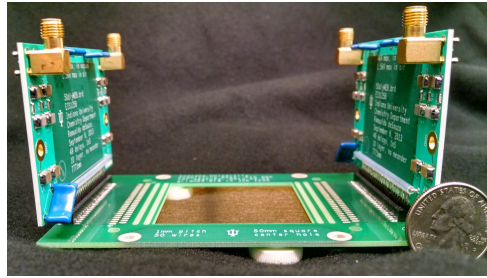


FIGURE 2.21: Photograph of the sense wire board coupled to delay line boards. Either a single delay board can be used to readout all fifty wires or two delay boards can be utilized to read out the even and odd wires independently.

outside of the vacuum chamber, which allows for a more efficient method of replacing the PMT should the need arise. A ^{226}Ra alpha emitter was used beforehand, but we transitioned to using a ^{241}Am alpha emitter ($1.42 \mu\text{Ci}$).

To realize the induced signal concept in a more compact geometry with a more efficient testing arrangement, a new PCB was fabricated. This sense wire board has an outer dimension of $\sim 8 \times 12 \text{ cm}^2$ with a $50 \times 50 \text{ mm}^2$ cutout. Across this cutout, 50 gold-plated tungsten wires with a diameter of $25 \mu\text{m}$ are strung with a 1 mm pitch using standard wire winding techniques. To efficiently read out this sense wire harp, a delay line is utilized thus minimizing the number of signals required to provide spatial information. The delay line consists of a continuous 7771 mm long trace on a 10 layer

Rogers 4350 PCB with ~ 1.14 ns/tap. The width of the trace was chosen to be 0.122 mm to maintain 50 Ω impedance. Construction of the delay line with a high quality PCB material, such as Rogers 4350, is essential to minimize signal degradation. In contrast to the first generation detector [1], this MCP-SW detector decouples the sense wire board from the delay line board. This decoupling makes the detector more compact as shown in Fig. 2.21.

The decoupling has the disadvantages of more connections (socket on the SW PCB and male connector on delay PCB) and longer traces from the wire harp to the delay tap. The decoupled delay board also replaces the serpentine delay line with a continuous trace. The change increases the complexity of the PCB fabricated from a six layer board to a ten layer board. One advantage of separating the delay line onto an independent PCB facilitates the efficient testing and implementation of different delay line designs without implementing a new sense wire plane. In addition, it allows the use of two delay boards to read out even and odd wires independently. In the following work, although two delay boards were connected to the sense wire plane due to limited number of digitizer channels available, only the signals from the even numbered wires were acquired and analyzed. Subsequent test of odd wire readout alone yielded comparable results. The first step in testing this new SW plus delay line readout was to see if the spatial resolution of 466 μm could be reproduced. This spatial resolution was replicated, which indicates that the changes to the continuous trace, the added connections, and the increased length from SW to delay board did not impact the performance of the detector. The following sections cover the optimization of the MCP-SW v2.0 detector.

Depicted in Fig. 2.20 is the experimental setup used to determine the spatial resolution of the MCP-SW detector. Alpha particles from a ^{241}Am radioactive source impinge on a secondary electron-emission foil. Passage of an α -particle through the 1.5 μm thick aluminized, mylar foil results in the ejection of electrons. Alpha particles that traverse

the aluminized, mylar foil are detected by a fast scintillator/photomultiplier tube (PMT) assembly placed directly behind the aluminized foil. Typically, ~ 6 electrons are ejected from the foil [20, 62]. These electrons are ejected with anywhere from 0.1–100 eV, with the most probable value of 3 eV (see [63] for energy and angular distributions). The ejected electrons are accelerated to an energy of ≈ 1 keV before drifting in a field free region for 16 cm and illuminating a stainless steel mask. This energy for the electron was chosen due to the high MCP detection efficiency of 50–85% (see Table 1.1). The mask is mounted directly to the entrance MCP bias ring, which is 1 mm upstream from the MCP active area. The precision mask, fabricated by laser micro-machining [64], has ten slits each measuring $50 \mu\text{m}$ by $7620 \mu\text{m}$ and spaced by either 4.2 or 4.5 mm apart. Electrons that pass through slits in the mask are amplified by the MCP stack and are subsequently detected by the sense wire harp. The MCP used was a standard Z-stack MCP (APD 340/6/5/12 D 60:1) with $5 \mu\text{m}$ diameter microchannels [4].

The entire assembly presented in Fig. 2.20 is housed in a vacuum chamber that is evacuated to a pressure of 4×10^{-8} torr. The entrance of the MCP stack was held at ground, while the MCP exit and sense wires (SW) were biased to potentials of +2528 V and +2755 V respectively. Both MCP and sense wires were biased using a ISEG NHQ224M low-noise, high voltage power supply (HVPS). The anode was biased to +2805 V using a ISEG NHQ226L HVPS. The secondary electron-emission foil and PMT (Burle 8575) were biased to voltages of -1000 V and -1800 V using a HK 5900 and Bertan 362 HVPS respectively. The signals arriving at either end of the delay line are designated Y_{up} and Y_{down} . Each of these signals was amplified by a custom built low-noise amplifier (gain = 30, bandwidth = 150 MHz) before being digitized by the Tektronix DPO5204 oscilloscope, which is a 10 GS/s waveform digitizer with 8 bit resolution and an analog bandwidth of 2 GHz. The signal from the anode was amplified by an RF Bay LNA-530 amplifier (gain = 30dB, bandwidth = 500 MHz) before being digitized to provide a common time reference for the sense wire signals. The digitizer was triggered using a

coincidence between the MCP signal and the PMT signal in order to reduce background events due to radiogenic decays in the MCP. The MCP signal used for the trigger was first inverted with a 100 MHz inverting transformer and subsequently amplified by an RF Bay LNA-530 Amplifier. Both the MCP and PMT signals were discriminated using a leading-edge discriminator (Lecroy 821) before forming the coincidence. The full electronics diagram is presented in Fig. D.2.

2.1.5.2 Measuring the spatial resolution of the MCP-SW detector

To minimize inherent noise on the induced signals, various grounding methods were explored. The optimal grounding configuration, which was crucial in realizing the best resolution, involved attaching aluminum standoffs between the ground of the evens and odds delay boards. Use of these standoffs with a bus wire running in between provided a means to symmetrically ground the entire system. The ground from both the MCP and anode signal readout/high voltage PCB was coupled to the center point between delay board standoffs. The ground of the sense wire PCB was also attached where end end of a standoff attached to the delay line board. Moreover, high frequency noise from each induced signal was mitigated by using an RF choke on each of the signal cables (between the delay board output and the front flange of the vacuum station). It was also determined that this noise did not arise from coupling of the sense wires with the anode. This was determined by increasing the distance between the anode and the sense wires. There was no change in the amplitude of the noise when the SW-anode distance was increased from ~ 15 mm to ~ 45 mm.

Initially the zero-crossing point of the digitized, induced signal was utilized to determine the position, but it was subsequently realized that selecting the time associated with 50% of the positive lobe amplitude was superior to the zero-crossing point as it was less susceptible to noise. The anode signal provides a common time reference for the

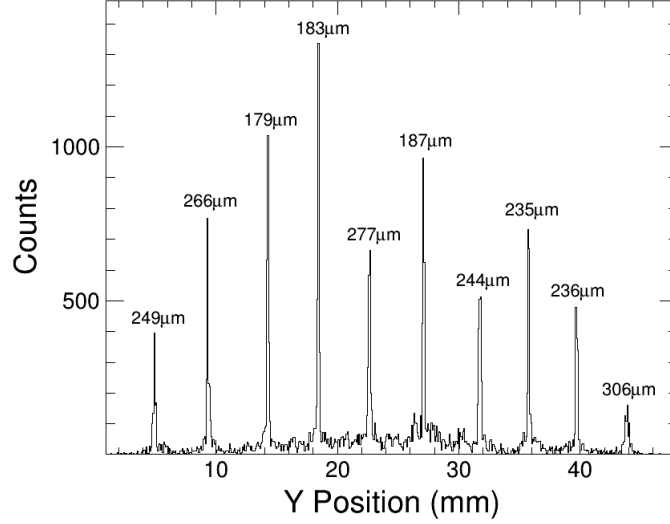


FIGURE 2.22: One-dimensional position spectrum of electrons incident on MCP through the calibration mask. The induced signals were filtered using and FFT (as described in the text). Slits in the mask are separated by 4.2 or 4.5 mm. The resolution (FWHM) of a given peak is indicated directly above the peak.

delay time measurement. This reference time is defined by utilizing a software CFD at the 75% level. No advantage is observed by lowering the value of the CFD. The time difference between each induced signal time and the anode time is designated Δt_{Yup} and Δt_{Ydown} .

The two-dimensional correlation between Δt_{Yup} and Δt_{Ydown} is constructed (see Fig. 2.7 for an example) and rotated to the $(\Delta t_{Ydown} + \Delta t_{Yup})$ vs. $(\Delta t_{Ydown} - \Delta t_{Yup})$ reference frame. The quantity $(\Delta t_{Ydown} - \Delta t_{Yup})$ reveals the image of the slits in the mask. This image is position calibrated using the known center-to-center spacing of the slits and a third degree polynomial with the equation:

$$Y = 1.6 \times 10^{-8}y^3 + 1.8 \times 10^{-6}y^2 + 4.2 \times 10^{-2}y + 24.4 \quad (2.1)$$

After calibration, the relative deviation of the data from the fit, $(\text{data} - \text{fit})/\text{fit}$, is at most 2%. Individual slits (from bottom to top) have a deviation of: 1.08, 1.44,

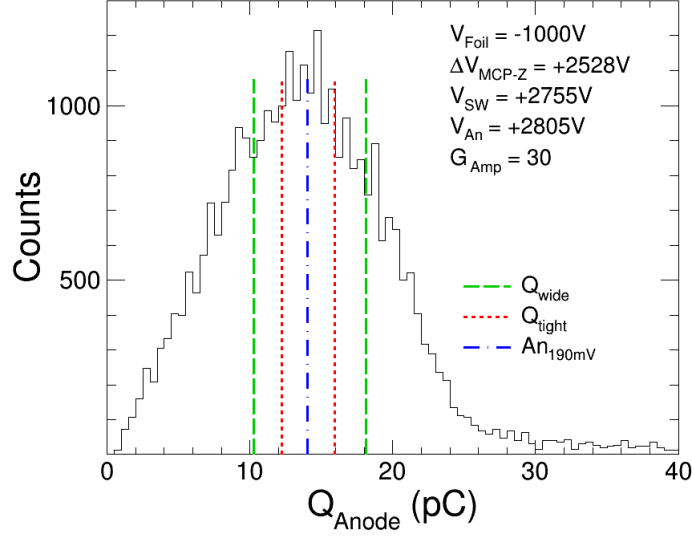


FIGURE 2.23: Total charge distribution measured using the anode signal. The long dashed line (green) and the short dashed line (red) correspond to the charge gating conditions described in the text. The dash-dot line (blue) corresponds to the charge associated with a -190 mV amplitude anode signal.

-1.98, 0.20, 1.40, 0.42, -1.08, -0.46, 0.20, and 0.22%. The resulting Y-position spectrum is depicted in Fig. 2.22. A total of ten peaks in the position spectrum are clearly resolved, corresponding to the slits in the mask. The average width of the peaks in the spectrum, $\langle \sigma_{\text{statistical}} \rangle$, was utilized to determine the spatial resolution. Based on the Gaussian-like nature of the peaks, the average FWHM was calculated using $\text{FWHM} = 2.35 \cdot \sigma$ for the nine peaks with $Y < 42$ mm. The peak, at $Y \approx 44$ mm, was not used in the reported average because of a lack of statistics in this peak once more stringent selection criteria were applied. Using this approach the spatial resolution of the detector was determined to be $276 \mu\text{m}$ FWHM. An improvement was made by applying a FFT filter with a cutoff frequency of 150 MHz. This cutoff frequency was chosen to eliminate high frequency noise as indicated in 2.8. This filtering improved the spatial resolution to $228 \mu\text{m}$ FWHM. The spatial resolution was further improved by selecting events with $56 \text{ ns} < (\Delta t_{Y_{\text{down}}} + \Delta t_{Y_{\text{up}}}) < 60 \text{ ns}$ because points that lie out of this range correspond to spurious events where the delay-line length is not constant. With this requirement the spatial resolution

improved to $202 \mu\text{m}$ with a rejection of 20% of the events.

Further improvements to the spatial resolution were made by selecting on events with a narrow charge distribution. The total charge of the electron cloud, as measured using the anode signal, is displayed in Fig 2.23. We elected to utilize a charge cut as a means to suppress both radiogenic decays, originating from impurities in the MCP glass, and pileup events. Radiogenic decays can initiate an avalanche anywhere in the depth of the MCP. The deeper the initial point of the electron avalanche, the less amplification occurs. Consequently, the rejection of small signals suppresses radiogenic decays. In contrast, pileup events are inherently associated with larger charge. Selection of the peak in Fig. 2.23 correspondingly minimizes both radiogenic decays and pileup events. A selection, Q_{tight} , was made on the center of the peak from 12.3 to 15.9 pC, as indicated by the red, short dashed line. By the use of FFT filtering, the delay sum criteria, and the Q_{tight} charge cut the spatial resolution was improved to $136 \mu\text{m}$ FWHM with a rejection of 80% of the events. Decreasing the width of the charge cut did not further improve the spatial resolution. In contrast, relaxing the charge selection to the Q_{wide} charge cut of 10.3–18.1 pC, as indicated by the green, long dash lines in Fig. 2.23, resulted in a spatial resolution of $168 \mu\text{m}$ FWHM with a rejection of 64% of the events.

Requirement that the amplitude of the anode exceeded -190 mV in addition to the requirement that the delay length was a constant resulted in the best resolution achieved. This threshold criteria led to an increase in the amplitude of the induced signals from a mean peak-peak amplitude of 34 mV to 50 mV. The charge corresponding to this threshold of -190 mV is depicted as the blue dot-dashed line in Fig. 2.23. Application of the FFT filtering, the delay sum criteria, and the threshold criteria resulted in a resolution of $119 \mu\text{m}$ FWHM. Imposing these conditions resulted in a rejection of 71% of the total events. The digital signal processing performed on each induced signal for the optimal spatial resolution of $119 \mu\text{m}$ FWHM is shown in Fig. 2.24. The impact of FFT filtering

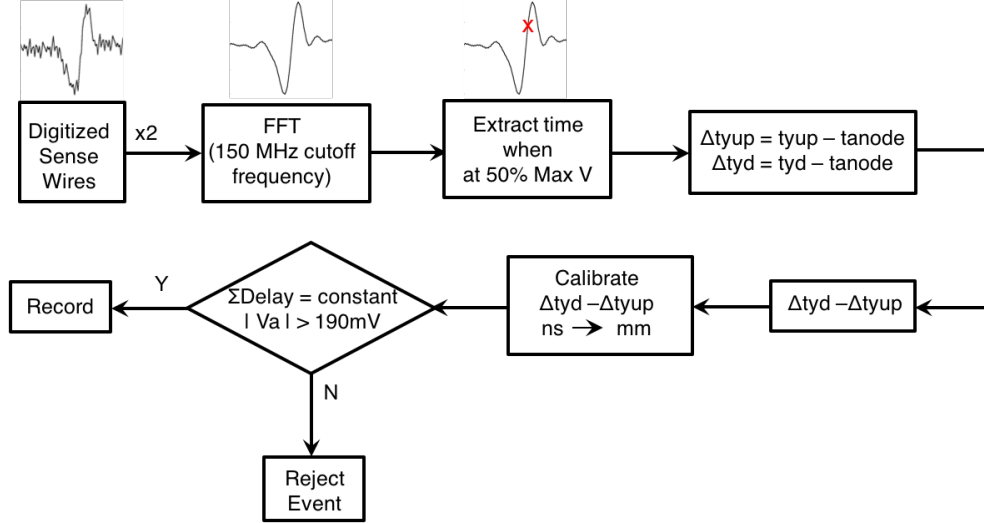


FIGURE 2.24: Schematic illustrating the complete procedure utilized to extract the optimal position resolution with the sense wire signals. The red marker denotes the 50% point of the positive lobe.

on the induced signal is evident in Fig. 2.24. The position spectrum with these selection criteria is presented in Fig. 3.17.

TABLE 2.2: Spatial resolution achieved for different stages in the analysis along with the intrinsic resolution.

| Condition | FWHM (μm) | % Rejected |
|---------------------------------------|------------------------|------------|
| 1. Raw | 276 | 0 |
| 2. FFT | 228 | 0 |
| 3. FFT+ ΣDelay | 202 | 20 |
| 4. FFT+ ΣDelay +Qwide | 168 | 62 |
| 5. FFT+ ΣDelay +Qtight | 136 | 80 |
| 6. FFT+ ΣDelay +An<-190 | 119 | 71 |
| Intrinsic of Condition 6 | 98 | 71 |

The measured spatial resolution corresponds to the convolution of the intrinsic spatial resolution of the detector with the finite slit width. To extract the intrinsic resolution, the effect of the finite slit width was de-convoluted from the measured resolution for the nine peaks with $Y < 42$ mm. The position resolution measured corresponds to the convolution of the intrinsic position resolution with the finite slit width. The measured

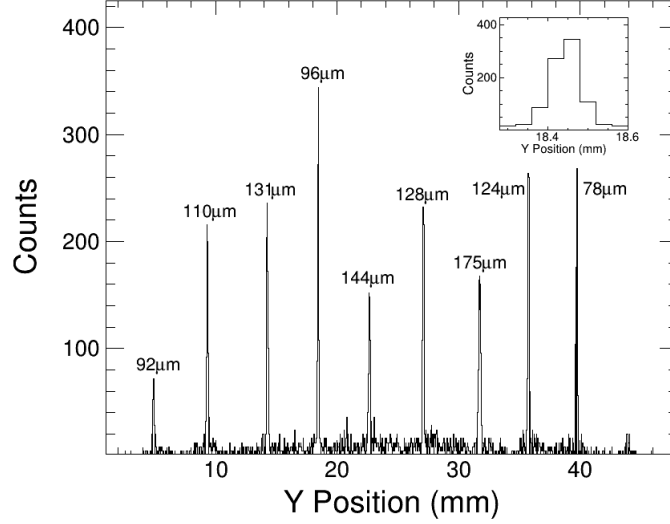


FIGURE 2.25: One-dimensional position spectrum using the delay sum and the threshold criteria (described in the text) of electrons incident on MCP through the calibration mask. Slits in the mask are separated by 4.2 or 4.5 mm. The resolution (FWHM) of a given peak is indicated directly above the peak. Shown in the inset is a zoom in of one of the peaks.

resolution $M(Y')$ is given by:

$$M(Y') = \int G(Y')I(Y')dY' \quad (2.2)$$

where $G(Y')$ is taken as a step function with a width of 50 μm to represent the slit, and $I(Y')$ is a gaussian with the intrinsic width, $\sigma_{intrinsic}$. By varying the intrinsic width the impact of the finite slit width on the measured resolution can be determined. Using this approach an average intrinsic resolution of 98 μm FWHM was extracted. The spatial resolution and the corresponding percentage of rejected events for each condition described are summarized in Table 3.3.

2.1.5.3 Measuring the spatial resolution of the MCP-SW detector with 5 and 2 GS/s digitization

The impact of using a lower sampling frequency on spatial resolution was also investigated. The data from the previous section was modified such that only every other sample was read in and used in the subsequent analysis, thus resulting in an effective sampling frequency of 5 GS/s. With use of the same data treatment, the spatial resolution increased to an average, measured spatial resolution of $159 \mu\text{m}$. This increase in measured resolution from $119 \mu\text{m}$ is unsurprising considering the position is measured using a time measurement. Next, we considered what resolution could be achieved with an even lower sampling frequency of 2 GS/s. We elected to use the CAEN v1729A digitizers, which have 14 bits as compared to the 8 bit Tektronix DPO5204 oscilloscope. The full electronics diagram is shown in Fig. D.1. The digital signal processing included: digitizing the induced signal waveforms, performing an FFT with a frequency cutoff of 150 MHz, performing a linear interpolation to step in a time steps of 0.05 ns, taking the derivative of the signal, performing an FFT with a cutoff frequency of 500 MHz, and extracting the maximum of the derivative signal. The maximum of the derivative corresponds to the zero-crossing point of the induced signal, which becomes our t_{Yup} and t_{Ydown} . The data processing following this time extraction is the same as that described in the previous section. The measured spatial resolution achieved for this processing method with the best gating criteria is $169 \mu\text{m}$ FWHM with a rejection of 77% of the data. Surprisingly, the spatial resolution only decreased by $10 \mu\text{m}$ when the sampling frequency decreased from 5 GS/s to 2 GS/s.

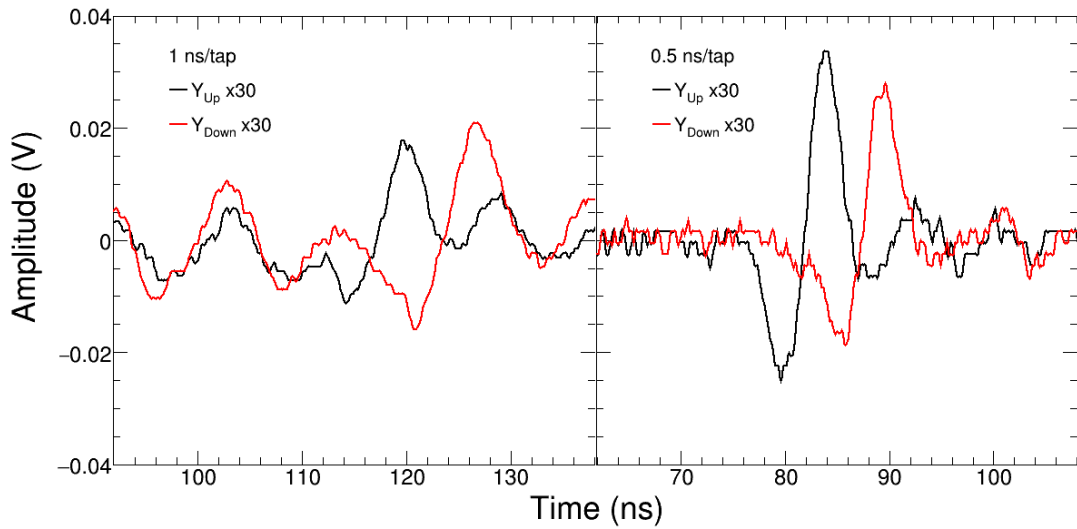


FIGURE 2.26: Digitized waveforms of edge events for each delay board. The delay boards with 1ns/tap and 0.5ns/tap are shown.

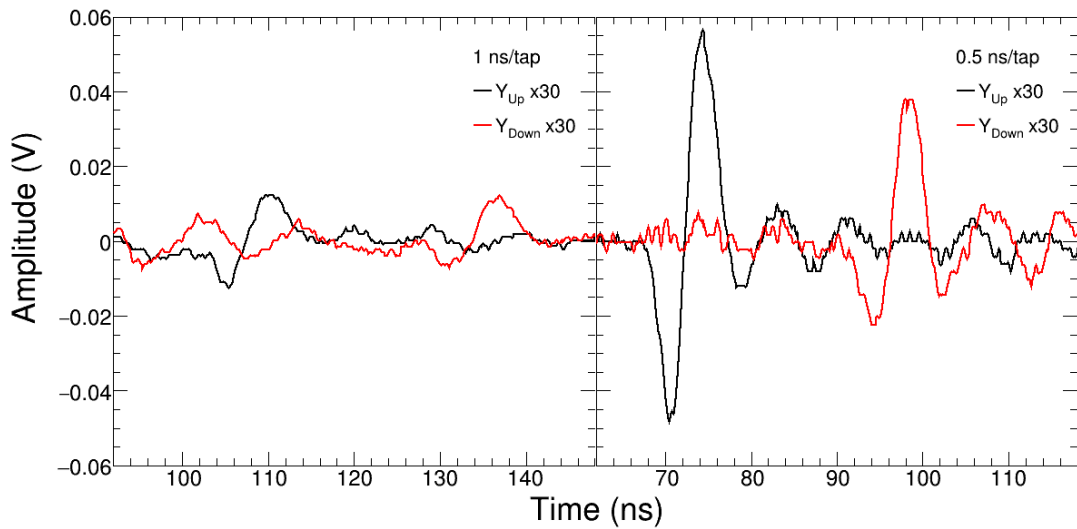


FIGURE 2.27: Digitized waveforms of edge events for each delay board. The delay boards with 1ns/tap and 0.5ns/tap are shown.

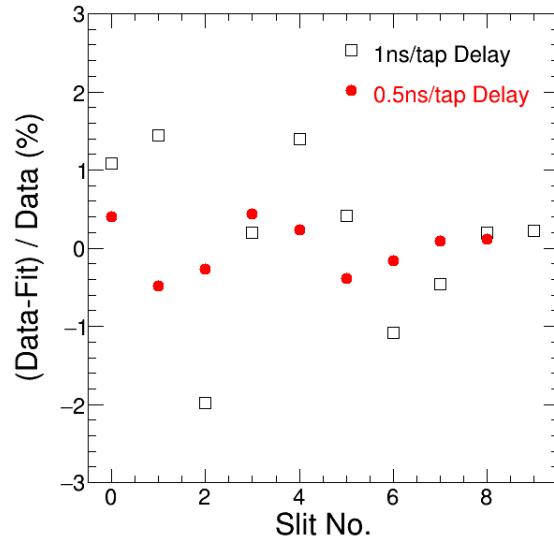


FIGURE 2.28: Comparison of MCP-SW linearity for the 1ns/tap to the 0.5ns/tap delay boards.

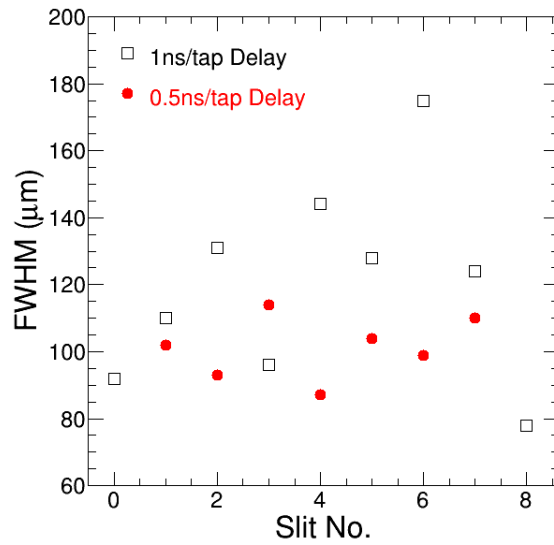


FIGURE 2.29: Comparison of MCP-SW spatial resolution for the 1ns/tap to the 0.5ns/tap delay boards.

2.1.5.4 Measuring the spatial resolution of the MCP-SW detector using 0.5ns/tap delay boards

Even though we were able to achieve 98 μm FWHM resolution with the 1ns/tap delay boards, the signal-to-noise (S/N) was fairly poor for particles arriving at both the edge and middle of the detector. As a result, we fabricated delay boards with half the delay length, which are subsequently termed the 0.5ns/tap delay boards. Digitized waveforms for both delay board lengths are shown in Fig. 2.26 for a middle event and Fig. 2.27 for an edge event.

With use of the 0.5 ns/tap delay boards, the linearity improved greatly from $\pm 2\%$ to $\pm 0.5\%$ as shown in Fig. 2.28. The linearity is defined as the relative deviation from the fit, when calibrating from time (in channel number) to Y position. This is improved because the signals are less sensitive to noise fluctuations with the lower overall attenuation. As a result, we opted to go back to using the zero-crossing point of the induced signals for the 0.5ns/tap case when defining the time. Surprisingly, the obvious improvement to the S/N of the signals did not improve the intrinsic spatial resolution. Shown in Fig. 2.29, is the measured spatial resolution as a function of slit number for both the 1 ns/tap and 0.5 ns/tap delay boards. The slit numbers are numbered with the bottom to top of the detector. Slit number is used instead of Y position because a second generation mask was used in the 0.5 ns/tap measurement.

Both masks were made by laser ablation [64]. In the case of the 1 ns/tap delay boards, the precision mask has ten slits each measuring 50 μm by 7620 μm and spaced by either 4.2 or 4.5 mm apart. In contrast the 0.5 ns/tap delay board, the precision mask has nine slits each measuring 25 μm by 2 mm and spaced by 4.5 mm apart. Using a mask with narrower slits decreases the count rate of α generated electrons on the detector, but also minimizes the uncertainty of assigning an intrinsic resolution based on the measured

resolution. If the slit width is small relative to the intrinsic resolution of the detector, then the measured resolution is equivalent to the intrinsic resolution, which was the motivation for use of the $25\ \mu\text{m}$ mask. The average measured and intrinsic resolution for the 0.5 ns/tap boards was $99\ \mu\text{m}$ whereas the average intrinsic resolution for the 1 ns/tap delay boards was $98\ \mu\text{m}$. But the uncertainty for assigning the resolution has greatly improved from $\pm 50\ \mu\text{m}$ to $\pm 15\ \mu\text{m}$. It would be preferable to compare the variation of each delay boards using the same generation mask, but at present that measurement has not been made.

To see if 10 GS/s digitization was still limiting the spatial resolution of the approach, data was acquired using 20 GS/s digitization. The electronics for this arrangement can be found in Fig. D.3. This required use of a new digitizer, the Keysight MSOS804A oscilloscope. Otherwise, the setup and analysis was identical to the 10 GS/s case with 0.5ns/tap delay boards. The resulting spatial resolution was $102\ \mu\text{m}$ FWHM, and as a result 10 GS/s sampling was determined to be the fastest digitization required for the induced signal approach. Furthermore, the sampling frequency of 10 GS/s is not the fundamental limit defining the spatial resolution of the induced signal approach. This result, can be understood in terms of the fastest transition times of 2 ns meaning that ~ 20 points are digitized over this time interval, which is sufficient to accurately characterize the zero-crossing point.

2.2 Resistive anode technology

2.2.1 Prior work with resistive anodes

To explore how the shape of the induced signal depends on position we elected to use a resistive anode (RA) positioned behind the wire harp, so that the centroid of the electron cloud measured by the RA could be used to characterize the corresponding induced

signals. A RA was chosen to provide the position measurement as it is a simple and cost effective means to provide the required position information. Clearly, the better the resolution achieved for the RA, the more precisely the dependence of the induced signal on position can be investigated. The space necessary to position the wire harp between the MCP and the RA prevents minimization of the MCP to RA distance and hence limits the optimal resolution achievable [65]. This section focuses on the optimization of the RA. Unfortunately, the RA was unable to be used in conjunction with the sense wires as it led to a large capacitive coupling of its signal to the sense wires positioned in front of it.

Using the resistive anode approach, good spatial resolution, $50 \mu\text{m}$ (FWHM), has been achieved with 1000 incident photons/s [52]. However, achieving this level of resolution required a 5-stack MCP consisting of a chevron detector followed by a Z-stack with a decelerating potential between them. For the simpler arrangement of a single chevron detector, a position resolution of $134 \mu\text{m}$ (FWHM), has been achieved with incident photons [66]. For the case of a single incident electron, when a ^{63}Ni β^- source was used to irradiate a stack of two chevron MCPs, a resolution of $250 \mu\text{m}$ (FWHM) was achieved [42]. Detection of a single electron, ion, or photon represents the ultimate in sensitivity. Providing good position resolution at low levels of signal-to-background can impact several applications. For this reason, the present work focuses on determining the spatial resolution achievable for low-intensity signals using a single Z-stack MCP. Efforts to optimize the resolution of the RA for our experimental test setup will be described.

2.2.2 Spatial resolution with the standard charge division method

The experimental setup utilized to determine the position resolution of the MCP-resistive anode (MCP-RA) detector, is depicted in Fig. 2.30. A $1.4 \mu\text{Ci}$ ^{241}Am α -source (**A**) was oriented so that some of the emitted α particles strike a $1.5 \mu\text{m}$ thick aluminized,

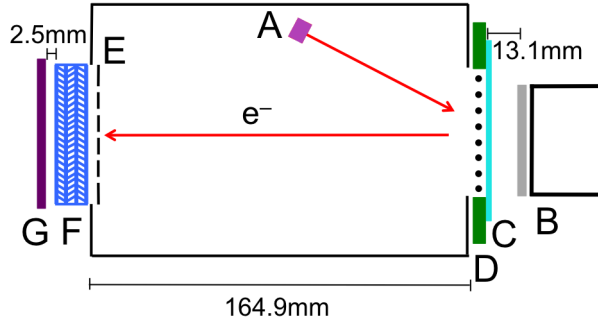


FIGURE 2.30: Schematic illustration of the experimental setup. Indicated in the setup are **A**: ^{241}Am source, **B**: scintillator with PMT readout, **C**: secondary electron-emission foil, **D**: accelerating wire harp, **E**: mask, **F**: Z-stack MCP, and **G**: RA.

mylar foil (**C**) biased to -300 V. This foil acts as a secondary electron-emission foil. After ejecting electrons, α particles traverse the foil and are detected in a fast, plastic scintillator read out by a photomultiplier tube (Burle 8575). Typically 6 electrons are ejected from the foil [20, 62]. These electrons are accelerated towards a wire harp (**D**) held at a potential of $+1000$ V. The electrons are then transported within a metallic conduit and after passing through a metallic mask (**E**) are incident on the front face of the $10\ \mu\text{m}$ -pore Z-stack MCP (Photonis APD 3 40/12/10/12 D 60:1) [4]. The conduit serves to shield the electrons from stray electromagnetic fields. The entrance of the 40 mm diameter MCP (**F**) is held at ground potential, while the exit of the MCP is typically biased to a voltage of $+3139$ V. The MCP amplifies the incident electrons to 5×10^6 - 7×10^7 electrons. After exiting the MCP stack, these electrons are accelerated towards the RA (**G**) [36] which is typically biased to a potential of $+3286$ V, where electrons are collected. This entire assembly is housed in a vacuum chamber that is evacuated to a pressure of 4×10^{-8} torr.

Using this experimental setup a high count rate of 2.1×10^4 counts sec^{-1} was initially observed on the MCP. It was speculated that the origin of this high count rate was α -particles striking the metallic conduit and ejecting electrons. To test this hypothesis, we biased the conduit to a potential of $+1000$ V. With this background suppression we achieved a count rate of 580 counts sec^{-1} on the MCP active area of ≈ 12 cm^2 . Concerns

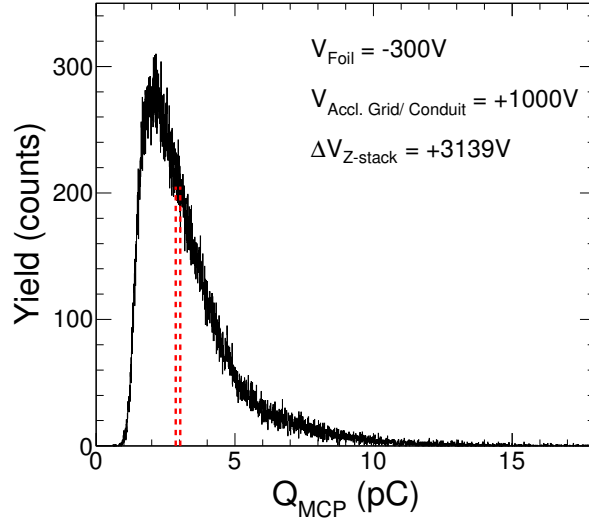


FIGURE 2.31: Pulse height distribution of total charge measured at the exit surface of the MCP. The dashed (red) line corresponds to the gating condition described in the text.

about sparking to the MCP front surface prevented us from biasing the conduit to a higher voltage. Electrons were detected in the MCP in coincidence with a PMT signal at a rate of $480 \text{ counts sec}^{-1}$. We therefore deduce that the background rate with the conduit biased is $\approx 100 \text{ counts sec}^{-1}$. Absent the conduit and α source the detector itself has a background rate of $60 \text{ counts sec}^{-1}$ principally due to the radiogenic decays in the detector.

Charge arriving at the four corners of the RA is processed by high quality charge sensitive amplifiers (CSAs) [67]. These CSAs are located in vacuum approximately 6 in away from the RA. The output signals from the CSAs were shaped by commercial shaping amplifiers (Tennelec 241S). The best resolution was obtained for an integration time of $1 \mu\text{s}$. The amplitude of the resulting semi-gaussian signal from each corner of the RA was digitized using a peak-sensing ADC (CAEN V785) [68]. The magnitude of the four resulting charges were designated Q1, Q2, Q3, and Q4. When viewed from the entrance surface of the MCP detector, the signal designated Q1 corresponds to the upper left corner of the RA and the remaining signals follow a clockwise orientation. The gains

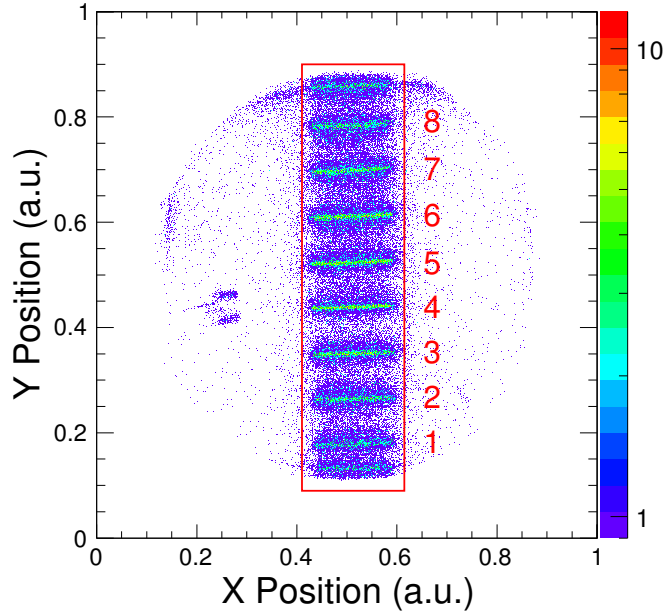


FIGURE 2.32: Two-dimensional position spectrum resulting from illuminating the masked MCP detector with electrons from the secondary electron emission foil.

of the four CSAs and shaping amplifiers were normalized by injecting a known charge into one corner of the RA and measuring the response at the remaining corners. Following amplification by a fast amplifier (x14.5), the charge at the exit surface of the MCP was measured using a fast QDC (CAEN V862) [68]. The coincidence of the MCP and PMT signals was used to both gate the ADC and QDC as well as trigger the computer readout in the PC-based VME data acquisition system. The full electronics diagram is presented in Fig. D.4.

To determine the spatial resolution, a mask was attached to the front mounting ring of the MCP detector ≈ 1 mm from the entry surface. This mask consisted of a $76\mu\text{m}$ thick sheet of stainless steel in which ten slits were produced by laser ablation [64]. The slit dimensions were $100\mu\text{m} \times 7620\mu\text{m}$. Adjacent slits were spaced by either 4.2 mm or 4.5 mm and spanned the active area of the MCP detector. As the slit area corresponds to approximately 0.6% of the active area, the probability for a single electron passing through the slits is small. Depicted in Fig. 2.34 is the schematic of the RA along with

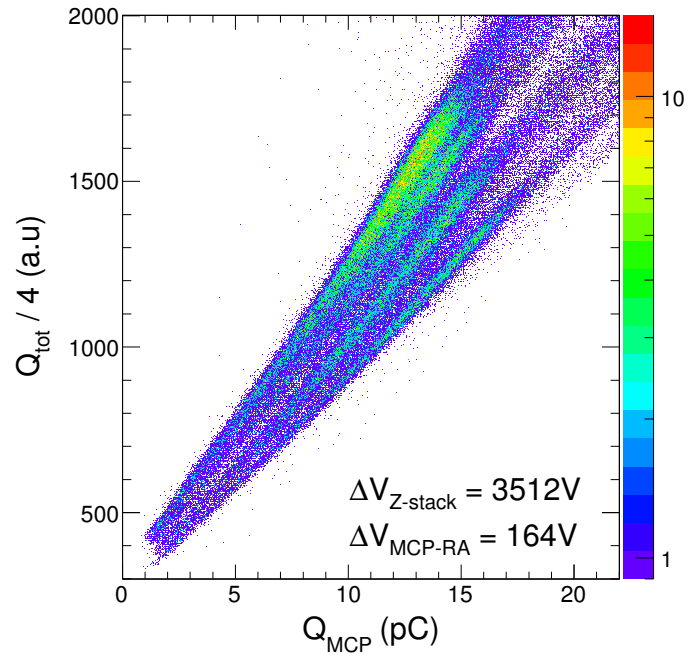


FIGURE 2.33: Two-dimensional spectrum demonstrating the relationship between Q_{MCP} and Q_{tot} .

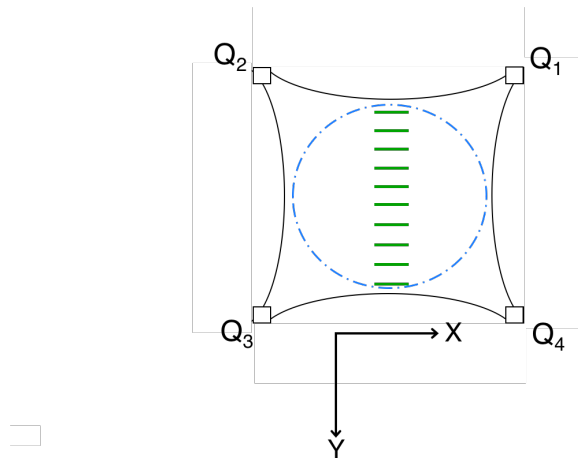


FIGURE 2.34: Schematic of the RA with designations for Q_1 – Q_4 listed. The outline of the 40 mm MCP and the slits in the stainless steel mask are also depicted.

the location of the slits in the mask and the active area of the MCP.

The centroid of the electron cloud in a Cartesian coordinate system was calculated according to the following equations [40, 42]:

$$X = \frac{Q_1 + Q_4}{Q_{tot}} \quad (2.3)$$

$$Y = \frac{Q_1 + Q_2}{Q_{tot}} \quad (2.4)$$

where Q_{tot} is the total charge, calculated by summing the charge of the four corners. The distribution of total charge produced by the MCP, Q_{MCP} , is shown in Fig. 2.31. The large range spanned is due to the exponential amplification inherent in the MCP detector. The distribution exhibits a broad peak centered at 2.1 pico-Coulombs and has a long tail to larger charge. This long tail has previously been attributed to ion feedback in a channel [51]. However, as this spectral feature persists even after the detector has been exposed to good vacuum for a week, we believe other factors contribute to this long tail. Specifically, the long tail can be understood as the detection of more than one electron, qualitatively consistent with multiple electrons being incident on the masked MCP. These double hits could result from multiple electrons being generated from the electron-emission foil, or from an electron generated from the electron-emission foil simultaneously with an electron generated from a radiogenic decay in the MCP glass. Q_{tot} was used in lieu of Q_{MCP} to calculate the centroid of the charge cloud. in order to avoid the noise and potential non-linearity of the fast amplifier. This choice was made since the high quality CSAs used are less noisy in determining the charge as they inherently integrate the signal as compared to the MCP fast amplifier.

The two-dimensional spectrum of the masked detector is shown in Fig. 2.32. Clearly visible in the spectrum are the ten slits in the mask. The number assigned to each slit is also indicated. Evident at $X \approx 0.25$ and $Y \approx 0.45$ is a “hot spot” in the MCP. The

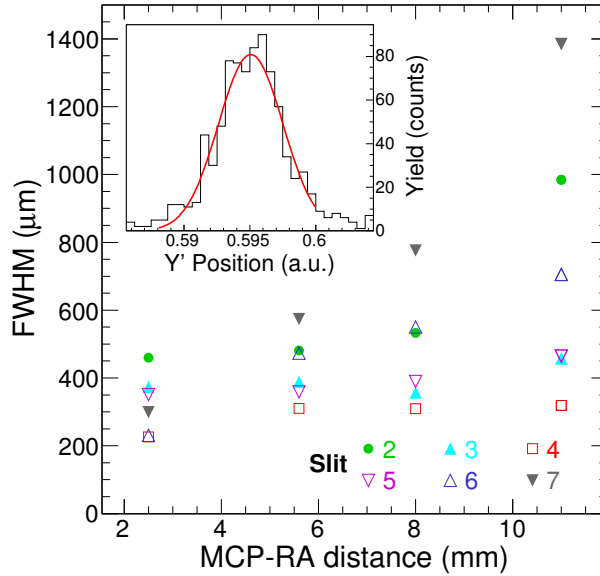


FIGURE 2.35: Dependence of the extracted resolution on the distance between the MCP and the RA for several slits. In the inset, the portion of the Y' spectrum associated with a single slit is shown along with its gaussian fit (red line).

location of this “hot spot” corresponds to a visible crack in the MCP. Outside the region of the slits, a background haze can also be discerned. This background is likely due to radiogenic decays in the MCP itself that survive the coincidence condition. The more intense haze located between the slits is most likely associated with slit scattering from the edge of a slit. The influence of the “hot spot” was eliminated and the impact of the background minimized in the subsequent analysis by selecting only events within the rectangular region indicated in Fig. 2.32. Close examination of Fig. 2.32 reveals that the slit images are not horizontal due to the imprecise placement of the mask in front of the detector. To address this issue the two-dimensional image was rotated by an angle so as to make the two dimensions independent of each other. This rotated two-dimensional image (X', Y') was used in the subsequent analysis.

We examined whether any charge loss was occurring on the RA as presumably incomplete charge collection would result in poorer position resolution. To address this question, we examined the two-dimensional spectrum of Q_{tot} vs Q_{MCP} , presented in

Fig. 2.33. Four bands are clearly visible in the spectrum. As Q_{MCP} represents the true charge generated, in some cases less charge is measured by the RA. For positions close to one edge of the RA, the sheet resistance significantly increases for the opposite edge. This results in a longer risetime for the corresponding CSA signal, impacting the charge collection time. Consequently, the $1 \mu\text{s}$ integration time of the shaping amplifier is insufficient to provide complete charge integration. Selection on the top most band in this spectrum guarantees that the complete charge collection occurs on the RA, however it restricts the image to the center half ($\approx 20 \text{ mm}$ diameter) of the RA.

We now turn to examining the dependence of the position resolution on the distance between the MCP and RA, $\Delta V_{\text{MCP-RA}}$, and Q_{MCP} . To avoid restricting our investigation of these factors to only the central region of the RA, we did not impose the condition that $Q_{\text{tot}} \approx Q_{\text{MCP}}$. Instead, a narrow gate in Q_{MCP} as depicted in Fig. 2.31 was applied. Under these conditions, the Y' spectrum was generated to determine the position resolution. This spectrum consists of ten peaks each of which is well described by a gaussian. A typical one-dimensional slit spectrum in the Y' dimension is presented in the inset of Fig. 2.35 for one of the center slits. As evident in the inset, a gaussian provides a good description of the measured distribution. To avoid non-linearities at the detector edge, the eight inner slits were used to provide a linear position calibration. The position resolution was then determined from the width of each of the eight gaussians that fit these peaks.

To explore if the measured resolution depends on the distance between the back of the MCP and the front of the RA (MCP-RA distance), this distance was varied and the resolution was measured. The resulting data are presented in Fig. 2.35. Several trends are evident in the figure. For slits closer to the edge of the detector, such as slits 2 and 7, a marked dependence of the resolution on distance is observed with the FWHM increasing with increasing MCP-RA distance. In contrast, more central slits (slits 3 through 5) do

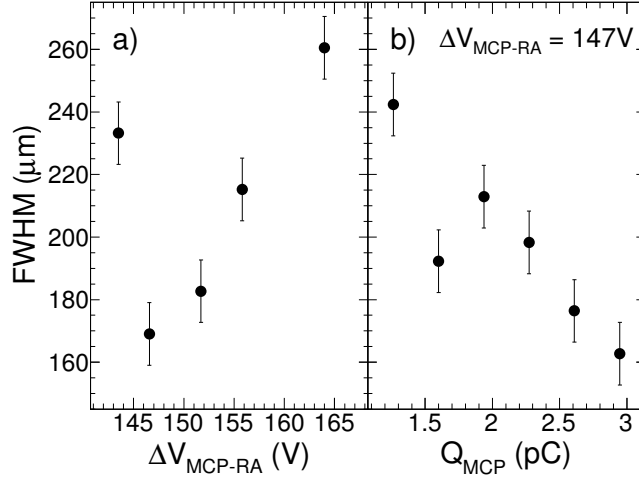


FIGURE 2.36: Panel a: Dependence of the resolution on potential difference between MCP and the RA, $\Delta V_{\text{MCP-RA}}$. Panel b: Dependence of resolution on MCP charge, Q_{MCP} .

not appear to exhibit a systematic dependence of resolution as a function of position. For the closest distance measured, ≈ 2.5 mm, the resolution ranges from 225 μm to 460 μm . It should be noted that as the MCP to RA distance was varied the potential difference between them, $\Delta V_{\text{MCP-RA}}$, was kept constant. Consequently, the electric field decreases significantly as the MCP-RA distance increases. For the remainder of this work, a MCP-RA distance of 2.5 mm was used to characterize other factors impacting resolution. As the emphasis of the subsequent investigation was obtaining the best resolution, the condition that $Q_{\text{tot}} \approx Q_{\text{MCP}}$ was enforced.

An important factor impacting the size of the electron cloud, is electron-electron repulsion as the cloud propagates to the RA. However, as the position resolution obtained utilizes charge centroiding, a larger charge cloud does not necessarily adversely impact the measured resolution. To experimentally determine if electron-electron repulsion plays a significant role in the measured resolution we fixed the MCP-RA distance at 2.5 mm and varied the voltage between the MCP exit surface and the RA. The resulting resolution is presented in Fig. 2.36a. In the range explored a clear minimum exists when $\Delta V_{\text{MCP-RA}} \approx 147$ V corresponding to a field of ≈ 59 V/mm. The error bars shown in

Fig. 2.36a depict the variation in resolution with $2 \text{ pC} < Q_{\text{MCP}} < 4 \text{ pC}$. At this potential an average resolution of $\approx 170 \text{ }\mu\text{m}$ is measured across the central region of the detector. At the edges of the detector a resolution of $\approx 250 \text{ }\mu\text{m}$ is obtained for this potential. As evident in Fig. 2.36b when the potential $\Delta V_{\text{MCP-RA}}$ is increased to $\approx 165 \text{ V}$ (66 V/mm), the resolution deteriorates to $\approx 260 \text{ }\mu\text{m}$ in the central region. Lowering the potential from the optimal value results in a rapid increase in the measured resolution. This result is consistent with the following physical picture. Electrons are emitted from the rear surface of the MCP detector with a distribution of initial velocities. Subsequent acceleration minimizes the spread of these initial velocities in the direction of the RA, hence compressing the electron cloud in that dimension. This compression is associated with a larger electron-electron repulsion. The use of a retarding potential between a chevron MCP and Z-stack MCP [51] to achieve a resolution of $50 \text{ }\mu\text{m}$ is consistent with the present result [52, 53]. The dependence of the observed resolution on the total MCP charge is indicated in the right panel of Fig. 2.36. Overall, an essentially linear trend is observed with the resolution improving from $213 \text{ }\mu\text{m}$ to $170 \text{ }\mu\text{m}$ as the Q_{MCP} increases from 1.9 to 2.9 pC . The measured resolution of $170 \text{ }\mu\text{m}$ achieved for the present configuration is under the condition of $2.9 \leq Q_{\text{MCP}} \leq 3.0 \text{ pC}$.

The position resolution measured corresponds to the convolution of the intrinsic position resolution with the finite slit width as described in Section 2.1.5.2. Using this approach an intrinsic resolution of $157 \text{ }\mu\text{m}$ (FWHM) is extracted for a corresponding measured resolution of $170 \text{ }\mu\text{m}$. This resolution is in agreement with the previous resolution achieved with a Z-stack detector of $100\text{-}200 \text{ }\mu\text{m}$ [48].

2.2.3 Using pulse shape analysis to improve the spatial resolution

Digital signal processing techniques were employed to investigate the joint use of charge division and risetime analyses for the resistive anode (RA) coupled to a microchannel plate detector (MCP). In contrast to the typical approach of using the relative charge at each corner of the RA, this joint approach results in a significantly improved position resolution. A conventional charge division analysis utilizing analog signal processing provides a position measured resolution of $170 \mu\text{m}$ (FWHM). By using the correlation between risetime and position we were able to obtain a measured resolution of $92 \mu\text{m}$ (FWHM), corresponding to an intrinsic resolution of $64 \mu\text{m}$ (FMHM) for a single Z-stack MCP detector.

2.2.3.1 Experimental setup

Depicted in Fig. 2.30 is the experimental setup used to determine the position resolution of the MCP-RA detector. Further details of the experimental setup can be found in Section 2.2.2. The entire assembly presented in Fig. 2.30 is housed in a vacuum chamber that is evacuated to a pressure of 4×10^{-8} torr. The microchannel plates were biased to a voltage of $+3139 \text{ V}$ using a ISEG NHQ224M low-noise, high voltage power supply (HVPS). The RA was biased to $+3284 \text{ V}$, also using a ISEG NHQ224M HVPS. The secondary electron-emission foil and photomultiplier tube were biased to voltages of -300 V and -1800 V using HK 5900 and Bertan 362 HVPS respectively. Signals detected at each corner of the resistive anode were amplified by a high quality charge sensitive amplifier (CSA) [67] operated in vacuum. The four CSAs are situated approximately 13 cm from the MCP-RA to minimize cable capacitance. The output signals from the CSAs are coupled to a 250 MS/s digitizer (Caen DT5720B) [68]. Readout of the digitizer is triggered by the coincidence of a fast signal extracted from the back of the MCP detector

and the PMT. The full electronics diagram is presented in Fig. D.5. The digitizer is readout by a standard PC and waveforms are recorded for subsequent analysis. For the analysis subsequently described the waveforms associated with a total of 260,000 coincident triggers were recorded.

Indicated in Fig. 2.37 is the reverse pincushion shape of the resistive anode along with the circular outline of the 40 mm diameter MCP detector. Superimposed on the RA is the image of the ten slits provided by the stainless steel mask. The four corners of the MCP-RA are designated Q_1 , Q_2 , Q_3 , and Q_4 as evident in Fig. 2.37. Along with the relative position of the MCP-RA and mask, shown in Fig. 2.37 are the signals measured at two locations on the RA. One set of digitized traces (red solid line) correspond to an electron cloud incident at the the bottom slit of the RA as indicated by the red, solid square. The other set of traces (black dashed-dot-line) correspond to a position close to the center of the RA as indicated by the black, solid circle. The waveforms associated with these two positions are markedly different. When the position signal arises from the center of the detector all the waveforms are essentially the same as is expected. However, when the signal originates at the bottom of the RA, while the two corners nearest the signal exhibit a fast risetime followed by an exponential decay, the upper corners of the RA manifest a significantly slower risetime. This risetime, dictated by the RC of the resistive anode thus provides a measure of the particle's position. Motivated by prior work which utilized the risetime of signals in resistive silicon detectors to achieve position sensitivity in one dimension [69], we elected to characterize the RA waveforms by their risetime. The risetime (RT) of each signal was defined as the time required for the signal to go from 10% to 90% of its maximum value. As the slits in the mask are oriented to probe the Y dimension of the RA, for the remainder of this work we focus on the position information in that dimension.

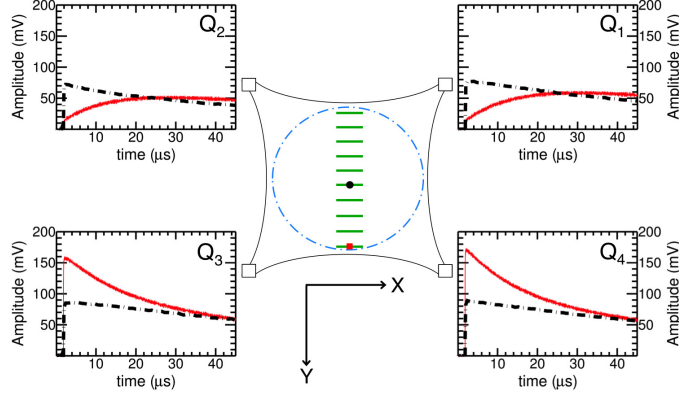


FIGURE 2.37: Schematic of the RA along with the outline of the 40 mm diameter MCP and slits in the stainless steel mask. Pulse shapes associated with the electron cloud incident on two locations of the RA are also shown. Slit 0 (s0) corresponds to the bottom slit and slit 9 (s9) to the topmost slit.

2.2.3.2 Signal risetime analysis

Signals obtained from the CAEN digitizer are processed through a series of mathematical operations using a standard C++ code calling ROOT [70] libraries. In the present investigation the sampling resolution is 4 ns since the digitizer used has a sampling frequency of 250 MS/s. The obtained signals are corrected for the DC offset and gains for different channels for CSA's on an event-by-event basis.

Presented in Fig. 2.38 is the correlation between the risetime observed for signals at the two bottom corners of the RA namely Q_3 and Q_4 . Given the exponential dependence of the signal amplitude on the RC of the resistive anode, the correlation is examined on a logarithmic scale. Individual slits are clearly evident in Fig. 2.38 with low numbered slits exhibiting shorter risetimes and higher numbered slits associated with longer risetimes. An overall linear dependence between $\log(\text{RT}_{Q_3})$ and $\log(\text{RT}_{Q_4})$ is observed as one moves from the bottom of the RA (s0) to the top (s9). Interestingly, a large jump in risetime is observed between slit 5 (s5) and slit 6 (s6), indicating a high sensitivity of the risetime to position in the center of the detector. Moreover, these two slits, in contrast to the other

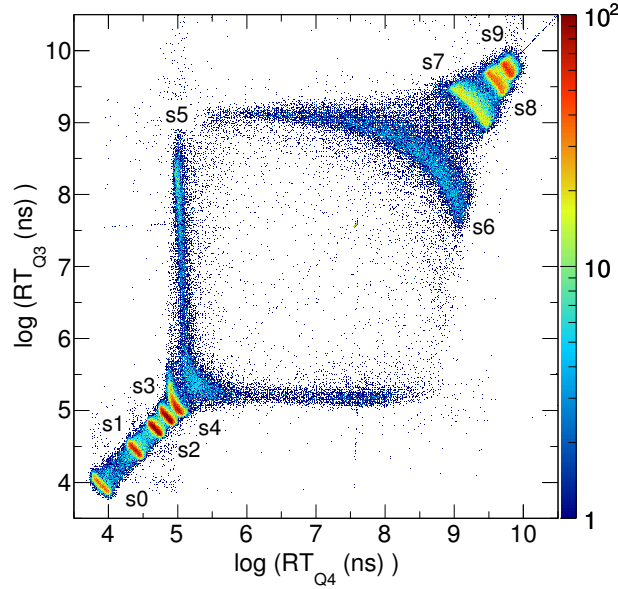


FIGURE 2.38: Correlation between the risetime extracted from CSA output signals for the corners Q3 and Q4. The numbering of the slits is indicated in the figure.

slits manifest a broad range of risetimes in at least one of the two risetimes. Electrons associated with these slits often do not show a strong correlation between the risetime of Q₃ and the risetime of Q₄ as indicated by the horizontal and vertical bands in the figure. Both the large sensitivity to position of the risetime in this region of the detector and the large dispersion in risetime are likely due to the fact that the charge cloud incident in this region experiences near equal resistance in all directions and a relatively small gradient in all directions. For all but these center two slits however the risetime measured for the two corners exhibits a clear anti-correlation. This anti-correlation arises from the spatial extent of each slit in the x dimension. Motivated by the overall positive correlation between $\log(\text{RT}_{Q_3})$ and $\log(\text{RT}_{Q_4})$ we construct the quantity $\log(\text{RT}_{Q_3}) + \log(\text{RT}_{Q_4})$ corresponding to a line of unity slope in Fig. 2.38. It is clearly evident that the spacing of the slits along this line is not uniform.

In Fig. 2.39 the dependence of the summed risetime, $\log(\text{RT}_{Q_3}) + \log(\text{RT}_{Q_4})$, on the position in the Y dimension is explored. The position in the Y dimension is determined

by using the charge division method described in Section 2.2.2. To obtain the charge measured at each corner of the MCP-RA we have utilized digital filtering techniques to provide signal conditioning. We initially used a gaussian filter on the digitized signal to integrate the signal from each CSA resulting in a gaussian-like pulse. The amplitude of this pulse is related to the charge measured at the corner. To efficiently realize the gaussian filter a recursive algorithm was employed [71, 72]. Use of an integration and differentiation time constant of 500 ns was determined to result in the best position resolution. The resolution obtained is comparable to the resolution of 170 μm obtained for this experimental setup with analog electronics described in the previous section. To determine the sensitivity of our result to the filtering technique chosen we also used a trapezoidal filter. Further details on the signal processing can be found in the Appendix A.

Evident in Fig. 2.39 is a clear correlation between the summed risetime and the $Y_{position}$ of the electron cloud. Since $Y_{position}=0$ is associated with the top of the RA, as the value of $Y_{position}$ increases one observes a general decrease in the summed risetime. This trend is understandable since as the position of the electron cloud moves closer to the bottom of the RA the risetime decreases as initially evident in Fig. 2.30. The correlation observed for the upper half of the RA, $Y_{position} < 0.45$ is also observed for the lower half of the RA, $Y_{position} > 0.45$. The fact that the observed locus is not centered on $Y_{position}=0.5$ is likely due to the uncertainty in the positioning of the mask relative to the RA. Situated along the locus of points in Fig. 2.39, that is the main feature of the spectrum, are a series of peaks corresponding to the slits in the mask. An enlarged region centered on slit 3 is displayed in the inset of the figure. The relationship between summed risetime and $Y_{position}$ exhibited by the peaks in 2.39 provides useful information. It describes how these two quantities should be related for a given position of the electron cloud on the RA. Selection of the data in these peaks corresponds to approximately 25% of the data. Aside from the strong locus with peaks visible in Fig. 2.39 one also observes data that does not lie on this locus. The majority of this data is associated with horizontal lines

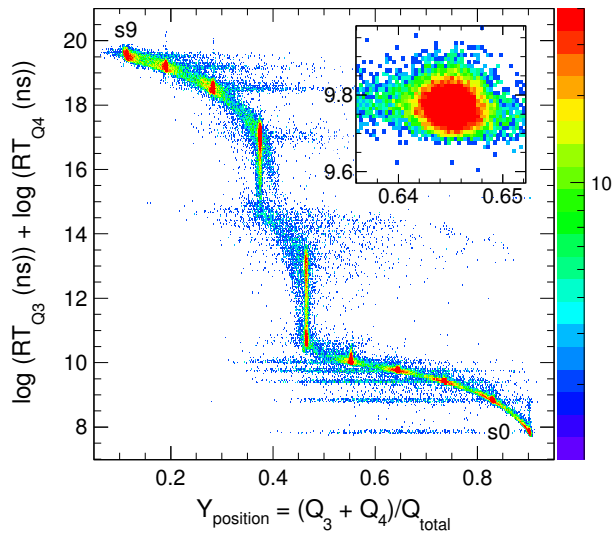


FIGURE 2.39: Dependence of the summed risetime of Q3 and Q4 on the Y position of the electron cloud. The peaks corresponding to slit 0 (s0) and slit 9 (s9) are indicated. The peak associated with slit 3 is presented in the inset.

which originate from one of the ten peaks. Examination of the pulse shapes associated with this data clearly establishes that much of this data is associated with the pileup of two signals. Such a pileup disturbs the baseline for the signal distorting the measured charge while minimally disturbing the signal risetime.

To investigate if using the joint information from the summed risetime together with the charge division method provides an improvement in the position resolution we selected the ten peaks visible in Fig. 2.39. As the resulting distributions are reasonably well described by gaussians, they were fit with this functional form. As the distance between the slits corresponding to each of the peaks is well known the position spectrum was calibrated and the position resolution extracted. The resulting resolution is presented in Fig. 2.40.

To begin we examine the measured resolution where only the charge division technique is utilized for the digitized signals. The result for this case which does not make

use of any risetime information is presented as the cross symbol (green). The resolution obtained from this analysis with the trapezoidal filter is typically $190 \mu\text{m}$ (FWHM). Use of the gaussian filter (not shown) gives a comparable result. As the use of these filters mimics the use of an analog shaping amplifier, also shown for comparison is the resolution obtained from the use of analog electronics. Although the resolution obtained with the analog electronics is $\approx 20 \mu\text{m}$ lower than that obtained with the trapezoidal filter it is not a dramatic reduction. Moreover, using the analog electronics a reasonable resolution could only be obtained for the four central slits as described in the previous section. In contrast, using the digital signal processing approach a relatively uniform resolution is obtained across the entire detector. The somewhat lower value observed for the two edge slits is due to the slight deviation of the distributions from gaussians.

The measured resolution obtained by the joint use of summed risetime along with charge division is depicted by the red circles (gaussian filter) and blue triangles (trapezoidal filter) respectively. Both filters provide a measured resolution of $\approx 90 \mu\text{m}$ across entire detector. This result is a significant improvement over the use of the charge division approach alone. No systematic advantage is observed for one filter as compared to the other filter. Averaging the measured resolution of the central eight slits for either the trapezoidal or gaussian filters, one obtains an average measured resolution of $92 \mu\text{m}$. Accounting for the finite slit width of $100 \mu\text{m}$ this measured resolution corresponds to an intrinsic resolution of $64 \mu\text{m}$. This result is competitive with the resolution obtained using more complex MCP arrangements and a retarding potential [51–53]. The broad variation in risetimes is due to the fixed integration time of the shaping amplifier. The analysis could be improved by using a variable integration time, as determined by the risetime of the RA signals, for the shaping amplifiers. At this time, we opted to focus on constant integration times as it is representative of commercial electronics.

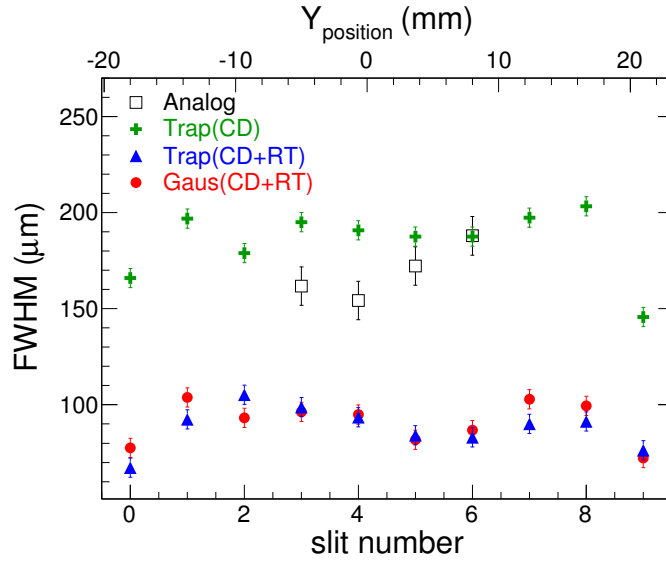


FIGURE 2.40: Comparison of the measured resolution as a function of slit (position) using the correlation between risetime and position with the charge division approach alone. The resolution obtained using analog electronics is shown for reference.

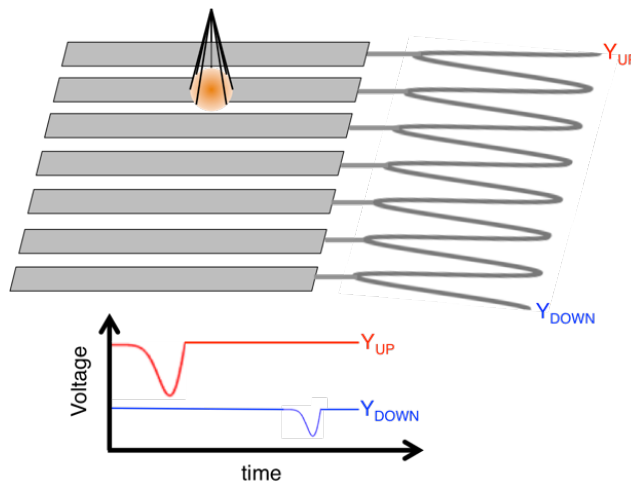


FIGURE 2.41: Schematic illustration of the multi-strip anode with delay line readout.

2.3 The multi-strip anode

Since the RA was found to be unsuitable for characterizing the position dependence of the induced signal shape, we opted to fabricate a multi-strip anode (MA). The issue

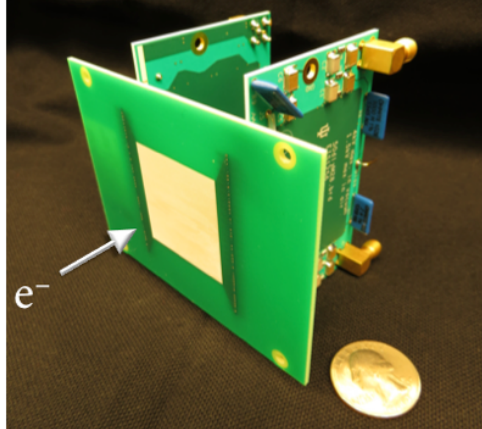


FIGURE 2.42: Photograph of the multi-strip anode with delay line readout in differential mode.

with implementation of the RA was the large capacitive coupling between RA signals and the sense wires position in front of it. Because the MA does not have a large RC, as is the case with the RA, we thought it would be a more suitable detector for characterization studies. The multi-strip anode designed consists of 100 strips, where each anode strip is $250\ \mu\text{m}$ wide with a $75\ \mu\text{m}$ inter-strip isolation. The anode area is approximately $3\text{cm} \times 3\text{cm}$. Upon arrival of the electron cloud, as shown in Fig. 2.41, the signal propagates from the strip(s) to the delay line where it splits. Time difference of signal arrival at either end of delay line is related to signal position. Even and odd strips are independently coupled to the taps of a delay line. Delay boards developed for the MCP-SW v2.0 detector were utilized for this experimental setup, which was both efficient and cost effective. A photograph of the MA can be seen in Fig. 2.42.

The entire assembly presented in Fig. 2.43 is housed in a vacuum chamber that is evacuated to a pressure of 4×10^{-8} torr. To determine the spatial resolution of this detector, a mask was affixed directly to the front MCP bias ring, which is 1 mm away from the MCP entrance. The precision mask, fabricated by laser micro-machining [64], has ten slits each measuring $100\ \mu\text{m}$ by $7620\ \mu\text{m}$ and spaced by either 4.2 or 4.5 mm apart. The entrance of the MCP stack was held at ground, while the MCP exit and MA

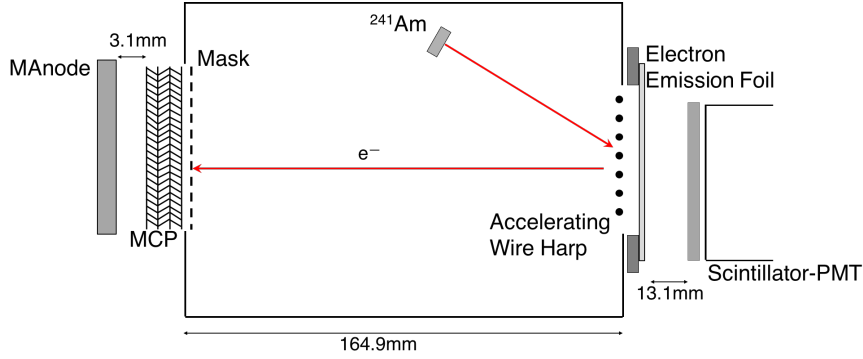


FIGURE 2.43: Schematic illustration of the experimental setup. Indicated in the MCP-MA detector.

were biased to potentials of +2449 V and +2650 V respectively. Both MCP and MA were biased using a ISEG NHQ224M low-noise HVPS. The secondary electron-emission foil and PMT (Burle 8575) were biased to voltages of -300 V and -1800 V using a HK 5900 and Bertan 362 HVPS respectively. The conduit was biased to +1000 V using the HK 6900 HVPS. The signals arriving at either end of the delay line are designated Y_{up} and Y_{down} . Each of these signals was amplified by a low-noise amplifier, the RF Bay LNA-530 (gain = 30, bandwidth = 500 MHz) before being digitized by the CAEN v1729A digitizers, which is a 2 GS/s waveform digitizer with 14 bit resolution and an analog bandwidth of 300 MHz. The signal from the MCP was inverted and amplified by a custom-built, low-noise amplifier (gain = 30, bandwidth = 150 MHz) before being digitized to provide a common time reference for the sense wire signals. The digitizer was triggered using a coincidence between the MCP signal and the PMT signal in order to reduce background events due to radiogenic decays in the MCP. The MCP signal used for the trigger was first inverted with a 100 MHz inverting transformer and subsequently amplified by an custom-built, low-noise amplifier (gain = 30, bandwidth = 150 MHz). Both the MCP and PMT signals were discriminated using a leading-edge discriminator (Phillips Scientific 711) before forming the coincidence. The electronics diagram for this setup is presented in Fig. D.6.

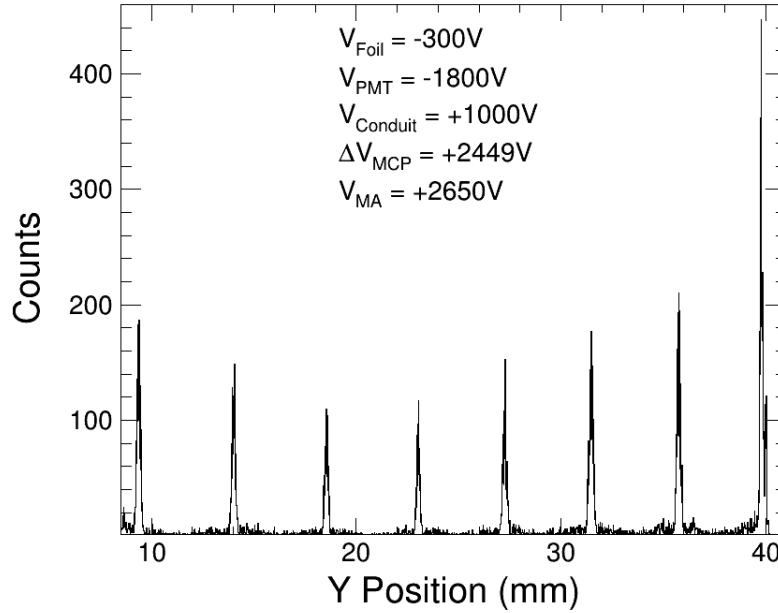


FIGURE 2.44: Position spectrum for the MCP-MA detector.

The digital signal processing included: digitizing the MA waveforms, performing an FFT with a frequency cutoff of 150 MHz, performing a linear interpolation to step in a time steps of 0.05 ns, taking the derivative of the signal, performing an FFT with a cutoff frequency of 500 MHz, and extracting the minimum of the derivative signal. The minimum of the derivative is a sensitive probe sense it represents a maximum value for the rate of change and is designated t_{Yup} and t_{Ydown} .

The time space was calibrated to the position space using the known location of the slits in the mask. After calibration, the relative deviation of the data from the fit, $(\text{data} - \text{fit})/\text{fit}$, is at most 1.4%. Individual slits (from bottom to top) have a deviation of: 1.37, -0.14, -0.23, -0.19, -0.13, -0.19, -0.36, and 0.09 %. The resulting Y-position spectrum is depicted in Fig. 2.44. A total of eight peaks in the position spectrum are clearly resolved, corresponding to the slits in the mask covered by the active area of the MA. The average width of the peaks in the spectrum, calculated using Gaussian Fits, was utilized to determine the spatial resolution. Based on the Gaussian-like nature of the peaks, the average FWHM was calculated using $\text{FWHM} = 2.35 \cdot \sigma$ for the eight peaks.

The spatial resolution after implementation of an FFT was $222 \mu\text{m}$ FWHM. The spatial resolution was further improved by selecting events where the sum of the $(\Delta t_{Y_{down}} + \Delta t_{Y_{up}})$ was a constant within 5 ns because points that lie out of this range correspond to spurious events where the delay-line length is not constant. The pulse width of the Yup signal was used to reject multiple-hits on the detector. The width was determined by finding the time at which the left edge and right of the unipolar signal passed 25%, and subtracting the left edge time from the right edge time. It was determined that widths greater than 12 ns for Yup corresponded to double-hits on the detector, and were consequently rejected.

With the FFT filtering, constant delay condition, and the pile-up rejection a measured spatial resolution of $169 \mu\text{m}$ was achieved with a rejection of 14.2% of the data. Further improvements were made by requiring that the sum of the Yup and Ydown amplitudes be lower than -54 mV. The measured spatial resolution achieved for this processing method with the best gating criteria is $117 \mu\text{m}$ FWHM with a rejection of 54.6% of the data. The intrinsic spatial resolution once the effect of the finite slit width is de-convoluted is $94 \mu\text{m}$ FWHM. The nicety of this approach is that it is a simple alternative to the typical electronics dense drawback of the multi-strip anode approach. The multi-strip anode has achieved $25 \mu\text{m}$ resolution in the MAMA detectors [49] with individual readout of the MA, but this method demonstrates that reasonable resolution can be achieved in a much more cost efficient way.

Chapter 3

Some applications of position-sensitive MCP detectors

3.1 Slow neutron radiography

This chapter concentrates on the development of two applications for PS-MCP detectors, which are slow neutron radiography and radioactive beam imaging. The sense wires approach is utilized for neutron radiography, whereas a multi-strip anode is coupled to an $E \times B$ detector for beam imaging. Experimental details along with the development of a new data acquisition system for neutron radiography are detailed. The spatial resolution achieved for both imaging detectors are discussed.

3.1.1 Motivation

The substantial penetrating power of neutrons allows them to non-destructively probe the internal structure and dynamics of dense media, and to identify materials contained within casings of heavy metals. For example, when the integrity and/or reliability of a stockpiled weapons system is called into question, the conventional approach is to completely disassemble and inspect the system. This approach is costly. Neutron radiography could be used as a means to screen weapons prior to disassembly [73]. As a diagnostic tool neutron radiography also affords the opportunity to impact fundamental studies. The high sensitivity of neutrons to hydrogen enables neutron radiography to greatly advance the understanding of water management in fuel cells [74–76]. This ability to sense light elements (such as hydrogen) in the presence of heavy metals exploits the non-monotonic variation of scattering-length density with position in the periodic table, but there are new developments in the field that can also be exploited.

The last several decades have seen tremendous advances in the sensitivity of various techniques to probe materials. Many of these advances have employed a common strategy, namely, to add a new contrast mechanism upon the foundations of some relatively well-established technique which extends its scientific reach in an efficient manner. Often this contrast agent/mechanism can be implemented as an add-on to an existing device. Optical and surface microscopy provides many such examples: differential interference contrast microscopy, fluorescence contrast microscopy, confocal imaging, two-photon imaging microscopy, scanning probe microscopies (SPM), such as scanning tunneling microscopy (STM), Magnetic Force Microscopy, capacitive SPM, etc. The scientific applications of these various probes are numerous.

We believe that neutron imaging is on the cusp of a comparable transformation. We further believe that some of these could be of particular utility in security applications and that the detector technology that we are developing will have a significant impact in this arena. Researchers in Europe and Japan have recently developed several novel contrast mechanisms and applications for neutron imaging which illustrate the exciting potential and promise to produce a revolution in the types of problems that neutron imaging can address. Among the concepts developed are the use of Bragg edges to measure average strain, texture, and even grain size in polycrystalline samples in a spatially resolved manner [77, 78]. There have even been early attempts to combine such images with vector tomographic reconstruction to develop a 3-dimensional map of these quantities [79]. Reflecting on these developments, as well as earlier studies of imaging using nuclear resonance [80], and a variety of dark-field and phase-sensitive techniques [81–85] should provide a rough idea of the range of exciting new possibilities this field has to offer. A common feature of these phase-sensitive techniques is to develop a modulated-intensity pattern at the detector (e.g. through the Talbot-carpet produced by a pair of neutron-absorbing gratings of suitable pitch and position), and use interactions in the sample to reduce the contrast and/or shift the phase of this pattern. By exploiting contrast

tied to the neutron phase, such techniques can distinguish features that give rise to only negligible differences in conventional intensity-based imaging, but they can also bring out completely new information, such as the imaging of magnetic domains [86]. In the early demonstrations of these techniques, the pattern was probed by scanning a third grating across the pattern since the available detectors had insufficient spatial resolution to reveal the modulation pattern directly. These techniques have also, for the most part, been developed for continuous (typically reactor) sources because the modulation pattern is tied to a particular ratio of the wavelength to the pitch of the gratings. However, using appropriate manipulation of the neutron spin and a detector with sufficient temporal resolution, a time-dependent modulation can be established at the detector, and this pattern can be analyzed at each wavelength in a time-of-flight spectrum for each detector pixel. This provides an avenue for deploying these techniques on pulsed (broadband) sources where time-of-flight can be used to distinguish different neutron wavelengths.

Over the last five years, researchers at LENS have developed a number of devices for manipulating the neutron spin in ways that can be used to realize some of these novel contrast mechanisms [87]. Researchers at LENS have not yet been able to collect suitable images as they do not have access to a detector with adequate temporal and spatial resolution. The plan is to link activities at LENS in support of neutron imaging in the development of position-sensitive, high-speed detectors to make significant strides in pushing the state-of-the-art in neutron imaging. The first step, which is presented in this thesis, is the application of the MCP-SW detector for traditional radiography.

The combination of both high spatial and temporal detector resolution is also important, for instance, in measuring the strain (associated with, say, 100 ppm shifts in the positions of Bragg as shown in [78]) corresponding to changes in time on the order of a few μs , and identifying species through neutron resonances will require similar capability. We also note that there are also other novel neutron techniques that will also be able to

make use of position sensitive detectors with better than 100 μm spatial resolution and/or μs time resolution include Modulated Intensity with Zero Effort, or MIEZE, which is a technique in which resonant spin-echo techniques are used to modulate the neutron beam with 100's of kHz to MHz frequencies to provide measurements of small energy transfer [88]. There is, therefore, a significant need for detectors with these capabilities even beyond the realm of techniques currently being investigated at LENS.

Researchers at LENS have already demonstrated novel concepts in neutron moderation [89, 90] and various devices for manipulating neutron spins [87, 91]. These recently developed spin-manipulation devices provide the basis for various novel contrast mechanisms to be incorporated into thermal neutron imaging. Naturally, polarized neutron imaging can provide important information on magnetic structures, but the neutron spin can also be used to encode neutron momenta and position as well [91] and this can be used to provide contrast based on small-angle scattering [84], or grain size (i.e. structural information on length scales below the technique's resolution limit, say 10 nm to 5 μm). In areas such as additive manufacturing or cumulative radiation damage in materials, imaging with such contrast could provide information unavailable with any other non-destructive technique. At this point, the extent to which images exhibiting this type of contrast will complement or duplicate the information available from Bragg-edge contrast images is unclear, but the detector we will develop here will be invaluable in assessing the relative strengths of the various options for imaging the distribution of detailed microstructure in components.

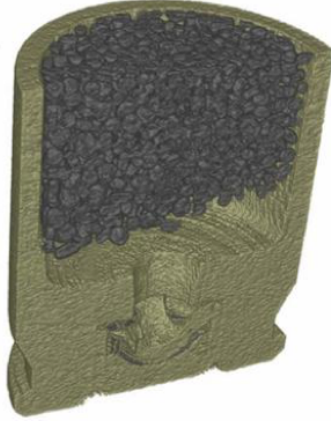


FIGURE 3.1: Individual gunpowder grains in a bullet measured using neutron tomography with the Medipix2 detector [18].

TABLE 3.1: Detection efficiencies for thermal, cold, and ultra-cold neutrons using NeuView detectors as compared to CCD based detectors [92].

* Quantum efficiency is a function of neutron energy and operating conditions.

** Dependent upon neutron beam dispersion and readout selected current best achieved resolution: 36 μm FWHM.

*** All-electronic gamma rejection option (proprietary): gamma sensitivity $<10^{-6}$ (gamma/neutron QDE) while preserving high thermal neutron sensitivity, available late 2017.

| Neutron Wavelength (\AA) | NeuView TM MCP Detector | Scintillator (Li-6) + CCD |
|-------------------------------------|---------------------------------------|------------------------------------------------------------------|
| QE* at 0.9 (thermal/epi) | $\sim 20\%$ | $\sim 5\%$ |
| 1-2 (thermal) | $\sim 40\%$ (static or dynamic) | $\sim 10\%$ (static), $<0.1\%$ (dynamic/gating) |
| 5 (cold) | $\sim 70\%$ | $\sim 25\%$ (static) |
| 30 (very cold) | $\sim 80\%$ | $\sim 30\%$ (static) |
| Spatial Resolution | $\sim 50 \mu\text{m}^{**}$ | $>200 \mu\text{m}$ |
| Temporal Resolution | $\sim 100 \text{ ns}$ | $\sim 100 \text{ ms}$ (ungated), $\sim 1 \mu\text{s}$ (gated) |
| Gamma Ray Sensitivity | $\sim 1\%$ ($<10^{-6***}$) | |

3.1.2 Overview of modern neutron radiography

Since neutrons are neutral particles, they must undergo a conversion into secondary particles to be detected. These particles can be electron-hole pairs for semiconductor detection, photons for neutron-sensitive scintillators, or ions/electrons for Gd or B doped microchannel plates (MCPs). Traditional neutron radiography involves a neutron-sensitive scintillator, such as ${}^6\text{LiF}$, GADOX (gadoliniumoxisulfite), or ZnS:Cu , followed by a CCD camera or amorphous silicon flat panel. As a result, there is an inherent tradeoff between spatial resolution and detection efficiency. The thicker the scintillator the higher the detection efficiency, but with increasing thickness leads to increased light scattering in the grains. For an optimized scintillator-camera assembly, the detection efficiency is typically only 1% [93]. X-Ray films are another commonly employed for neutron radiography due to their low cost. A spatial resolution of 20–50 μm has been achieved with film, but typical exposure times for a suitable image is 5 minutes, which is much longer than the scintillator/CCD exposure time of 10 seconds on the PSI NEUTRA beam line [94]. Film also has several other drawbacks including: a limited dynamic range, a strongly non-linear response, the method cannot be used for neutron tomography, and the risk of sample activation as compared to the scintillator/mirror geometry [94]. Imaging plates are another detection means for neutron radiography, which have achieved 25–100 μm spatial resolution with short collection times of 20 s [94]. Doping MCPs with ${}^{10}\text{B}$ has typically achieved detection inefficiencies of 14–18% for thermal neutrons, with a theoretical upper limit of 50% if one uses a square microchannel geometry and increased ${}^{10}\text{B}$ doping for thermal neutrons [9, 10]. The MCP technology provides a means of achieving high spatial resolution with an improvement to detection efficiency. Table 3.1 lists the detection efficiencies for various neutron energies using both a CCD/scintillator arrangement as compared to a neutron-sensitive MCP detector [92]. The detection efficiencies, as measured by Surface Concept using Nova Boron MCPs, are clearly superior in the

MCP based systems at all energies. Furthermore, the spatial resolution was measured to be far superior at 50 μm FWHM for MCPs as compared to 200 μm for the CCD readout.

Furthermore, due to the absence of efficient neutron focusing optics, a high spatial resolution on the position-sensitive detector is required. Work has already been demonstrated using a ^{10}B doped MCP with a Medipix2/Timepix CMOS detector [45, 54] to image the individual gunpowder grains in a bullet (see Fig. 3.1)[18]. The Medipix2 readout allows neutron imaging at very high count rates (exceeding 100MHz), but is limited by the 55 μm pixel size at this rate [95]. At count rates of 2–3 MHz, the Medipix/-Timepix2 readout can achieve a resolution of 15 μm FWHM [47, 95]. Furthermore, the rate would be limited by the MCP to 10 MHz for this detection scheme. The MCP/XDL detector can operate at rates of ~ 0.5 MHz, and achieve a spatial resolution of ~ 30 μm FWHM [95].

Perhaps the state-of-the-art in slow neutron radiography is the Medipix2/Timepix CMOS readout which can achieve 15–55 μm FWHM resolution, but is fairly expensive and has a small area ($14 \times 14 \text{ mm}^2$). Use of the induced signal approach could provide a cheaper alternative to the Medipix2/Timepix technology (see Fig. 1.5). The low cost of this approach makes the coverage of large areas feasible by using multiple detectors each capable of sustaining a high rate. We do not expect the induced signal approach to achieve as good of a spatial resolution as the Medipix/Timepix sensor at this time, but we stress that this detector is still in the development phase. Furthermore, one major difference between the Medipix2/Timepix detector and the induced signal approach is the use of high speed digitizers for the sense wires as opposed to charge integration circuits. Some of the most exciting advances in electronics is in the realm of high-speed sampling and real-time processing of signals (digital signal processing). We therefore opted to investigate the limit of spatial resolution that can be achieved with high-speed sampling of the induced signals. Even if the induced signal approach cannot achieve the best

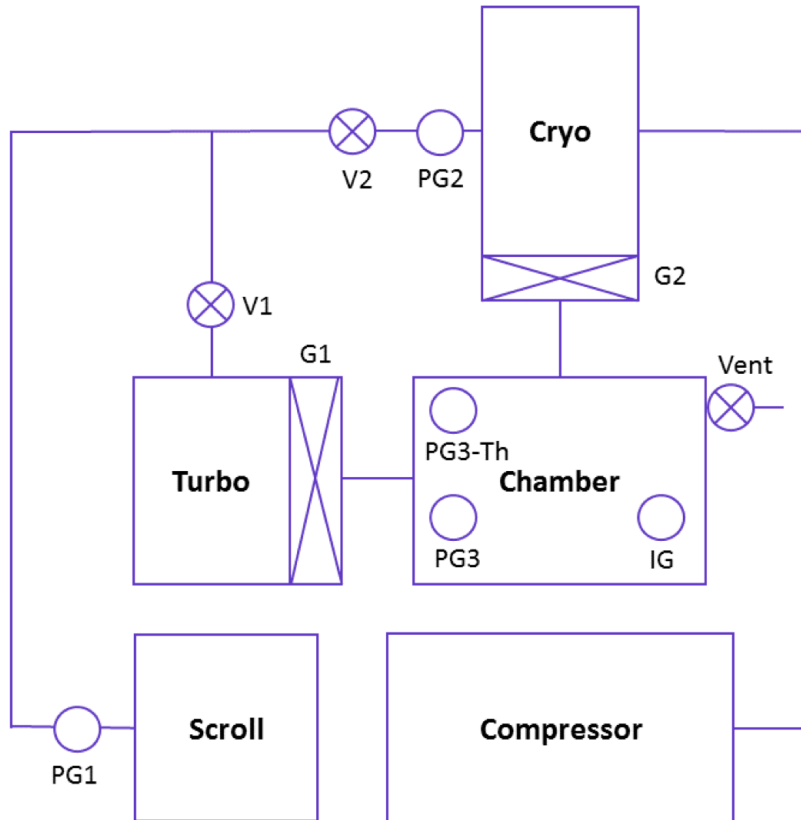


FIGURE 3.2: Schematic drawing of the vacuum test station for radiography. The vacuum is monitored by pressure gauges (PG1, PG2, PG3, and PG3-Th) and a hot-filament ionization gauge (IG). Gas flow is controlled by the manual valves (V1 and V2), gate valves (G1 and G2), and a vent valve (Vent).

spatial resolution as compared to the state-of-the-art measurements, there are still many applications where a somewhat worse resolution is still very useful. This is particularly true if the poorer resolution is offset by the ability to cover larger areas either by a single detector or by tiling. For example, with only 0.8 mm resolution, Kiyonagi and co-workers were able to map the strain associated with an iron plate under a tensile test [78]. Among the concepts developed are the use of Bragg edges to measure average strain, texture, and even grain size in poly crystalline samples in a spatially resolved manner [77, 78].

3.1.3 Radiography vacuum station

Due to the size constraints of working on a neutron beam line, we opted to design and construct a new vacuum test station specifically for this application. This had the added benefit of being able to test two separate sense wire detectors simultaneously. This radiography vacuum station (RVS) is an oil-free based system, which will extend the lifetime of the MCPs. As previously described, the operation of MCPs requires high vacuum with a pressure well below 5×10^{-6} torr. Moreover, due to the hydrophilic nature of the MCP plates, their storage when not in use also requires a good vacuum environment. The RVS is composed of the following major components: ISO200 six-way cross, scroll pump (Edwards nXDS15i 100l240V), turbomolecular pump (Pfeiffer TMH 262), and cryogenic pump (Austin Scientific Cryoplex 8 and Model 125 Compressor). A schematic drawing of the vacuum test station is shown in Fig. 3.2. After its assembly, the RVS was leak checked and found to be leak tight.

The scroll pump is used to establish rough vacuum in the chamber, and to back the turbomolecular pump (turbopump) during its operation. Once the chamber has been roughed out to a pressure of less than approximately 100 mtorr, the turbopump is used to evacuate the chamber to high vacuum. Following evacuation by the turbo pump to a pressure of approximately 2×10^{-5} torr, the cryogenic pump (cryopump) is used and the turbopump is valved off from the chamber. This limited use of the turbopump improves the noise characteristics of the test chamber as well as extends the lifetime of the turbopump. Using the cryopump the RVS can be evacuated to a pressure of 5.0×10^{-7} torr. A lower pressure was not obtained as this station has yet to be pumped continuously for longer than a few weeks. A photograph of the RVS in the neutron beam line can be seen in Fig. 3.3. To monitor the pressure, a combination of Pirani thermal conductivity sensors (HPS Products Series 316 Pressure Sensor) at each pumping stage, an extended-range Pirani thermal conductivity sensor (Thyracont VSR53DL), and one

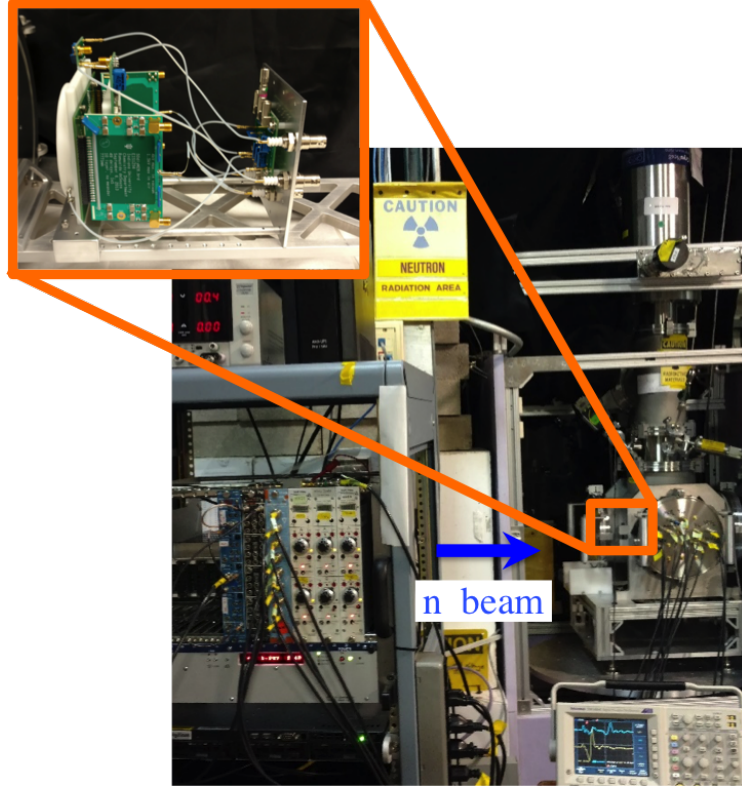


FIGURE 3.3: Photograph of the vacuum test station and MCP-SW detector in the LENS beam line.

hot-filament ionization gauge (HPS Products 10047) in the chamber are used. Moreover, the entrance flange, nominally 0.47 in thick, is thinned down to 0.10 in in the central 2 in diameter region. By thinning the flange in the central region, a calculated transmitted neutron flux of 97.39% should arrive on the detector face where 0.35% were absorbed and 2.26% were scattered.

3.1.4 Experimental setup

Depicted in Fig. 3.4 is the experimental setup used to detect slow neutrons and determine the spatial resolution of the MCP-SW detector. Slow neutrons are generated from the Low Energy Neutron Source (LENS), which is described in more detail in the following section. The detector is placed within the RVS. The entry and exit flanges of

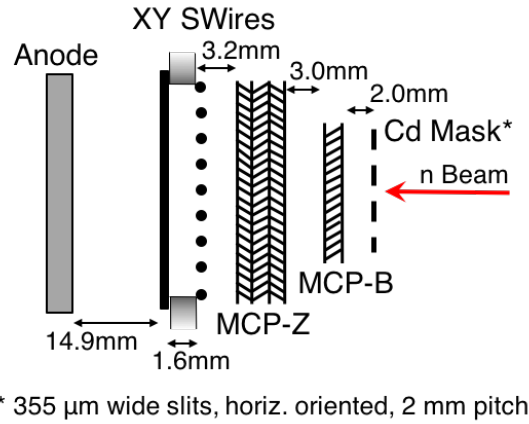


FIGURE 3.4: The experimental setup used for the slow neutron radiography measurements.

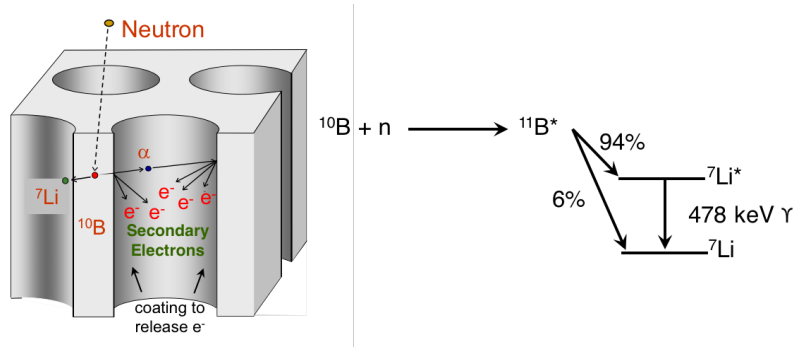


FIGURE 3.5: Neutron capture reaction in a boron doped MCP. Figure is taken from [96].

this station are constructed from aluminum to minimize neutron absorption/scattering. Moreover the entrance flange, nominally 0.47 in thick, is thinner in the central region to be 0.10 in thick. The neutron beam from LENS is incident on the entrance flange of the radiography station. Inside the RVS the neutrons are incident on a cadmium mask placed in front of the detector. Neutrons that pass through slits in the mask generate an electron signal which is amplified by the MCP stack and are subsequently detected by the sense wire harp.

The slow and thermal neutrons in the beam generate the electron signal by first producing charged particles via the net nuclear reaction below:



Capture of the neutrons by ^{10}B atoms doped into an MCP (termed MCP-B), results in production of an α -particle (1.777 MeV) and a ^7Li ion (1.014 MeV). These atoms will go on to create the electron avalanche in the boron-doped MCP followed by amplification in a MCP Z-stack (termed MCP-Z). The position of the neutron capture event is localized to one or two channels because the range of alpha and Li particles in the MCP glass are 3.5 and 2 μm respectively [97]. There is a 93% chance that the ^7Li will be in an excited state and emit a 478 keV γ . The sensitivity of the MCPs to γ photons is minimal, and thus should not lead to extra image blurring. The sole commercial supplier of neutron sensitive MCPs is Nova Scientific [98]. Although they do not typically sell individual neutron sensitive plates only complete neutron sensitive detectors, they have agreed to sell us individual neutron sensitive plates to advance this project. The MCP-B was a standard Nova MCP with 25 mm diameter, 8 μm diameter microchannels, 10 μm center-to-center spacing, l/d ratio of 80:1, and bias angle $0^\circ \pm 16^\circ$. The MCP Z-stack was a standard Photonis MCP (APD 3 40/12/10/12 D 60:1) with 10 μm diameter microchannels [4].

3.1.5 The neutron source

The low energy neutron source (LENS) at Indiana University is a facility that is unique in the United States and has served as a flagship for a new class of neutron sources that have come to be known as Compact Accelerator-driven Neutron Sources (CANS) [89, 99, 100]. This facility has been a center of innovation in neutron instrumentation for the last decade, is a founding member of the international Union of CANS facilities (UCANS), and produces neutron beams with sufficient intensity to conduct materials

research and instrumentation testing. LENS has already been involved with both new technologies related to radiography and the testing of new detector technologies [87, 101].

The small angle neutron scattering (SANS) beam line available has an associated integrated neutron count rates of $2.7\text{--}5 \times 10^4 \text{ n s}^{-1} \text{ cm}^{-2}$. Instantaneous count rates in the moderator imaging station (MIS) beam line can exceed $1 \times 10^5 \text{ n s}^{-1} \text{ cm}^{-2}$ for neutrons near the peak in the moderator spectrum and roughly a factor of 3 higher than this for fast neutrons (during the proton pulse) [101]. If needed, even higher rates could be realized by placing a detector within one of the target vaults (at distances as small as 1.5 m from the moderator), but this would not have the added benefit of collimating the neutron beam. The sample position of the SANS beam line has an associated L/D ratio of ~ 83 . The L/D is an important ratio to consider when choosing a neutron source because it determines the resolution limit of your detector. The equation for the resolution limit, d , is listed below where l is the distance from your sample to the detector, D is the aperture or moderator window size, and L is the source to detector length [102]. For the minimum distance between object and detector possible of $l = 2 \text{ mm}$, given that D was 10 cm, and L was 830 cm a resolution limit of $24 \text{ }\mu\text{m}$ is obtained. This resolution limit is well below the spatial resolution achieved when measuring single electrons.

$$d = l \cdot (D/L) \tag{3.2}$$

The floorplan for LENS is depicted in Fig. 3.6. LENS is composed of a 13 MeV proton linac that was the first university-based pulsed neutron source in the United States, and is based off a similar concept from Chalk River Laboratories [103, 104]. The LENS proton accelerator utilizes a PL-13 Linac to provide a 25 mA (peak current), 13 MeV beam with a 1.8% duty cycle and up to 6 kW of beam power. The proton beam has a variable pulse width ranging from $10 \text{ }\mu\text{s}$ to 1 ms with a repetition rate of 10 to 40 Hz.

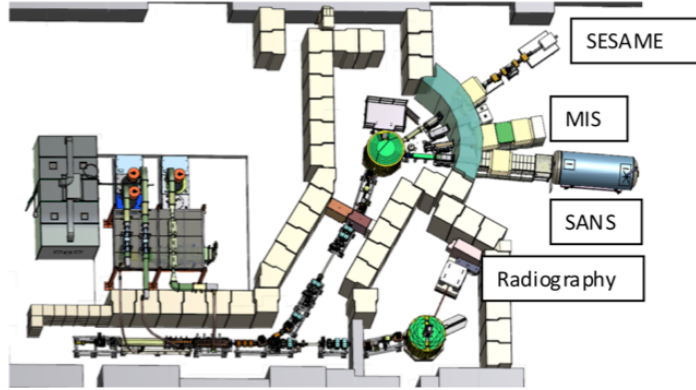


FIGURE 3.6: The 13 MeV accelerator (lower left) is powered by three 1 MW klystrons operating at 425 MHz and feeds a proton beam onto a beryllium target in one of two target stations (green circle on the right).

The PL-13 consists of a 3 MeV RF quadrupole, a 4 MeV drift tube LINAC (DTL), and a 6 MeV DTL to achieve a total energy of 13 MeV. Once the protons have been accelerated to 13 MeV, two octapole magnets (one for X and Y) along with standard quadrupole magnets define a beam spot that is ≈ 3 cm high by ≈ 4 cm wide. This corresponds to a power density of 500 W/cm average, 28 kW/cm instantaneous on the 1.1 mm thick beryllium target.

Neutrons are generated from low energy ${}^9\text{Be}(p,xn)$ reactions in the water cooled beryllium target. This reaction offers a high cross-section for neutron production with a limited gamma production and activation of the source. Note that the main source of γ background is due to capture in the moderator and reflector. More information on the total neutron cross-section as well as energy and angular distributions can be found in [105, 106]. Neutrons are then moderated using a 1 cm thick solid methane moderator held at 6.5 K. There is a beryllium filter placed downstream of the moderator, which selects a higher concentration of slow neutrons as compared to fast neutrons. Collimation using a series of boron nitride and stainless steel rings defines our beam spot to be ≈ 20 mm.

We were situated on the small angle neutron scattering (SANS) beamline at LENS.

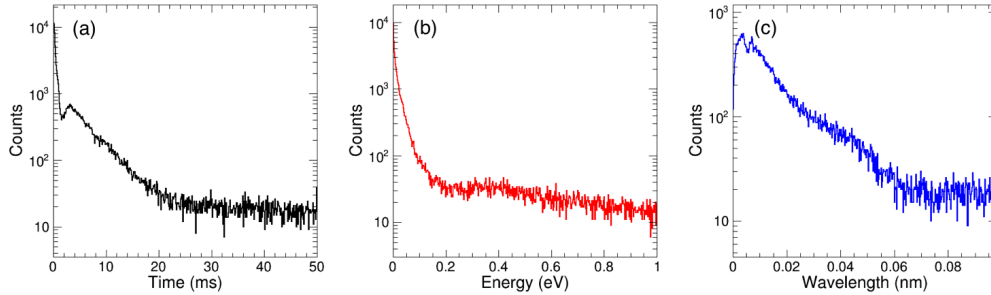


FIGURE 3.7: LENS beam structure with (a) time-of-flight, (b) energy, and (c) wavelength shown.

At this beam position, a compound neutron energy spectrum is observed where one component is a fast flash of neutrons while the other is roughly a 19K Maxwellian. A neutron energy spectrum at our beam position is presented in Fig. 3.7c. This energy was calculated using the time-of-flight (TOF) measurement where the start time is the proton pulse associated with the LINAC and the stop pulse is associated with slow neutrons arriving on our detector.

State-of-the-art neutron radiography is typically performed with the highest fluxes achievable ($10^6 - 10^8 \text{ counts s}^{-1} \text{ cm}^{-2}$) and is typically limited to facilities like the NEUTRA (thermal neutrons) or ICON (cold neutrons) facilities at Paul Scherrer Institut (PSI), the Spallation neutron source at Oak Ridge National Lab (ORNL), the Lujan Center at Los Alamos Neutron Science Center (LANSCE), or the using the reactor at the National Institute of Science and Technology (NIST). A more complete list of the international facilities can be found in [102]. Tremsin and co-workers have already demonstrated that approximately $15 \mu\text{m}$ FWHM can be achieved when individual gun powder grains inside of a bullet shell casing using an Medipix2/Timepix CMOS detector (see section 1.6.4) at the ICON beam facility [18]. To achieve the highest quality image, one would require a high neutron flux so that the radiogenic decays of the MCP do not limit the measurement in terms of background. Moreover, a coherent beam with minimal divergence is crucial to high quality imaging. While making a measurement at one of the

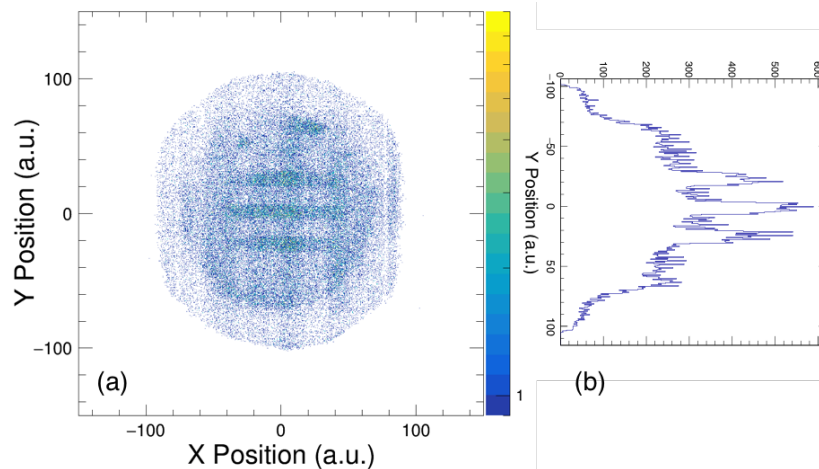


FIGURE 3.8: a) First 2D image with slow neutrons at LENS. b) One-dimensional y-projection of the 2D image.

sources above would be preferable, we have opted to operate at the Low Energy Neutron Source (LENS) at Indiana University for diagnostic purposes. Making a measurement at one of the listed facilities would be a natural advancement of the project.

3.1.6 First neutron radiographs

The following measurements were made over a two day period in December 2016. The availability of the beam time was given on short notice and as a result did not enable adequate experiment preparation time. Nonetheless, this test enabled our first detection of neutrons with our un-optimized experimental setup and DAQ. The mask used in this measurement is mounted on the front flange of the vacuum chamber, which is 27.4 mm upstream from the MCP active area, contrary to the setup shown in Fig. 3.4. The precision mask, fabricated by electrical discharge machining, has 5 slits each measuring 2 mm wide and spaced by 5.0 mm apart. However, only the central 3 slits were illuminated in this case due to the size of our beam spot. If one compares the area of a beam spot to the area of the slits, the area of the detector exposed to neutrons in this measurement was 13.85%.

The entrance of the MCP-B was held at ground, while the MCP-B exit was held at +936 V. The entrance to the MCP-Z and the exit were biased to potentials of +1026 V and +3860 V respectively. The sense wires were biased to potentials of +3885 V and +3900 V. The MCP-B, MCP-Z and SW were biased using a ISEG NHQ224M low-noise, HVPS, while the anode was biased to +4000 V using a ISEG NHQ226L HVPS. The signals arriving at either end of the delay line are designated Y_{up} and Y_{down} for the Y-dimension and X_{Left} and X_{Right} for the X-dimension. Each of these signals was amplified by a custom built low-noise amplifier (gain = 30, bandwidth = 150 MHz) before being digitized by the CAEN v1729A digitizers, which is a 2 GS/s waveform digitizer with 14 bit resolution and an analog bandwidth of 300 MHz. The anode signal was also digitized to provide a common reference time for both v1729A digitizers. The digitizers were triggered using the anode signal after amplification by an RF Bay LNA-530 amplifier (gain = 30dB, bandwidth = 500 MHz). The full electronics diagram is depicted in Fig. D.7.

Using LENS in low power mode ($\sim 10\%$ of full power) we were able to acquire our first 2D neutron image as shown in Fig. 3.8a. The 25 mm outline of the Boron-MCP and the 40 mm outline of the MCP Z-stack are clearly visible. There is a hotspot inherent to the MCP stack at $Y \approx 60$ au and $X \approx 10$ au. Also visible is a sharp cutoff at both the left and right edges of the detector. Non-uniform intensity fluctuations across the face of the detector are also observed. Even with a low S/B of 0.7, we were able to clearly resolve 2 mm wide slits in our Cd mask as is evident in Fig. 3.8b. An intrinsic spatial resolution of 861 μm FWHM was extracted. The major limitation of the setup was the DAQ could only handle a maximum data rate of 300 cps, thus leading to limited statistics in the image. Another limitation of this detector and DAQ is that we did not have a good way to mitigate background events from radiogenic decays in the MCP glass. An inherent advantage of the 1D MCP-SW detector, see Section 2.1.5, was the electronics was triggered by a coincidence measurement between the α -particle and striking the foil and the electron arriving on the face of the detector. In this system however, we only

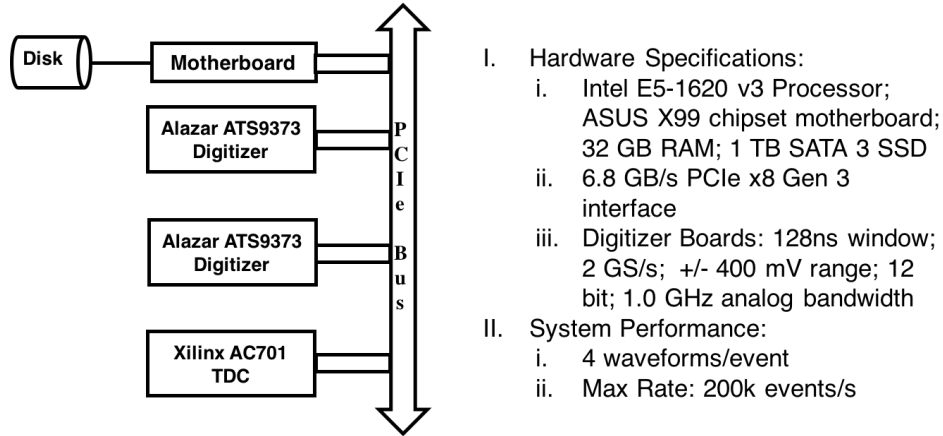


FIGURE 3.9: Data acquisition system developed for slow neutron radiography experiments.

triggered on neutrons arriving on the detector face. In order to reduce background events inherent to the MCP glass, we sought to incorporate a time-of-flight (TOF) measurement where the start time is the proton pulse associated with the LINAC and the stop pulse is associated with slow neutrons arriving on our detector. This TDC was added to the system described in the second neutron measurement conducted in June 2017.

3.1.7 Neutron data acquisition

In order to improve the S/B of the detector and not be limited by poor statistics, we constructed a new DAQ that can acquire data at rates up to 200k cps such that our image quality will not be significantly influenced by the radiogenic decays in the MCP (rate=100 cps) that are the major source of background. The data acquisition system developed for slow neutron radiography is shown in Fig. 3.9. The hardware consists of a ASUS X99 chipset motherboard with an intel E5-1620 v3 processor. The computer has 32 GB of RAM and a 1 TB SATA 3 SSD hard drive. There are four PCIe x16 slots, 1 PCIe x4 slot, and one x1 PCIe slot associated with the DAQ. The graphics card uses one x16 slot, the digitizers use two x16 slots, and the TDC uses one x4 slot. The

DAQ employs a 6.8 GB/s PCIe x8 Gen 3 interface to communicate with the two Alazar ATS9373 waveform digitizers and the Xilinx AC701 TDC. There was a 125 MHz clock associated with the TDC, which thus provided a time resolution of 8 ns. This time resolution is much better than what is needed for selection of slow neutrons. This TDC was developed as it allowed implementation into the DAQ with minimized effort. This TDC was relatively easy to integrate because prior development work had accessed the start and stop times by directly accessing the FPGA core under Linux. The digitizers were chosen based on their sampling of 2 GS/s with 12 bit resolution over a ± 400 mV range. A time window of 128 ns was chosen, which is significantly larger than the total delay length of 60 ns. This shorter time window was significantly shorter than the window in the unoptimized CAEN v1729a digitizers, where the data was recorded for 1024 ns. Minimizing this time window reduces the data transfer from the digitizer which allows operation at higher data rates.

The Alazar digitizers were specifically chosen for their maximum throughput being determined by the PCIe interface as opposed to the previously used VME interface. The event files are structured as follows for each event: the event delimiter (*delim*), number of digitizer channels being read out (*nchan*), the number of samples in the waveform (*nsamp*), the TDC stop time (*tstop*), and the digitizer waveform data. The digitizer waveforms are organized from channel 0 to *nchan* with no delimiters between channels. We can calculate the data generated per event using the following formula:

$$data/event = delim + nchan + nsamp + tstop + (nchanval * nsampval) \quad (3.3)$$

$$data/event = 2B + 2B + 2B + 4B + (4 * 256 * 2B) \quad (3.4)$$

$$data/event = 2058B/event \quad (3.5)$$

We can then calculate the max trigger rate by taking the data storage rate and dividing

by the data generated per event. The bottleneck for recording data is in the SATA 3 SSD, which has a maximum write performance of 600 MB/s. Although this value is often quoted as the write performance, a more realistic value often achieved is 500 MB/s. Writing at this rate would correspond to a max trigger rate of 243k cps. This is approximately a thousand-fold improvement improved over our rate-limited VME system that could record waveforms at ~ 300 cps. We next turned our attention to whether the 1 TB storage would be sufficient. One of the highest intensities we can achieve at the IU neutron source (LENS) is 3000 cps with a 2 mm slit mask at full power. To collect $\sim 10^7$ events, we would require an hour of acquisition time, corresponding to ~ 21 GB data. Furthermore, every 15 minutes a run is automatically ended and the data is transferred from our DAQ to our data drives. Operating at the count rates achievable at LENS does not pose a problem for this DAQ. A flow chart outlining how the DAQ operates while acquiring data is shown in Fig. 3.10.

In order to verify the performance of the neutron DAQ, several pulser tests were performed. One such test involved pulsing both the digitizers and TDC to determine the maximum rates the DAQ could achieve. In this synchronous pulsing mode we were able to record data while, pulsing at ~ 200 kHz. This result is consistent with the previously calculated max trigger rate of 243 kHz. We also measured the maximum throughput the DAQ could handle without recording data to disk. This was determined to be 1.1 MHz, which represents an upper limit for the system. To further improve the count rate the DAQ can achieve with recording to disk we could (a) investigate using digitizers that allow direct access to the FPGA, (b) decrease the record length of the waveforms, (c) use zero-suppression to only record data around the induced signals, or (d) use a hard drives that connect to the PCIe bus directly. Once the DAQ is able to digitize in the MHz regime, no added benefits come from being able to digitize faster; for, MCPs are limited to a maximum rate in the MHz regime.

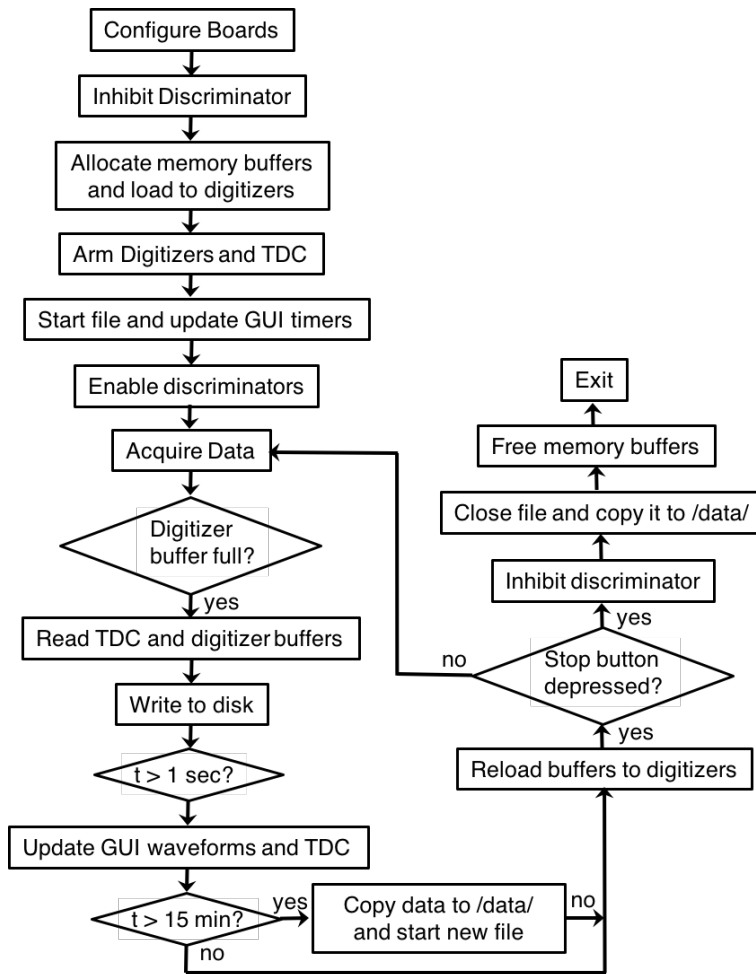


FIGURE 3.10: Flowchart explaining the operation of the DAQ.

The next test performed tested whether readout properly maintained the synchronicity of the digitizers and the TDC. To accomplish this, a pulser that provided two distinct waveforms was used. The first waveform arrived $100 \mu\text{s}$ following the start pulse with double the amplitude as compared to the second waveform that arrived at $200 \mu\text{s}$. The full electronics can be found in Fig. D.8. By having a unique amplitude and arrival time, we were able to determine if the TDC was synchronized with the digitizer boards. At a count rate of 2k cps the digitizer boards remained synchronized with the TDC for a 20 hour stress test. It was also determined that one digitizer can re-arm faster than the other digitizer. This was determined by using the 2D MCP-SW detector to

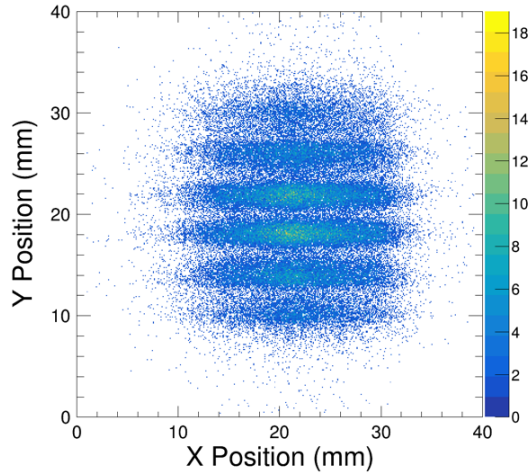


FIGURE 3.11: 2D image acquired using the neutron data acquisition system. An uncollimated ^{241}Am α -source was placed directly in front of masked 2D MCP-SW detector to achieve a count rate of 8000 cps.

acquire data. Both the y-dimension and x-dimension have two signals from each end of the delay line. By sending a signal from each dimension to each of the digitizers, we were able to check the expected anti-correlation (see Fig. 2.7) for each dimension. If the anti-correlation was not present, then we knew the digitizers had lost synchronization. From this test it was determined that to maintain synchronization of the trigger a veto was necessary to inhibit subsequent events for at least two clock cycles (256 ns). Throughout these measurements a veto for 400 ns was provided.

To further test the response of the new data acquisition system, an uncollimated ^{241}Am α -source was placed directly in front of masked 2D MCP-SW detector. With this setup we were able to achieve a count rate of 8000 cps for a $10\ \mu\text{Ci}$ α -source. This confirmed the “robustness” of the DAQ with a higher asynchronous count rate than LENS is capable of providing. The 2D image from this uncollimated alpha particle run is shown in Fig. 3.11. The mask used in this case had a 3.5 mm width, such that most of the active area was exposed.



FIGURE 3.12: Microscope image of Cd mask with 1 mm scale used in Section 3.1.8. The image is a composite of three microscopy images.

3.1.8 Second measurements of neutron radiographs

The Cd mask is mounted directly in front of the entrance MCP bias ring, which is 2 mm upstream from the MCP active area. The mask was placed as close as possible to the MCP to mitigate the influence of beam divergence on spatial resolution. The precision mask, fabricated by electrical discharge machining, has 7 slits each measuring $\sim 355 \mu\text{m}$ wide and spaced by 2.0 mm apart. Due to the imprecision of the machining process brought about by machining at the minimum wire width, the slit width was measured using the IU Light Imaging Microscopy Center. A Leica M205FA Stereo Microscope was used to measure the slit width with the following widths listed from the bottom of the detector to the top: 293, 362, 414, 431, 345, 310, 362 μm . The largest difference in slit

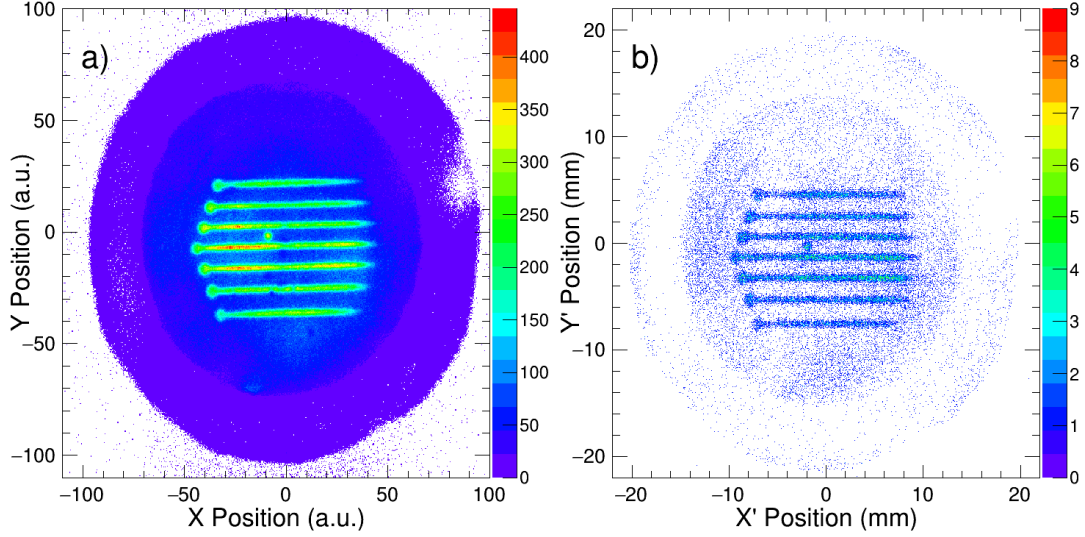


FIGURE 3.13: 2D image acquired using the neutron data acquisition system. A beam of neutrons were produced and moderated using LENS. a) Raw 2D image b) 2D image has been rotated and “cleaned” using several selection criteria.

width is $138\ \mu\text{m}$, so it was crucial that the width was measured in order to decouple the intrinsic spatial resolution from the finite slit width. A composite image of the three microscopy images used to measure the width of each slit is depicted in Fig. 3.12.

The entrance of the MCP-B was held at ground, while the MCP-B exit was held at $+1242\ \text{V}$. The entrance to the MCP-Z and the exit were biased to potentials of $+1373\ \text{V}$ and $+3900\ \text{V}$ respectively. The sense wires were biased to potentials of $+3915\ \text{V}$ and $+3930\ \text{V}$. The MCP-B, MCP-Z and SW were biased using a ISEG NHQ224M low-noise, HVPS. The anode was biased to $+4030\ \text{V}$ using a ISEG NHQ226L HVPS. The signals arriving at either end of the delay line are designated Y_{up} and Y_{down} for the Y-dimension and X_{Left} and X_{Right} for the X-dimension. Each of these signals was amplified by a custom built low-noise amplifier (gain = 30, bandwidth = 150 MHz) before being digitized by the Alazar ATS9373 digitizers, which is a 2 GS/s waveform digitizer with 12 bit resolution and an analog bandwidth of 2 GHz. The digitizers were triggered using the anode signal after amplification by an RF Bay LNA-530 amplifier (gain = 30dB, bandwidth = 500 MHz). The anode signal was amplified by an RF Bay LNA-530 Amplifier before being

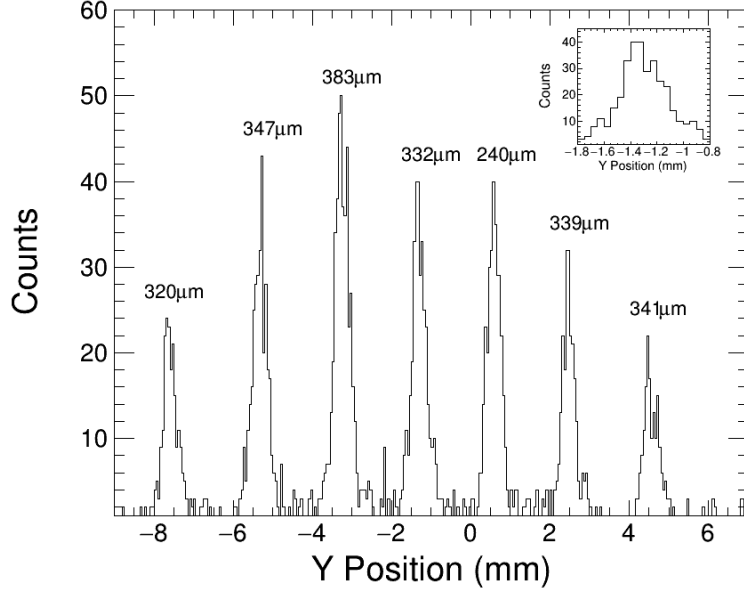


FIGURE 3.14: One-dimensional position spectrum resulting from illuminating the masked MCP detector with slow neutrons.

used to form the trigger and providing the stop signal of the Xilinx AC701 TDC. The start pulse of the TDC was associated with the proton pulse from the LINAC. The full electronics diagram is depicted in Fig. D.9.

After digitizing each induced signal, each signal is filtered with a FFT with a cutoff frequency of 150 MHz. Initially, the zero-crossing point of the digitized, induced signal was utilized to determine the position, but it was subsequently realized that selecting the time associated with 50% of the positive lobe amplitude was superior to the zero-crossing point as it was less susceptible to noise induced from the MCP or anode. The two-dimensional correlation between t_{Yup} and t_{Ydown} is constructed and rotated to the $(t_{Ydown} + t_{Yup})$ vs. $(t_{Ydown} - t_{Yup})$ reference frame. The quantity $(t_{Ydown} - t_{Yup})$ reveals the image of the slits in the mask and is designated Y position in arbitrary units. The quantity $(t_{Xleft} - t_{Xright})$ is constructed in the same way and referred to as X position in arbitrary units. A image without selection criteria, but after FFT filtering is shown in Fig. 3.13a, and is designated a “raw” 2D image.

The seven slits are all clearly visible in Fig. 3.13a. The 1 mm starting hole (for the machining process) at the edge of each slit is also evident. The 0.5 mm keyhole (for determination of left, right, up, and down) between the fourth and fifth slit (counting from the bottom slit) is also clearly evident. One can also see the circular active area of the MCP-B (25 mm diameter) and the MCP-Z (40 mm diameter). There is a bald spot in the northeast section of the 2D, which we opted not to investigate at this time, since the MCP-B represents the neutron sensitive region of the detector. There is an intensity profile apparent on the slits that we attribute to an intensity profile in the beam spot. Alternatively, it is possible that this intensity profile is a characteristic of the B-doped MCP.

The image was calibrated using the known center-to-center spacing and length of the slits. To calibrate the image a first degree polynomial with a slope of 0.212 mm/au was used. After calibration, the relative deviation of the data from the fit, $(\text{data} - \text{fit})/\text{fit}$, determined to be at most 1.61%. Individual slits (from bottom to top) and the 0.5 mm hole have a deviation of: 1.61, -0.04, -0.60, -0.39, -0.28, 0.07, 0.46, and 0.19%. The spatial resolution in FWHM was determined by performing a Gaussian fit on each slit of the Y-projection with an X-position constraint of $-6 \leq x \leq -4.5$ mm. The X-position was chosen to focus in an area where the slit width was constant. The average width of the peaks in FWHM was utilized to determine the spatial resolution. The average, spatial resolution of the raw Y-position spectrum was 676 μm . An improvement was made by applying an FFT filter with a cutoff frequency of 150 MHz, chosen to eliminate high frequency noise. This filtering improved the resolution to 627 μm . Close examination of Fig. 3.13a reveals that the slit images are not horizontal due to the imprecise placement of the mask in front of the detector. To address this issue the two-dimensional image was rotated by an angle so as to make the two dimensions independent of each other. This rotated two-dimensional image (X', Y') was used in the subsequent analysis. The spatial resolution was improved to 607 μm with use of the rotated frame. This resolution was

further improved by selecting on events where the sum of each end of the delay line is a constant value ± 10 ns. Points that lie outside of this range correspond to spurious events where the delay length is not constant. With this requirement the spatial resolution was improved to $595 \mu\text{m}$ with a 8% rejection of the events.

TABLE 3.2: Spatial resolution achieved for different stages in the analysis along with the intrinsic resolution.

| Condition | FWHM (μm) | % Reject |
|------------------------------------------|------------------------|----------|
| 1. Raw | 676 | 0 |
| 2. FFT | 627 | 0 |
| 3. FFT+Rotation (Rot) | 607 | 0 |
| 4. FFT+Rot+ Σ Delay (Σ D) | 595 | 8 |
| 5. FFT+Rot+ Σ D+NTOF | 535 | 93 |
| 6. FFT+ Σ D+NTOF+Thr>6mV | 329 | 99 |
| Intrinsic of Condition 6 | 216 | 99 |

Selection of slow neutrons using the measured time-of-flight (TOF) as shown in Fig. 3.7, improved the spatial resolution to $535 \mu\text{m}$ with a rejection of 93% of the data. A selection on the TOF spectrum was made until $2 \leq \text{TOF} \leq 12$ ms utilized. An additional selection criteria of an amplitude requirement was imposed. Examination of the pulse-height distribution for the positive lobe of the X_{Left} induced signal is determined to have a mean of 6.03 mV and a width of 2.57 mV ($\sigma_{\text{statistical}}$). Note this one pulse height distribution is representative for all induced sense wire signals. Based on this distribution, a minimum amplitude of 6 mV for the positive lobe was required in order to eliminate signals with a poor S/N ratio where extraction of timing from the signal was imprecise. The combination of all the selection criteria will be referred to as the “clean” condition. The resulting 2D image for the “clean” condition is shown in Fig. 3.13b. The width of the resulting peaks was determined using Gaussian fits of the Y’ projection as shown in Fig. 3.14. The measured FWHM of each slit listed from top to bottom were: 320, 347, 383, 332, 240, 339, 341 μm . The measured spatial resolution thus has an average value of $328 \mu\text{m}$ with a standard deviation of $41 \mu\text{m}$. To extract the intrinsic resolution from

the measured spatial resolution, the effect of the finite slit width was de-convoluted. The resulting intrinsic FWHM of each slit listed from top to bottom were: 250, 245, 260, 157, 90, 266, 242 μm . The average intrinsic spatial FWHM is thus 216 μm . Table 3.2 summarizes the spatial resolution achieved at each step in the analysis.

This resolution is 1.3 times higher than the best resolution achieved in Section 2.1.5.3 for 2 GS/s digitization. The poorer resolution could be a result of the un-optimized collimation of the LENS beam. It would be a natural evolution of the project to use this detector at a state-of-the-art radiography facility such as Paul Scherrer Institut (PSI) or Los Alamos Neutron Science Center (LANSCE). It was observed that the induced signal amplitude was smaller and consequently the S/N was worse than in the case of the α -particles described in Section 2.1.5.3. This difference in signal amplitude could be due to a greater penetration into the MCP of the neutron as compared to the electron. Larger penetration before conversion of the neutron to an electron signal would lead to an overall decrease in the gain of the MCP detector. Potentially a thicker layer of B at the front of the stack could improve the overall S/N of the signals, and thus improve the quality of the data. Another logical evolution of the setup would be to develop a setup with 10 GS/s for four channels, since our best spatial resolution of 98 μm required this sampling frequency. Rapid progress is being made in the realm of high speed digitization. As a result, we are following development both at commercial vendors in particular SP Devices, as well as national laboratories such as PSI. Specifically, the ADQ7 digitizer from SP Devices and DRS5 chip from PSI are particularly appealing options as they offer 10 GS/s digitization. The ADQ7 chip is particularly interesting as it offers the user to access the FPGA and implement their own digital signal processing routines on it. This FPGA access would allow extraction of the zero-crossing point in real time. The benefit of realizing the position determination in real time is that it minimizes the data transfer allowing higher data rates to be achieved.

3.2 Beam Imaging using a position-sensitive $\mathbf{E}\times\mathbf{B}$ detector

3.2.1 Motivation

A new generation of radioactive beam facilities provide unique opportunities to investigate nuclei far from β -stability. However, the beam intensity of the most N/Z exotic nuclei is typically less than 1000 ions/s posing significant challenges in imaging these beams. In the case of low energy beams, it is particularly important that the imaging detector introduce the least amount of material into the beam path in order to minimally distort the beam. In addition, as most accelerator facilities are pulsed it is beneficial if the imaging detector has good timing characteristics. Due to their high gain, fast temporal response, sensitivity to a single electron, and compact size, microchannel plates (MCPs) are often used as an electron amplifier for these imaging detectors [7].

There are several methods for providing position sensitivity with an MCP detector as discussed in Section 1.6. To realize a beam imaging detector from this technology requires transport of electrons produced at a secondary-emission foil onto the surface of the PS-MCP detector situated away from the beam axis. In one approach, a clever magnetic field arrangement provided transport of the electrons on helical trajectories onto the the surface of a MCP detector [20, 107, 108]. This technique resulted in a spatial resolution of $588\mu\text{m}$ FWHM [107]. The most serious limitation of this approach is the large space occupied by this detector making its use prohibitive in many experiments.

A beam timing detector, which is compact and introduces a minimal amount of material into the beam path, is an $\mathbf{E}\times\mathbf{B}$ detector [109–112]. Such a detector has been used to measure the time-of-flight of beam particles and reaction products in nuclear reaction studies [113–115]. To make the MCP in an $\mathbf{E}\times\mathbf{B}$ detector position-sensitive we employed a multi-strip anode with delay line readout, which is a particularly appealing because of its simplicity and low cost. Moreover, due to the fast time response of the

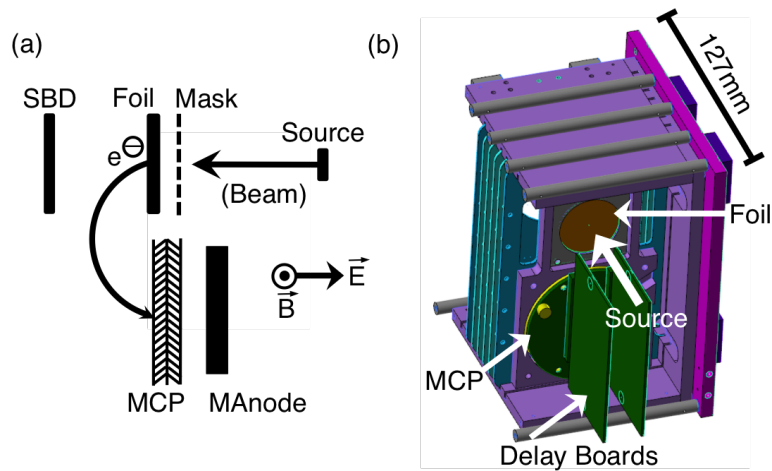


FIGURE 3.15: (a) Schematic of the experimental setup used to assess the spatial resolution of an $E \times B$ MCP detector with a multi-strip anode. (b) CAD drawing of the position-sensitive 40 mm diameter $E \times B$ MCP detector. For clarity, some of the magnets along with one iron plate and the side of the PEEK box have been removed.

detector it is capable of resolving two particles that arrive simultaneously but are spatially separated. Two principal factors influence one's ability to accurately image the beam: the impact of electron transport from the electron-emission foil to the MCP and the inherent spatial resolution of the position-sensitive element. A beam imaging detector was developed by coupling a multi-strip anode with delay line readout to an $E \times B$ -MCP detector. This detector is capable of measuring the incident position of the beam particles in one-dimension. The design, testing, and performance of this detector are subsequently described.

3.2.2 Experimental setup

Presented in Fig. 3.15a is a schematic drawing of the experimental setup used to determine the spatial resolution of the position-sensitive $E \times B$ MCP detector. Electrons, ejected from the $0.5\mu\text{m}$ thick aluminized mylar foil by the passage of ionizing radiation, are accelerated and bent onto the surface of a 40 mm diameter MCP. The MCP used

was a standard chevron stack (APD 2 MA 40/12/10/12 60:1 NR) with 10 μm diameter microchannels provided by Photonis USA [4]. The MCP amplifies the incident electrons by a factor of $\sim 10^6$. The resulting electron pulse is incident on a multi-strip anode. Printed on an FR4 PCB, the multi-strip anode is composed of 250 μm wide strips with a 75 μm inter-strip isolation. The total active area of the anode is $\sim 3\text{cm} \times 3\text{cm}$ (w x h), thus restricting detection of the electrons amplified by the MCP. This choice of a reduced size anode was simply due to ease of implementation in an existing setup. It served the purpose of demonstrating the feasibility of the technique. All 100 strips of the anode are read out by two independent delay boards (as indicated in Fig. 3.15b) to read out the even and odd strips. The use of two delay boards minimizes the attenuation and dispersion experienced by the signal in the delay line. The delay boards consist of a continuous 7771 mm long trace on a 10 layer Rogers 4350 PCB with $\sim 1\text{ns}/\text{tap}$. Construction of the delay line with a high quality PCB material is essential to minimize signal degradation. The position of the incident particle is measured by constructing the time difference of the signal arrival at each end of the delay line. As described in Section 2.3, we previously used a multi-strip anode coupled to a delay line with a simple electrostatic arrangement to achieve a spatial resolution of 94 μm FWHM. Any variation in the electron transport can only adversely impact this resolution. This delay line approach has been successfully employed at rates up to 10MHz [14].

A CAD drawing of the detector is presented in Fig. 3.15b. The electric field is produced using a series of rings situated co-axially along the beam path. By applying a voltage of +4500V to the most upstream ring plate (with $\sim 8\text{mm}$ between ring plates) and stepping the voltage down using 500M Ω resistors between each ring an electric field of $\sim 114,300\text{ V/m}$ is generated. A magnetic field perpendicular to the beam axis is produced by a set of 8 neodymium permanent magnets [116]. The magnets each measure 25mm x 25mm x 12mm and are located on two soft iron plates measuring 146mm x 127mm x 98mm, and collectively produce a field of $\sim 90\text{G}$ in the region of electron production.

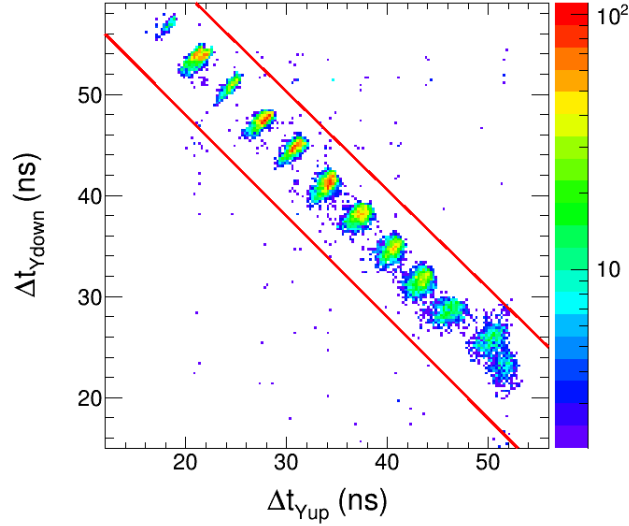


FIGURE 3.16: Two-dimensional spectrum of Δt_{Ydown} *vs.* Δt_{Yup} .

This magnetic field bends the path of the electrons $\sim 180^\circ$ onto the front face of the MCP. The impact energy of the electron on the MCP is controlled by biasing the aluminized mylar foil to -1250V. The biases of the foil and the ring plates were chosen to optimize the measured resolution. The front of the chevron MCP was held at ground, while the back of the chevron MCP was biased to +1792V. The multi-strip anode, spaced from the back of the MCP by 1 mm, was biased to +2350V.

3.2.3 Measuring the spatial resolution of the $\mathbf{E} \times \mathbf{B}$ MCP detector

To test the performance of the detector, it was placed in a vacuum chamber that was evacuated to a pressure of $\sim 4 \times 10^{-7}$ torr. The secondary emission foil of the detector was illuminated by a $1.5 \mu\text{Ci } ^{241}\text{Am}$ α -source. Between the α -source and the secondary-emission foil was a 0.8mm thick aluminum plate with $355 \mu\text{m}$ wide slits that are 6.4 mm long. The 13 slits in the mask have a center-to-center spacing of 2mm. Alpha-particles passing through slits in the mask and in the secondary emission foil were detected using a silicon surface barrier detector (SBD) situated as indicated in Fig. 3.15a.

Passage of an α -particle through the foil generates electrons, which are transported by the $E \times B$ field onto the MCP. The amplified electron signal from the MCP is incident on the multi-strip anode. A signal arriving on a strip propagates to the delay line, where it splits. The signals arriving at either end of the delay line are designated Y_{up} and Y_{down} , and are used to determine the position of the incident particle. Each of these signals was amplified by a fast-timing preamplifier with a gain of 200 (Ortec VT120A) before being digitized by a 10 GS/s waveform digitizer with 8 bit resolution (Tektronix DPO5204 oscilloscope). The digitizer was triggered using a coincidence between the MCP signal and the SBD signal in order to reduce background events due to radiogenic decays in the MCP. The MCP signal used for the trigger was first inverted with a 100 MHz inverting transformer and subsequently amplified by an Ortec VT120A. The SBD (Ortec BA-45-900-100) was amplified by a fast preamplifier [117]. Both the MCP and SBD signals were discriminated using a constant-fraction discriminator (Tennelec TC454) before forming the coincidence. The full electronics diagram is presented in Fig. D.10.

The arrival time of the Y_{up} and Y_{down} signals is determined by utilizing a software CFD, with a fraction of 0.5. A delay time of 1.5 ns was chosen for the CFD based on the typical 3 ns risetime of the signals. The time difference between the trigger time and the zero-crossing point of the CFD for the delay-line signals are designated $\Delta t_{Y_{up}}$ and $\Delta t_{Y_{down}}$.

The two-dimensional correlation between $\Delta t_{Y_{up}}$ and $\Delta t_{Y_{down}}$ is shown in Fig. 3.16. The majority of the data in Fig. 3.16 lies in a single anti-correlated band, with $\Delta t_{Y_{up}}$ increasing as $\Delta t_{Y_{down}}$ decreases. The behavior is approximately linear indicating that dispersion and attenuation in the delay line do not play a significant role in distorting the time correlation. The anti-correlation results from the constant length of the delay line. Points that lie off this line are consequently spurious and can be rejected. One can clearly resolve twelve peaks in the spectrum which correspond to the slits in the mask.

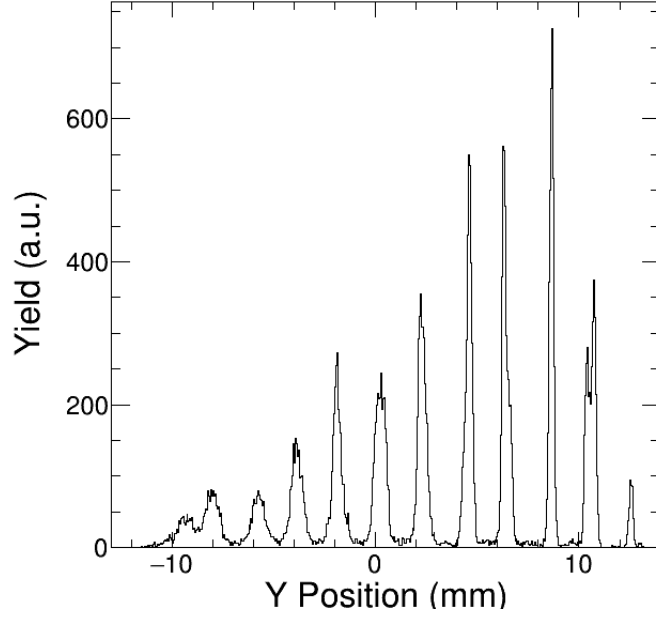


FIGURE 3.17: One-dimensional position spectrum of electrons on the MCP generated by α particles incident on the foil that have passed through the calibration mask. Slits in the mask, with a width of $355 \mu\text{m}$, have a 2mm center-to-center spacing.

From the two-dimensional spectrum evident in Fig. 3.16, a one-dimensional spectrum, $\Delta t_{Y_{down}} - \Delta t_{Y_{up}}$, is constructed. This spectrum is calibrated using the 2 mm center-to-center spacing of the slits and the result is depicted in Fig. 3.17. The average width of the central 7 peaks in the spectrum, $\langle \sigma_{statistical} \rangle$, was utilized to determine the spatial resolution. Based on the Gaussian-like nature of the peaks, the average FWHM was calculated using $\text{FWHM} = 2.35 * \sigma$. Using this approach the spatial resolution of the detector was determined to be $520 \mu\text{m}$ FWHM. An improvement was made by applying a Fast Fourier Transform (FFT) filter with a cutoff frequency of 150 MHz. This improved the spatial resolution to $488 \mu\text{m}$ FWHM. The spatial resolution was further improved by selecting events with $70 \text{ ns} < (\Delta t_{Y_{down}} + \Delta t_{Y_{up}}) < 80 \text{ ns}$ as indicated by the solid lines in Fig. 3.16. With this requirement the spatial resolution improved somewhat to $482 \mu\text{m}$ with a rejection of 8% of the events. Further requirement that the amplitude of the delay line signals exceeded -50 mV resulted in the best resolution obtained. Collectively these

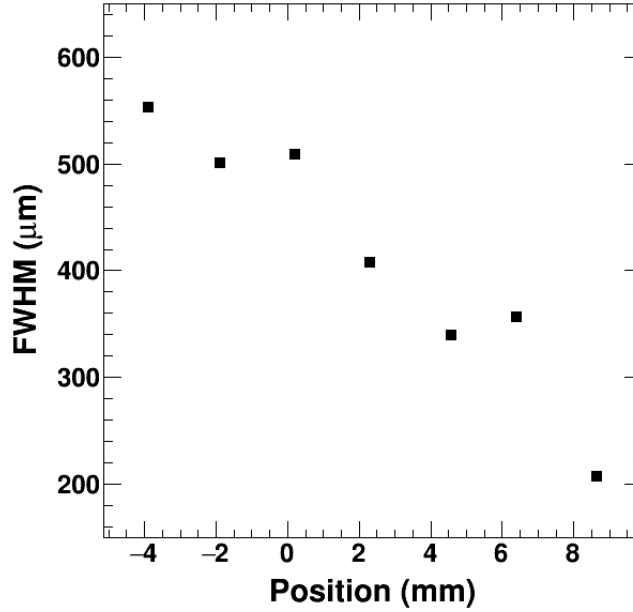


FIGURE 3.18: Measured spatial resolution as a function of position for events meeting selection criteria of the the “clean condition”.

selection criteria are referred to as the “clean condition” and resulted in a resolution of $413 \mu\text{m}$ FWHM. Imposing this condition resulted in a rejection of 66% of the total events.

The dependence of the measured resolution on position is presented in Fig. 3.18 for signals which meet the selection criteria of the “clean condition”. A clear general trend is evident with the resolution decreasing from approximately $550 \mu\text{m}$ to approximately $200 \mu\text{m}$ over a distance of approximately 12 mm. The poorer resolution is associated with the location on the MCP furthest from the foil. This trend was qualitatively discernible in Fig. 3.17 with narrower peaks observed as Y increases from 10 mm to 10 mm. Relaxing the amplitude requirement results in the same overall trend with a slightly larger resolution from 697 to $249 \mu\text{m}$.

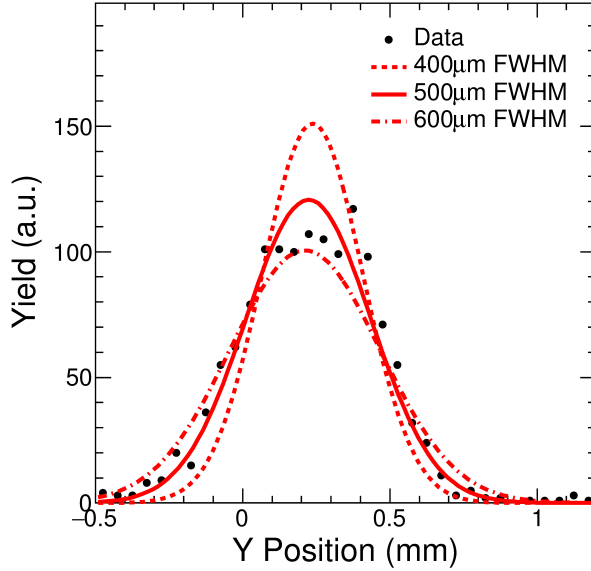


FIGURE 3.19: Measured one-dimensional position spectrum for a central slit (mean $Y = 0.2\text{mm}$) in the mask. Gaussians with widths of $400\mu\text{m}$, $500\mu\text{m}$, and $600\mu\text{m}$ FWHM are depicted for reference.

TABLE 3.3: Spatial resolution achieved for different stages in the analysis along with the intrinsic resolution. The values shown represent the average over the central seven slits.

| Condition | FWHM (μm) | % Rejected |
|----------------------------------------------------------|------------------------|------------|
| Raw | 520 | 0 |
| FFT | 488 | 0 |
| FFT + ΣDelay | 482 | 92 |
| FFT + ΣDelay + $>50\text{mV}$ | 413 | 34 |
| Intrinsic (FFT + ΣDelay + $>50\text{mV}$) | 334 | 34 |

3.2.4 Intrinsic spatial resolution of $\mathbf{E}\times\mathbf{B}$ MCP detector

The spatial resolution measured corresponds to the convolution of the intrinsic spatial resolution of the detector with the finite slit width of $355\mu\text{m}$. The position resolution measured corresponds to the convolution of the intrinsic position resolution with the finite slit width as described in Section 2.1.5.2. In Fig. 3.19, superimposed on the experimental data are the predicted resolutions, $M(Y')$, of $400\mu\text{m}$, $500\mu\text{m}$, and $600\mu\text{m}$ FWHM. From this comparison, one can clearly deduce that the measured spatial

resolution for this slit is consistent with approximately $500 \mu\text{m}$ FWHM. To extract an average intrinsic resolution, the effect of the finite slit width was de-convoluted from the measured resolution for each of the central 7 peaks. The extracted intrinsic resolution of each of the individual peaks was then averaged. Using this approach an average intrinsic resolution of $334\mu\text{m}$ FWHM was determined. The measured resolutions for the different selection and analysis criteria along with the intrinsic resolution are summarized in Table 3.3.

3.2.5 Approved experiments using the $E \times B$ MCP detector

Two institutions, the University of Notre Dame and Michigan State University, have already adopted the use of this $E \times B$ MCP detector for experiments that require a beam imaging detector with decent spatial resolution. The Notre Dame PS-MCP detector system was designed to be used with the St. George Recoil Mass Separator in studying alpha gamma reactions of astrophysical importance in inverse kinematics. Recoil nuclei were created by accelerating a stable, heavier nuclei onto a Helium gas target. The entire detector assembly will be placed at the focal plane at the end of separator. The detector system will be used to make a TOF vs E measurement, where two of these $E \times B$ designs are used to measure TOF and a commercial Si-strip detector is used to measure energy. The experiment requires 1 mm spatial resolution in one-dimension, which is well within the performance of the $E \times B$ MCP detector.

A research group at Michigan State University intends to measure the fission barriers for neutron-deficient nuclei such as ^{196}Pb and ^{121}Cs . Beams of ^{195}Tl and ^{120}Xe from the National Superconducting Cyclotron Laboratory (NSCL) will be produced via nuclear reactions and transported to the experimental setup. The setup will have one of the MCPs at the focal plane of the A1900, which is the magnetic separator used for separating the secondary beam. Two more MCP detectors will be placed ~ 30 m downstream

where the MCPs will be orthogonal to one another for TOF and position measurements. Downstream of the MCP detectors will be an ion chamber for a ΔE measurement. From the ΔE vs TOF they can identify the beam on an event-by-event basis. Downstream of the ion chamber will be an active target-time projection chamber (AT-TPC), which will be filled with hydrogen gas. The MCP tracking detector and the ion chamber will verify the charge of the beam is situated between the MCP and the AT-TPC detectors. They will measure the excitation function for proton-induced fission in order to extract the fission barriers.

Chapter 4

Simulations to understand detector performance

This chapter will focus on the factors that influence the spatial resolution of various PS-MCP detectors. The electron cloud size is calculated after it emanates from an MCP in order to understand the resolution of two simultaneous, but spatially separated particles. Simulations to understand the performance of the MCP-SW both with and without differential readout are discussed. Moreover, simulations to understand the spatial resolution of an $E \times B$ MCP detector are explored.

4.1 Geometric factors impacting the MCP electron-cloud size

As one goal in implementing the induced signal approach is to resolve two incident electrons that simultaneously impact the detector but are spatially resolved, it is necessary to know the size of the charge cloud. In order to understand the role of geometric factors in determining the size of the electron cloud, we constructed a simple model of the Z-stack MCP detector. Pores in the microchannel plates were represented by circles with a diameter of $10 \mu\text{m}$ with a $12 \mu\text{m}$ center-to-center spacing arranged in a hexagonal geometry. The registration of consecutive planes is assumed to be random to each other. Consistent with the impact of a single electron in the entry plane, a single pore is assumed to be struck on the entrance MCP. The overlap of that initial pore with the pores in the subsequent MCP plane is calculated as the registration between the two planes is varied. A single pore in the first plane is found to overlap with up to three pores in the second plane. In the third plane (MCP), while the most probable number of pores involved for a single incident electron is five, up to seven pores can be triggered. The true distribution of


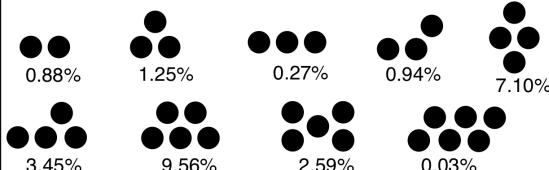
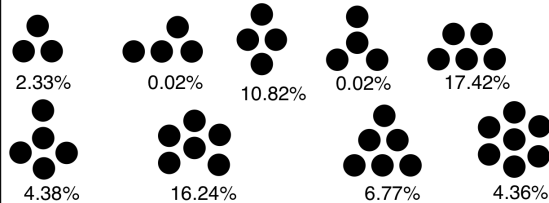
| $N_{\text{mid-layer}}$ | |
|------------------------|------------------------------------------------------------------------------------------------------------------------------------------------------------------------|
| 1 |  1.34% 3.02% 7.21% |
| 2 |  0.88% 1.25% 0.27% 0.94% 7.10% 3.45% 9.56% 2.59% 0.03% |
| 3 |  2.33% 0.02% 10.82% 0.02% 17.42% 4.38% 16.24% 6.77% 4.36% |

FIGURE 4.1: Predicted spatial configuration of activated pores at the exit of the Z-stack. The configurations are organized according to $N_{\text{mid-layer}}$, the number of pores struck in the middle MCP of the Z-stack. The percentages indicate the probability with which each configuration occurs.

pores might be slightly larger due to the angular divergence of electrons exiting one MCP and entering a subsequent MCP, which is not considered in the present simple geometric simulation.

In addition to investigating the number of pores triggered by an incident electron it is useful to examine the geometry of pores associated with the electron cloud. The spatial distribution of the pores predicted by the simulation is depicted in Fig. 4.1. The distribution of resulting shapes is organized according to the number of pores illuminated in the middle MCP of the Z-stack. From the shapes shown, a cloud diameter of $\approx 40 \mu\text{m}$ exiting the MCP can be deduced. This cloud diameter is smaller than that assumed in the simulations of Saito *et al* [118]. In that work, an initial cloud radius of $44 \mu\text{m}$, was assumed for a chevron arrangement of two MCPs with $25 \mu\text{m}$ pores. At a distance of 2.5 mm from the MCP this initial cloud was calculated to grow to a diameter of ~ 1.4 mm.

4.2 Calculating the growth of the MCP electron cloud

Prior work[118, 119] has successfully modeled the experimentally measured radius of the charge cloud. In order to calculate the size of the charge cloud for the conditions present in this study we followed the approach of Saito *et al* [118] and implemented a simple model to calculate the radial growth of the electron pulse as it leaves the MCP and propagates to the anode. The direction of the electric field, namely towards the anode is denoted as the dimension z . The electron cloud leaving the MCP is subdivided into a sequence of slices in time, each with an initial radius r_0 . Coulomb repulsion along the z -direction within a slice is assumed to be negligible and slices are taken to be independent. Associated with each slice is a current, I_s , given by:

$$I_s = I_0 \exp(-[(s\Delta t - t_0)/(\delta t/2)]^2) \quad (4.1)$$

where s represents the slice index with $s = 1, 2, 3, \dots$ and δt characterizes the width of the pulse while Δt represent the width of a slice. The time t_0 is the time at which the slice with the maximum current leaves the MCP. Governed by both its initial radial velocity and the Coulomb repulsion, the cloud grows in radius as it propagates towards the anode. From Gauss' law, under the assumption that the electric field emanating from the charge cloud has no z component, it can be shown that the radial growth of the cloud, with radius r , is governed by [118]:

$$\frac{d^2 r}{dt^2} = \frac{e}{m} \frac{I_s}{2\pi\epsilon_0 r \dot{z}} \quad (4.2)$$

where e is the unit charge, m is the mass of the electron, and ϵ_0 is the vacuum dielectric constant. The velocity in the z dimension is \dot{z} . The displacement of the slice from the MCP surface at time t is described by:

$$z = \frac{e}{m} \frac{E}{2} t^2 + \dot{z}_0 t \quad (4.3)$$

where \dot{z}_0 is the initial velocity of the electron in the z direction and E is the electric field. The initial velocities in the radial and z direction are simply the corresponding components of the initial velocity. Hence,

$$\dot{r}_0 = \sin \theta \sqrt{\frac{2eU}{m}} \quad (4.4)$$

$$\dot{z}_0 = \cos \theta \sqrt{\frac{2eU}{m}} \quad (4.5)$$

where U is the initial energy and θ is the angle with respect to the z direction. Consistent with earlier work [118] the distribution of initial energies and angles is taken as:

$$f_U(U) = \frac{U}{U_c^2} \exp(-U/U_c) \quad (4.6)$$

$$f_\theta(\theta) = \frac{\pi}{2\theta_{max}} \cos\left(\frac{\pi}{2} \frac{\theta}{\theta_{max}}\right) \quad (4.7)$$

Depicted in Fig. 4.2 is the growth of the electron cloud for different values of the initial energy, U , and emission angle, θ . Both the energies and emission angles chosen span the distributions presented above. The initial radius of the charge cloud was taken as 44 μm , the accelerating potential between the MCP and anode was chosen as 147 V, and the number of electrons exiting the MCP was taken as 1×10^7 . The width of the electron pulse, δt , was assumed to be 0.3 ns. Evident in panels a) and b) of Fig. 4.2 is that the rate of growth of the electron cloud radius, d^2r/dt^2 decreases rapidly as time increases, essentially independent of U or θ . After just 100 ps the acceleration is over an order of magnitude less than its initial value. The dependence of the radial velocity of the electron cloud on time is presented in panels c) and d) of Fig. 4.2. The rapid increase in the radial velocity with time lasts between ≈ 50 -100 ps after which the velocity is approximately constant. A larger dependence on energy as compared to angle is noted for the saturation value of the radial velocity. The saturation value of the radial velocity

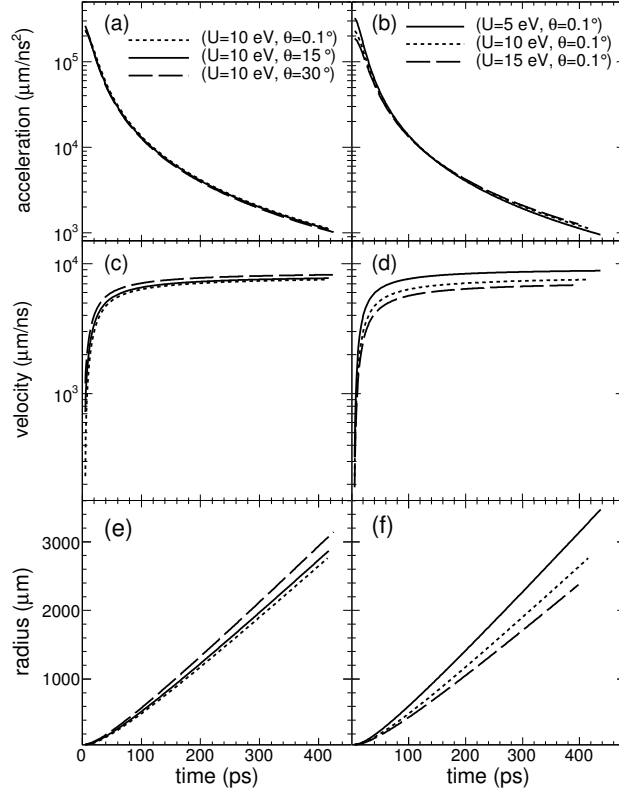


FIGURE 4.2: Growth of the electron cloud for different values of the initial energy, U , and emission angle, θ .

is 6000-8000 $\mu\text{m}/\text{ns}$. Shown in panels e) and f) of Fig. 4.2 is the dependence of the radius of the charge cloud on time. As expected, after the velocity has attained its saturation value, i.e. 100 ps, the radius depends linearly on time. The largest radii are obtained for the largest emission angles and the smallest energies. The energy dependence can be understood as due to the fact that for small energies the impact of Coulomb repulsion in broadening the electron cloud persists for a longer period of time.

To calculate the size of the charge cloud experimentally observed, the energy and angular distributions were sampled and the radial growth of the charge cloud was integrated using a fourth order Runge-Kutta algorithm. The electron pulse emanating from the MCP with an assumed width of $\delta t = 0.3$ ns was characterized by 100 slices along the z direction. Each slice had an associated current, I_s , as given by Eq. 3. The radial

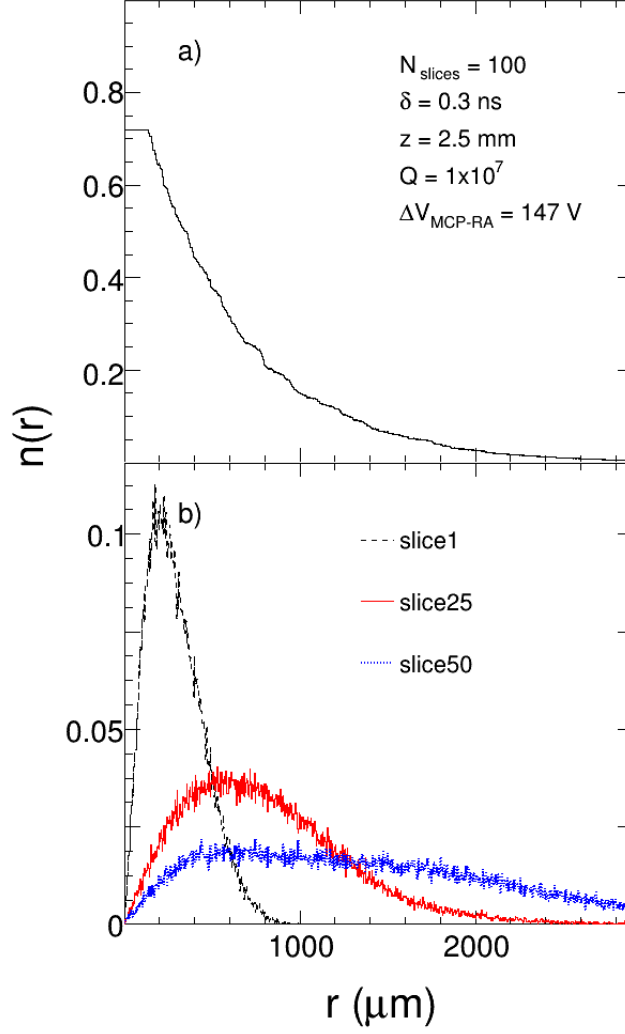


FIGURE 4.3: Panel a) Charge density distribution calculated at $z = 2.5$ mm for an electron cloud of 1×10^7 electrons. A total of 100 slices were used to characterize the cloud which had a width $\delta t = 0.3$ ns. Panel b) Distributions for the individual slices $s = 1, 25$, and 50. All the distributions have been scaled by a factor of 5×10^4 for clarity.

growth of each slice was calculated independently. The radial dependence of the resulting charge density distribution, $n(r)$, for all slices was calculated according to [118]:

$$n(r) = \sum_s \frac{I_s \Delta t}{r_s^2} \times f_U \times f_\theta \quad (4.8)$$

In Fig. 4.3 the total charge density distribution is shown along with the distribution

for $s = 1, 25,$ and 50 . When the current in a slice is small as in the case of $s = 1$, the charge density distribution is narrow and peaked at small values of r . With increasing current the charge density distribution becomes broader and shifts to larger values of r . The largest values of r are observed for the slice with the largest current, $s = 50$. The sum over all slices represents the charge density distribution of the entire electron cloud. This distribution exhibits a single peaked structure extending to $r = 3000 \mu\text{m}$ with the lower peak occurring at $\approx 60 \mu\text{m}$. When the distance between the MCP and anode is decreased from $z = 2.5 \text{ mm}$ to $z = 1.5 \text{ mm}$, the entire distribution $n(r)$ is compressed. When the number of electrons decreases to $\approx 2 \times 10^6$ electrons, the higher peak moves to lower values of r and is less discernible. If the size of the charge cloud is defined as the radius that encompasses 70% of the charge, a single radius can be obtained. Integration of the charge density distribution shown in Fig. 4.3a yields a radius of $694 \mu\text{m}$. The numerical results of our calculations are semi-quantitatively consistent with results previously reported [118].

4.3 Factors influencing the spatial resolution of the MCP-SW detector

In order to understand the factors limiting the extracted spatial resolution of $98 \mu\text{m}$ FWHM, simulations were performed. The simulations examined the impact of the delay line and the amplifier noise on the resolution of the MCP-SW detector. The induced signal was simulated by constructing the derivative of a Gaussian with an amplitude of 100 mV and a standard deviation of 2 ns . The resulting signal had an amplitude of 30 mV and a transition time from minimum to maximum of 4 ns . This transition time represents the inherent timing characteristics of the induced signal, which was measured using a sense wire harp without delay line readout. When inverted, this waveform both in amplitude and transition time provided a good description of the actual signals from the detector. The Y position was randomly chosen between 0 and 50 mm and the effect of the delay line on the signal propagating to the two ends of the delay line was accounted

for. The simulation utilizes the measured attenuation as a function of position on the delay line, V_{out}/V_{in} , given by:

$$\frac{V_{out}}{V_{in}} = (0.014y^2 - 2.09y + 104.72)/100 \quad (4.9)$$

where y is the distance from end of the delay line expressed in mm. The influence of noise on the extracted position resolution was accounted for by adding measured amplifier noise, nominally $\sim 1\text{--}1.5$ mV peak-to-peak, to the simulated signal. This noise was associated with digitized waveforms of induced signals just prior to an event on the detector. As a result, the noise is an adequate representation of the amplifier noise, but does not include noise associated with capacitive coupling to the MCP or anode. For each pair of up and down simulated signals, Y_{up} and Y_{down} , the zero-crossing point was determined by fitting a spline function to the transition region. The zero-crossing points $t_{Y_{up}}$ and $t_{Y_{down}}$ correspond to the delayed signal relative to a common reference time. The resolution was calculated by fitting a Gaussian to the distribution of $t_{Y_{up}} + t_{Y_{down}}$ and extracting its width (FWHM). The influence of noise on the resolution was determined by scaling the noise prior to its addition to the inverted derivative signal.

The results of the simulation are summarized in Fig. 4.4. The extracted resolution is shown as a function of the signal-to-noise (S/N) ratio in the simulation relative to the data. Three different cases were calculated to investigate the impact of the attenuation associated with three different delay line lengths. To calculate the resolution, for each combination of delay line length and S/N, 100,000 Y positions were chosen. The full attenuation (FA) case is for the delay boards used in the present setup, which have a length of 7771 mm. In the Half Attenuation (HA) case the length of the delay line is 3945 mm. The No Attenuation case corresponds to reading each sense wire out independently without the use of a delay line, hence decoupling the resolution achieved from the delay line approach. For a given delay line length, as S/N increases (achieved by reducing

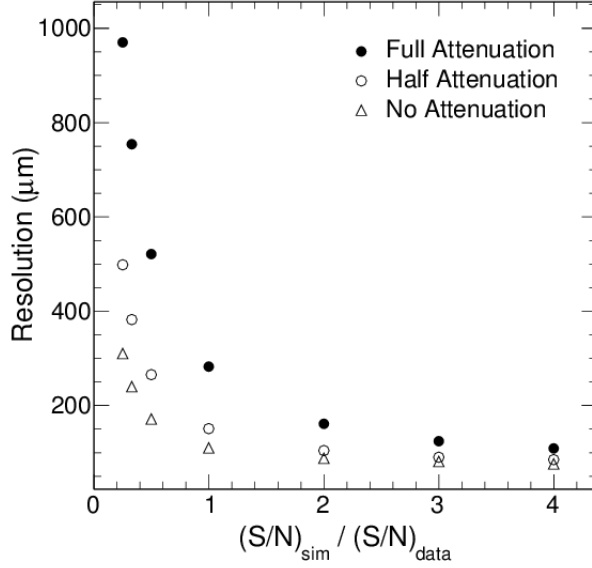


FIGURE 4.4: Simulated spatial resolution (FWHM) as a function of relative S/N ratio of simulation to data. Three cases are shown for the attenuation of the delay line: full attenuation, half attenuation, and no attenuation.

the noise) an improvement in the resolution is observed. For a given S/N, reducing the length of the delay line, and therefore the attenuation experienced by the signal, acts to improve the resolution. The detector as presently realized (FA, S/N=1) has a simulated resolution of $\sim 280 \mu\text{m}$ which is close to the resolution of $276 \mu\text{m}$ obtained experimentally for the raw data. The simulation demonstrates that if the half-length delay boards were used, even without a decrease in the noise, the resolution would improve to $\sim 150 \mu\text{m}$. In addition, if the amplifier noise was reduced by a factor of two, an improvement of the resolution to $\sim 104 \mu\text{m}$ could be achieved. The best spatial resolution achieved in the simulation, $\sim 76 \mu\text{m}$, is associated with decreasing the amplifier noise by a factor of four and reading out each wire independently. However, this readout scheme would undermine the simplicity and low cost of the existing induced signal approach. For comparison with the optimal simulation results, the best measured resolution obtained for the data using specific selection criteria, primarily the selection of larger amplitude signals, was $119 \mu\text{m}$.

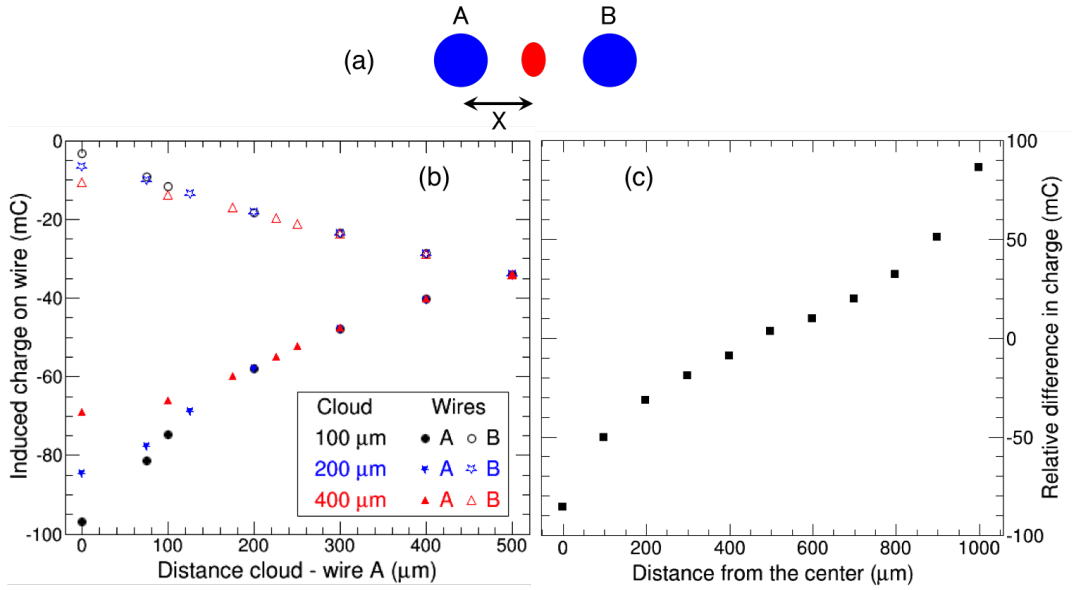


FIGURE 4.5: Results of Maxwell 2D simulations. The upper figure illustrates how the electron cloud (red oblong) is placed between wires A and B, where X defines the distance between the center of wire A and the center of the electron cloud. The lower figure is the plot of induced charge on the wire as a function of distance X. The open points represent the charge induced on wire B, while the closed points represent the charge induced on wire A. The simulations were performed for multiple charge-cloud sizes.

4.4 Understanding the spatial resolution of the MCP-SW detector with a differential readout

Maxwell 2D, a software program from Ansoft that solves Maxwell's equations for two-dimensional geometries, was used to study the charge induced on the sense wires. This calculation is not dynamic, but calculates for a given instant in time the charge on the sense wires when the charge cloud is at a specified distance from the sense wire plane. The charge cloud for each calculation is kept constant in each calculation, where the total charge is equal to 1 pC. The charge cloud is assumed to be a disk that extends from plus to minus infinity, or an infinite column of charge. The sense wires are assumed to be 25 μm in diameter with a pitch of 1 mm. Shown in Fig. 4.5a, is the drawing of the arrangement of the wires A and B with an electron cloud in between, where X which

defines the distance between the center of the electron cloud and the center of wire A. Shown in Fig. 4.5b, is a plot of charge induced on wires A and B as a function of the distance of the center of the charge cloud from the center of wire A.

Simulations were performed for 100 μm , 200 μm , and 400 μm diameter charge cloud sizes. For each charge cloud size, there is a monotonic decrease in the magnitude of the induced charge on wire A as the charge cloud is moved away from wire A. As the induced charge on wire A decreases, the charge on wire B increases. For distances larger than 200 μm , the induced charges converge such that there is no longer a dependence on charge-cloud size. At distances smaller than 200 μm , there is a difference in the induced charge for different charge-cloud diameters. Smaller charge clouds induce more charge on the wires than larger clouds. This result can be explained by Gauss's Law. When a charge cloud is sufficiently close to wire A, a larger charge cloud will intercept the wire. Thus, only a fraction of the charge cloud, the part outside of the wire, contributes to the induced signal. At the same distance, a smaller charge cloud would not intercept the wire and would lead to a larger induced signal because every charge cloud size has a total charge of 1 pC.

If one plots the difference in induced charge of wire B from wire A as a function of distance from wire A to the electron cloud (Fig. 4.5c), then one will see an anti-correlated relationship. The linear region of this plot spans from 200-800 μm . If we assume that we can detect differences over this 600 μm distance at the 10% sensitivity level then we should be able to achieve a position resolution of 60 μm .

These calculations indicate that independent readout of alternating wires in the sense wire plane is beneficial. This new delay board design provides an independent readout of the even and odd wires on a sense wire plane. Readout of the even and odd wires allows the differential measurement of the induced signal. This differential method should be sensitive to small differences in induced signals produced on adjacent

wires. It is anticipated that the use of the differential approach will result in a significant improvement in the position resolution achieved with the induced signal approach. In addition, use of the differential approach will reject noise common to both the even and odd wires.

4.5 Simulating the spatial resolution of the $\mathbf{E} \times \mathbf{B}$ detector

The significantly larger spatial resolution of $334 \mu\text{m}$ obtained with the ExB detector as compared to the $94 \mu\text{m}$ associated with the simple electrostatic arrangement indicates that the electron transport from the foil to the MCP dictates the measured resolution. To understand the electron transport in the crossed electric and magnetic fields between the secondary-emission foil and the front surface of the MCP detector we simulated the electron trajectories using the ion trajectory code SIMION [120]. Performing these calculations required mapping the magnetic field accurately as described below.

4.5.1 Mapping the magnetic field

The magnetic field in the active detector volume was measured using the DC Gauss-meter model GM1-ST [121]. This probe has a manufacturer quoted resolution of 0.1G and an accuracy of 1% of the measured value. This probe was capable of measuring one component of the magnetic field at a time. The probe was attached to a machined aluminum block and moved in a precise manner to map the magnetic field in increments of 12.7 mm in each dimension. In this manner a two-dimensional plane of one component of the magnetic field was produced. By use of precision spacers additional magnetic grid planes were measured. The resulting three-dimensional grid was interpolated to the 1 mm level and used for the subsequent simulations. The X-dimension is defined along the beam axis, the Y-dimension is defined as the principal direction of the magnetic field, and

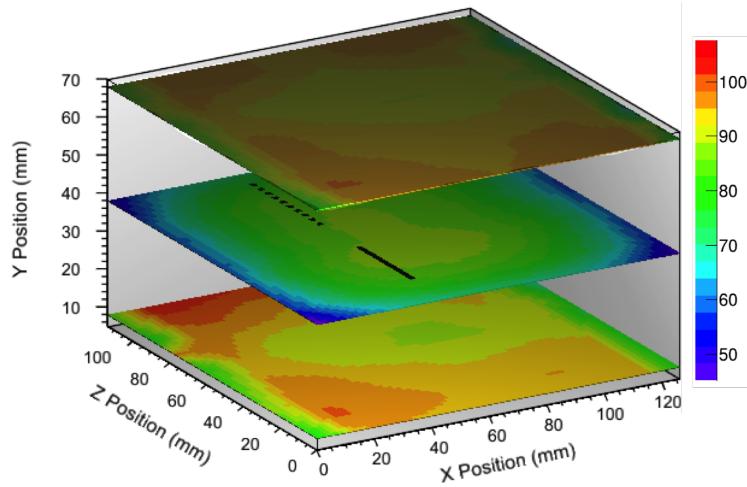


FIGURE 4.6: The magnetic field component, B_Y , in the XZ plane is presented for the $y = 8, 38, 68$ mm. The Y-dimension is defined as the principal direction of the magnetic field while the X-dimension is associated as the direction of the incident ionizing particles. The Z-dimension is perpendicular to both the X and Y dimensions using the right hand rule. The solid and dashed lines shown in the $Y=38$ mm plane indicate the positions of the foil and MCP respectively.

the Z-dimension is perpendicular to both the X and Y dimensions. The other components of the magnetic field were measured by rotating the aluminum block with the probe attached and repeating the procedure. The B_Y component of the magnetic field is shown in Fig. 4.6. The B_Y component of the magnetic field is shown in the XZ plane for three positions in the Y-dimension, with $y=38$ mm corresponding to the center of the detector. As is evident from the figure, the magnetic field in a plane exhibits some asymmetry. We attribute this asymmetry to the magnets not being identical and to their placement on the iron plates. The solid and dashed lines for $y = 38$ mm indicate the positions of the foil and MCP respectively. In the active region, the variation of the magnetic field in the principal direction is approximately ± 5 G.

For the α -particles incident on the 13 slits, the final YZ positions are shown in Fig. 4.7. In the case of $B_Y = 90$ G and $B_X = B_Z = 0$ G, presented in Fig. 4.7a, the image of the slits is observed as twelve vertical stripes. For reference, the area of the multi-strip

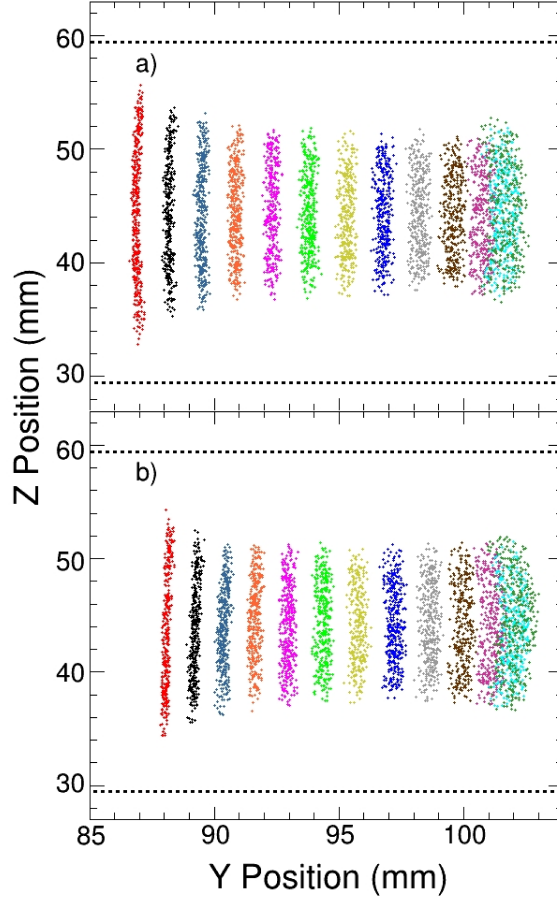


FIGURE 4.7: (a) Slit image predicted by SIMION at the anode position for the case of $B_Y = 90\text{G}$ and $B_X = B_Z = 0\text{G}$. (b) Slit image predicted by SIMION at the anode position for the case of the measured magnetic field.

anode is depicted by the dashed lines. As one moves to larger Y position, the width of each stripe increases resulting in poorer resolution. For the two slits at the largest value of Y , the slits are unresolved from each other. Thus the trend of resolution with position observed in Fig. 3.18 is reproduced. Two additional features can be noted in Fig. 4.7b. The vertical extent of the central stripes is somewhat smaller than that of the edge stripes indicating a contribution of focusing in the image by the field. In addition, the rightmost stripe exhibits a curvature not observed for the other stripes. Given the 7 mm resolution in Z , by replacing the multi-strip anode with a cross-strip anode [41] a two-dimensional position measurement could be implemented.

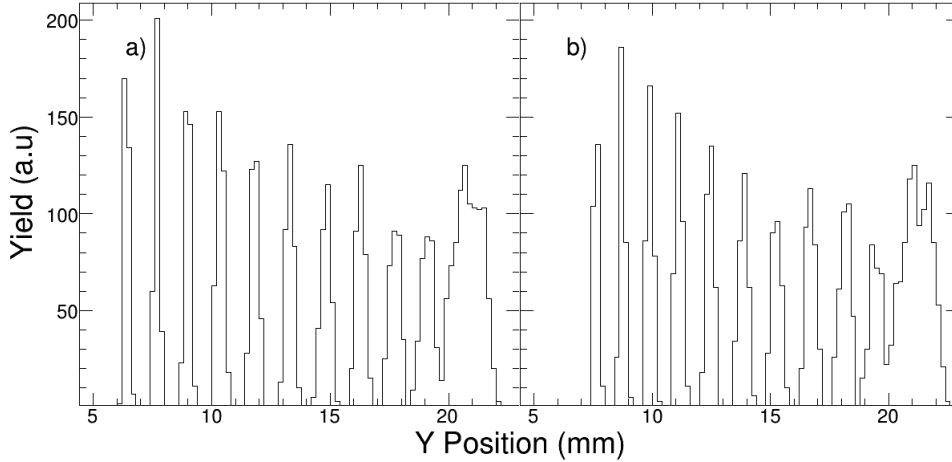


FIGURE 4.8: SIMION simulations of the position spectrum of electrons generated by α particles passing through slits in the calibration mask. The initial kinetic energy and angular distribution of the electrons was assumed to be 3eV and a cone with a 30° half angle respectively. Panel a) A constant magnetic field of $B_Y = 90\text{G}$ was used together with B_X and $B_Z = 0\text{G}$. Panel b) A measured magnetic field was used whose principal axis is presented in Fig. 4.6.

4.5.2 Simulating the spatial resolution

Using the measured magnetic field together with the SIMION-calculated electric field, the trajectory of electrons in the detector was simulated using the program SIMION [120]. To evaluate the spatial resolution, 100,000 electrons were generated on the masked, aluminized mylar foil and transported through the crossed magnetic and electric fields. An initial kinetic energy of 3 eV was assumed for the electrons, consistent with the most probable initial electron energy for a similar experimental setup [63]. Although the initial kinetic energy distribution of ejected electrons extends out to 100 eV [63], it suffices to choose 3 eV for the initial energy as the large bias potential applied to the electron emission foil overwhelms the initial kinetic energy chosen. To begin, we simulated the electron transport in a magnetic field with $B_Y = 90\text{G}$ and $B_X = B_Z = 0\text{G}$. Electrons were assumed to be emitted within an initial angular cone with a half angle of 30° [63] with one electron emitted for each incident α -particle. The simulated position spectrum on the MCP is depicted in Fig. 4.8a. Eleven peaks are observed with the peak

at $Y=21$ mm significantly broader than the rest. The average spatial resolution of the ten narrower peaks observed in Fig. 4.8a is $572 \mu\text{m}$ FWHM. We also investigated the electron transport in the measured magnetic field for the same initial kinetic energy and angular distribution previously used. The simulated position spectrum for the measured magnetic field is depicted in Fig. 4.8b. The results of this magnetic field calculation are fairly similar to the previous case. The slight difference observed is that the broad peak at $Y>20$ mm appears to be splitting into two peaks as evident in Fig. 4.8b. The average spatial resolution of the ten peaks with $Y < 20\text{mm}$ is $647 \mu\text{m}$ FWHM. The larger spatial resolution associated with the calculations utilizing the measured magnetic field indicate that variations in the field degrade the resolution. Efficiency was defined as the percentage of initial electrons originating from the slits that subsequently reach the multi-strip anode, which was determined to be $\sim 88\%$ for both the measured and constant field simulations. We also investigated the position sensitivity in the Z-dimension using the same approach that was used in the Y-dimension. The position sensitivity in this dimension was determined to be ~ 7 mm. This poorer resolution in the Y-dimension can be understood if one considers the electron trajectories in the magnetic field. Although it is only possible to achieve good position resolution in one dimension, by coupling two $E \times B$ detectors oriented orthogonally, a 2D position image of a beam can be achieved.

Chapter 5

Conclusions

The summary of the results in this dissertation is organized by detector and presented below. These results are depicted in a synopsis table, Table 5.1. In this table, the best resolution achieved for each approach can be discerned.

TABLE 5.1: Summary of the best spatial resolution achieved with each PS-MCP detector.

| PS-MCP Detector | Intrinsic Spatial Resolution FWHM (μm) |
|---------------------------------------------|--------------------------------------------------------|
| First Generation Induced Signal | 466 |
| Second Generation Induced Signal– 2 GS/s | 169 |
| Second Generation Induced Signal– 5 GS/s | 159 |
| Second Generation Induced Signal– 10 GS/s | 98 |
| Induced Signal for Slow Neutron Radiography | 216 |
| Resistive Anode | 157 |
| Resistive Anode– Risetime Analysis | 64 |
| Multi-Strip Anode (delay line) | 94 |
| E×B with Multi-Anode for Beam Imaging | 334 |

5.1 The MCP-SW detector

The second generation of a MCP-SW detector with position-sensitivity has been designed, fabricated, and optimized. Position-sensitivity was achieved by utilizing a MCP coupled to a sense wire harp with delay line readout. Signals arriving at either end of the delay line were digitized by high speed digitizers and subsequently analyzed. To measure the position-sensitivity, the masked detector was exposed to a low intensity source of electrons. The simplest analysis provided a measured spatial resolution of 276 μm FWHM. To understand the factors that limit the measured spatial resolution,

simulations were performed. These simulations predict a spatial resolution of $280 \mu\text{m}$ FWHM. The fact that the resolution of the simulation reproduces the measured resolution achieved with the simplest analysis suggests that the primary factors influencing the resolution are understood. The simulation also demonstrates that if the signal attenuation is reduced by use of a shorter delay line the resolution would improve to $\sim 150 \mu\text{m}$. If the amplifier noise was additionally reduced by a factor of two, an improvement of the resolution to $\sim 104 \mu\text{m}$ could be realized. The simulations indicate that use of a high quality PCB material, which minimizes the attenuation and dispersion of the signal significantly affects the position resolution obtained. With the existing detector and a delay line of ≈ 50 ns, the measured spatial resolution was improved to $119 \mu\text{m}$ by use of digital signal processing techniques and implementation of signal selection criteria. This measured resolution of $119 \mu\text{m}$ FWHM corresponds to an intrinsic resolution of $98 \mu\text{m}$ FWHM.

This improvement in the spatial resolution from $466 \mu\text{m}$ first reported with the first generation detector to $98 \mu\text{m}$ FWHM, with this detector, represents a significant advance using the induced signal technique. After obtaining this resolution with the 50 ns delay line, we also improved the linearity of the induced signal approach by using a shorter delay line with a length of 25 ns. With this new delay board, the linearity improved from $\pm 2\%$ to $\pm 0.5\%$. We also determined the impact of the sampling frequency on resolution and found that 10 GS/s digitization is necessary to obtain the optimal resolution of $98 \mu\text{m}$. The resolution achieved was not improved by using 20 GS/s digitization. It was also possible to achieve $159 \mu\text{m}$ and $169 \mu\text{m}$ resolution with sampling frequencies of 5 GS/s and 2 GS/s digitization, respectively. This present design provides competitive spatial resolution as compared to other existing approaches, and may provide a more cost effective means of imaging using MCP technology. The scalability of this approach makes it a good choice for imaging with larger MCP detectors ($10 \text{ cm} \times 10 \text{ cm}$ and $20 \text{ cm} \times 20 \text{ cm}$) presently under development.

A simple model that considered only geometric factors revealed that geometric factors alone were responsible for a cloud diameter of $\approx 40 \mu\text{m}$ exiting the MCP Z-stack. Modeling the growth of the electron cloud as it propagates to the anode demonstrated that the charge density distribution incident on the anode, at a distance of 2.5 mm from the MCP, has a peak at $60 \mu\text{m}$ (radius). Within a radius of $694 \mu\text{m}$ 70% of the charge cloud is encompassed. For the conditions investigated with the model, these latter values for the size of the charge cloud define the ability of a sense wire plane to spatially resolve two simultaneous ionizing events.

5.2 The MCP-RA detector

A RA detector along with an in-house readout electronic system was developed. The objective of developing this RA detector was to enable characterization of the induced signal shape by placing the RA detector directly behind the sense wire plane. The RA could thus provide an independent measure of position and be used to characterize the dependence of the induced signal on position. Unfortunately, the RA signals exhibited a large capacitive coupling with the sense wires, thus undermining its use as a tool in the characterization of the significantly smaller induced signals. Nonetheless, optimizing the spatial resolution of a Z-stack MCP-RA detector when illuminated by a low-intensity electron source was investigated. A low-intensity source of electrons was obtained by bombarding a mylar foil with incident α particles from a ^{241}Am source. Using this approach each ionizing event consisted of typically six electrons at a rate of 7 counts sec^{-1} incident on the masked Z-stack detector. With this electron source the dependence of the position resolution on the distance between the RA and MCP stack was examined. For the central region of the detector the resolution did not depend strongly on the MCP-RA distance increasing from $317 \mu\text{m}$ to $413 \mu\text{m}$ as the distance increases from 2.5 mm to 11 mm. The position resolution was determined to depend on the potential

difference between the MCP and RA, as well as the total charge of the electron cloud, Q_{MCP} . Requiring that the total charge of the RA equals the charge measured by the MCP provided an improvement in the measured resolution. The best measured resolution achieved was $170 \mu\text{m}$ (FWHM) which corresponds to an intrinsic resolution of $157 \mu\text{m}$ (FWHM) for the standard charge division approach.

A charge division approach from the four corners of the RA is typically utilized to extract the centroid of the electron cloud emanating from the MCP. The signals arriving at the four corners of the RA manifest a broad range of risetimes. For a 40 mm diameter MCP-RA detector, risetimes from $< 1\mu\text{s}$ to approximately $40 \mu\text{s}$ are observed. By digitizing the signals from the MCP-RA with a high speed digitizer, digital signal processing techniques were utilized to extract both the charge collected at each corner as well as the risetime of the four signals for each incident electron. Implementation of the charge division approach resulted in a resolution of $\approx 190 \mu\text{m}$ (FWHM), comparable to that obtained with analog electronics. Examination of the digitized signals reveals a clear correlation between the risetime of the signals and the position of the electron cloud. By using this correlation between risetime and position together with the charge division method a measured position resolution of $\approx 90 \mu\text{m}$ (FWHM) was achieved, corresponding to an intrinsic resolution of $64 \mu\text{m}$ (FWHM). This result represents a significant improvement in the position resolution obtained. It was also observed that in the central region of the detector the risetime is extremely sensitive to the position of the electron cloud. While this latter observation requires further investigation for full characterization, it presents intriguing possibilities for enhanced imaging capabilities.

5.3 Beam imaging

Although not a central point of this work, an $E \times B$ MCP detector with position-sensitivity in 1-dimension has been developed. This detector enables the imaging of

low-intensity radioactive beams. Position-sensitivity was achieved by utilizing a MCP coupled to a multi-strip anode with delay line readout. Signals arriving at either end of the delay line were digitized by high speed digitizers and subsequently analyzed. To measure the position-sensitivity, a mask was inserted and the detector was exposed to α -particles from an ^{241}Am source. While the simplest analysis provided a measured spatial resolution of $520\ \mu\text{m}$ FWHM, use of digital signal processing techniques along with use of signal selection criteria improved the spatial resolution to $413\ \mu\text{m}$. This measured resolution of $413\ \mu\text{m}$ FWHM corresponds to an intrinsic resolution of $334\ \mu\text{m}$ FWHM. To understand the measured resolution, the magnetic field was mapped, and the trajectories of ejected electrons were calculated using the program SIMION. For a constant magnetic field of $B_Y = 90\text{G}$ and $B_X = B_Z = 0\text{G}$, simulations predict a spatial resolution of $572\ \mu\text{m}$ FWHM. Use of the measured magnetic field results in a spatial resolution of $647\ \mu\text{m}$ FWHM. This approximate agreement of the simulation with the measured resolution suggests that the primary factors that influence the resolution are understood. The simulations demonstrate that the primary factor dictating the measured resolution is the electron transport from the foil to the MCP.

Although the present design only provides sub-millimeter position sensitivity over a limited region in one-dimension, this development of a compact, high-rate position-sensitive $E \times B$ detector has been productive. Two radioactive beam facilities, Michigan State University and the University of Notre Dame, have already built (or are constructing) an $E \times B$ MCP detector based on the design presented in this thesis. The detector at Notre Dame will be used to study alpha gamma reactions of astrophysical importance. The detector at Michigan State University will be used in experiments aimed at measuring the fission barriers for neutron-deficient nuclei such as ^{196}Pb and ^{121}Cs . This detector will also be utilized in upcoming experiments by the Indiana University Nuclear Chemistry Group. These experiments will involve measurement of the fusion cross-section of neutron-rich light and mid-mass systems at near-barrier energies. The detector will be

used in an E vs TOF measurement as the timing detector. In addition to providing the start time for the TOF measurement, the E×B MCP detector will be utilized to image the incident beam allowing selection on regions of the image. This capability will enable rejection of beam halo and improve the measurement of the angular distribution of fusion products. In addition to its use in these specific experiments, this detector also has the potential to be used as a diagnostic tool to aid the tuning of a radioactive beam at an accelerator facility.

5.4 Neutron radiography

Work in the development of MCP detectors for neutron radiography is particularly exciting as the MCP efficiency is much larger than the efficiency obtained with the traditional scintillator/CCD detection scheme. The induced signal approach has been utilized to construct a 2D imaging detector for slow neutron radiography. This detector was realized by inserting a boron-doped MCP detector in front of the MCP-SW previously described. Induced signals from the ends of the delay line in the X and Y dimension were digitized by high speed digitizers. The first incarnation of the DAQ, a VME based system, was limited to count rates of 300 cps. Due to the high value of beam time, a new efficient DAQ capable of acquiring at much higher rates was developed. This PCIe based DAQ can digitize the waveforms from the PS-MCP detector at rates up to 200k cps. A TDC was also developed and incorporated into the DAQ to allow for selection of events based on neutron energy. While the present measurements were restricted to conventional neutron radiography, future plans include transitioning to radiography involving novel contrast mechanisms (e.g. Bragg edge scattering). To assess the spatial resolution of the detector, the masked detector was illuminated with a beam of slow neutrons from the LENS facility at Indiana University. The simplest analysis provided a measured spatial resolution of 676 μm FWHM. This measured spatial resolution was improved to 329

μm FWHM through digital signal processing and utilization of selection criteria. The largest improvement in the resolution was associated with implementation of a threshold requiring a minimum signal amplitude for the induced signals. This measured spatial resolution of $329 \mu\text{m}$ FWHM corresponds to an intrinsic resolution of $216 \mu\text{m}$ when the effect of the finite slit width is de-convoluted. While this approach does not provide the best spatial resolution achieved with slow neutron radiography, it does provide an alternative approach that is more cost effective. The relatively low cost of this approach makes the tiling of large areas more feasible.

5.5 Outlook

Using the induced signal approach a competitive, spatial resolution of $98 \mu\text{m}$ FWHM (see Section 2.1.5.2) has been achieved. As simulations suggest that $76 \mu\text{m}$ FWHM (see Section 4.3) is the fundamental limit of the induced signal approach with the existing amplifier noise, further effort to substantially improve the spatial resolution is probably not warranted. Consequently, the future direction of the project is centered on applications. One such application could be the continuation of the slow neutron radiography measurements initiated in this thesis. To date, radiography has only been performed at LENS, a neutron source not optimized for radiography. State-of-the-art radiography is performed at facilities such as PSI or LANSCE, where the beam divergence is minimized and neutron flux is maximized. In order to take advantage of these higher neutron fluxes of 2×10^6 neutrons/s, the DAQ throughput would need to be improved by approximately a factor of ten. One way to improve this throughput would be to incorporate a new digitizer into the DAQ. The SP Devices ADQ7 digitizer, which has just become available, is particularly appealing as it offers the user access to the FPGA on the digitizer board. This enables digital signal processing routines to be executed within the FPGA allowing

extraction of the zero-crossing point in real time. As a result, the amount of data transferred would be minimized, permitting higher data rates to be realized. In addition, less storage space is required to describe the waveform. Moreover, this digitizer offers digitization at a sampling frequency of 10 GS/s, which is necessary to achieve a resolution of 98 μm . This higher sampling frequency, as demonstrated in this thesis should result in an improved spatial resolution for the neutron radiography provided the neutron source is not the limiting factor.

Aside from improvements to the DAQ, there are improvements to the neutron radiography experimental setup that could also be implemented. One such improvement would be in the throughput of the data for a high-quality image. To obtain the best resolution required a minimum amplitude of the induced signals. This requirement resulted in a rejection of 99% of the data. To increase the amplitude of the induced signals, atomic layer deposition could be utilized to increase the gain of the MCPs [122]. Alternatively, a different neutron converter could be used in front of the MCP stack, such that the associated neutron events will receive the full amplification of the MCPs. This could be achieved using a Gd foil. An additional benefit of using a Gd foil is the Gd has a larger neutron capture cross-section than ^{10}B . In expanding beyond the realm of conventional radiography, the LENS facility could still be utilized as a testbed for advanced forms of radiography such as Bragg edge scattering radiography [77, 78]. Following the initial implementation of a high contrast radiography technique with this detector, neutron tomographic measurements performed at a state-of-the-art facility like PSI or LANSCE would be the next logical step.

The LENS facility provides a good test environment within which to develop an improved detector and DAQ. It may also provide a reasonable environment within which to become familiar with advanced radiographic techniques such as Bragg edge scattering.

Following implementation of these improvements, utilizing this detector at the state-of-the-art facilities such as PSI or LANSCE are envisaged.

Appendix A

Signal processing for the resistive anode

Standard digital signal processing techniques are used on the CSA signals to extract the position resolution using gaussian and trapezoidal filter algorithms [71, 123–125]. To efficiently process the pulse shapes, recursive relations of both the filters were employed. For the gaussian shaper, the input signal is subjected to a combination of high-pass and low-pass filters. Each sample, i of the j^{th} channel CSA is subjected to a single-pole, high-pass digital filter using the following recursive relation [71]

$$\begin{aligned} HP_{out}^j[i] &= a_{HP}^0 CSA^j[i] + a_{HP}^1 CSA^j[i - 1] \\ &\quad + b_{HP}^1 HP_{out}^j[i - 1] \end{aligned} \quad (\text{A.1})$$

where a_{HP}^0 , a_{HP}^1 , and b_{HP}^1 are the coefficients of the high-pass filter kernel, which can be calculated from the following equations

$$a_{HP}^0 = (1 + e^{-1/\Delta_H})/2 \quad (\text{A.2})$$

$$a_{HP}^1 = -(1 + e^{-1/\Delta_H})/2 \quad (\text{A.3})$$

$$b_{HP}^1 = e^{-1/\Delta_H} \quad (\text{A.4})$$

Δ_H refers to the number of samples being considered for the high-pass time constant. The factor e^{-1/Δ_H} decides the sample-to-sample decay for a given time constant. Equation (A.1) mimics an analog differentiator circuit whose RC constant can be controlled by using the parameter Δ_H (in the units of number of samples). A time constant of 500 ns was used for all the channels of CSA. Due to finite length of the exponential tail of input signal, the high pass filter output may overshoot the baseline of the pulse. This tendency can be corrected by using a pole-zero recursive relation [72]. We utilized the pole-zero recursive relation given by the following equation

$$HP_{corr}^j[i] = HP_{out}^j[i] + PZC \times CSA^j[i - 1] \quad (\text{A.5})$$

where PZC is a pole-zero correction factor. The value of PZC can be chosen so as to correct for the overshoot. The second term provides the amplified (attenuated) exponential tail of the input pulse which corrects against the pole present in the exponential part of HP_{out}^j . The pole-zero corrected output of the high-pass filter is then transformed by a four-pole, low-pass digital filter, which is realized by the following recursive relations [71]

$$\begin{aligned} GSH^j[i] = & a_{LP}^0 HP_{corr}^j[i] + b_{LP}^1 GSH^j[i - 1] \\ & + b_{LP}^2 GSH^j[i - 2] + b_{LP}^3 GSH^j[i - 3] + b_{LP}^4 GSH^j[i - 4] \end{aligned} \quad (\text{A.6})$$

where $a_{LP}^0, b_{LP}^1, b_{LP}^2, b_{LP}^3, b_{LP}^4$ are the coefficients of a low-pass filter kernel and GSH^j refers to the semi-gaussian shaper output obtained for the j^{th} channel. The corresponding coefficients for the low-pass filter is given as

$$a_{LP}^0 = (1 - e^{-1/\Delta_L})^4 \quad (\text{A.7})$$

$$b_{LP}^1 = 4e^{-1/\Delta_L} \quad (\text{A.8})$$

$$b_{LP}^2 = -6(e^{-1/\Delta_L})^2 \quad (\text{A.9})$$

$$b_{LP}^3 = 4(e^{-1/\Delta_L})^3 \quad (\text{A.10})$$

$$b_{LP} = -(e^{-1/\Delta_L})^4 \quad (\text{A.11})$$

where Δ_L is the low-pass time constant of the high-pass filter. For each corner of the resistive sheet, the measured charge is obtained by determining the height of the semi-gaussian shaper output.

To ensure that the extracted resolution was not limited by the particular filter chosen, we also implemented a trapezoidal digital filter to extract the charge of the input signals. The following recursive relations are used for the j^{th} channel CSA

$$d^{k,j}[i] = CSA^j[i] - CSA^j[i - k] \quad (\text{A.12})$$

$$d^{k,l,j}[i] = d^{k,j}[i] - d^{k,j}[i - l] \quad (\text{A.13})$$

$$p^j[i] = p^j[i - 1] + m_2 d^{k,l,j}[i] \quad (\text{A.14})$$

$$r^j[i] = p^j[i] + m_1 d^{k,l,j}[i] \quad (\text{A.15})$$

$$s^j[i] = s^j[i - 1] + r^j[i] \quad (\text{A.16})$$

Here k represents the number of samples in the rising edge while l is the total number of samples in the rising as well as in flat top region of the trapezoid shaped signal, m_2 is the gain of the filter, m_1 is the pole-zero correction factor, and s^j is the output of the filter.

The correction factor depends on the decay time constant (τ) of the preamplifier, given by the following equation [124]

$$m_1 = \frac{m_2}{e^{(T_{clk}/\tau)} - 1} \quad (\text{A.17})$$

where T_{clk} is the sample resolution of the digitizer. For shaping the CSA signals both the rising and flat top lengths are chosen to be 500 ns and the sample resolution is taken to be 4 ns. The gain of the shaper is taken to be unity, while the decay time constant is chosen to be 30 μs to match the decay constant of the CSA. Charge collected at each corner of the RA is calculated by taking the average height of the trapezoidal output.

Appendix B

Wire winding manual

B.1 To use the wire winder

1. Clean wire winder with ethanol if it is dusty/dirty.

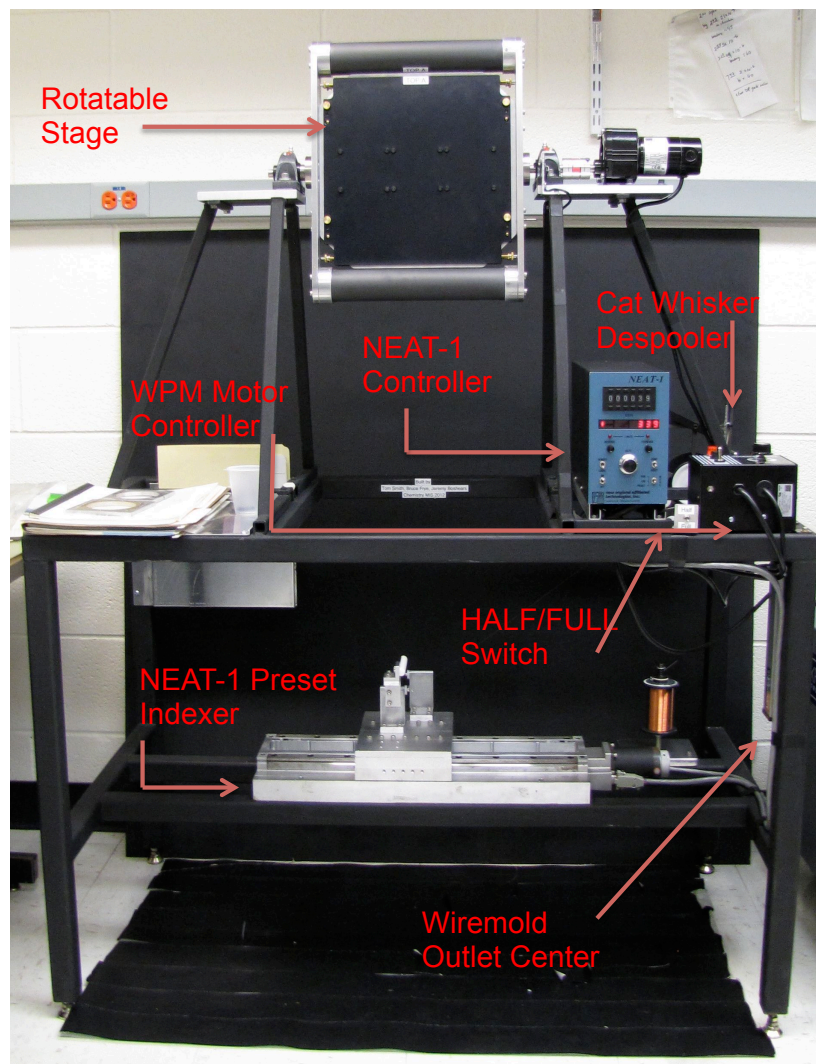


FIGURE B.1: The wire winder and all of its main components

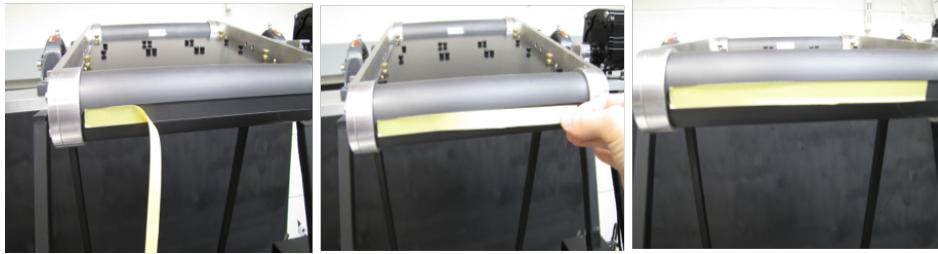


FIGURE B.2: Depiction of how Mylar tape should be overlaid into groove

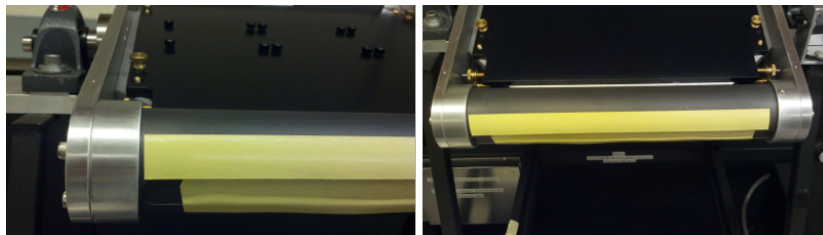


FIGURE B.3: How tape should be overlaid on the top and bottom of the curved edges

2. Sand down the curved side of the white Nylon piece on stepper motor, immediately above the Preset Indexer. Use 600 grade silicon carbide sandpaper to accomplish this. Over time, the wire can wear a groove into the Nylon piece. Alan Eads recommends that this step should be done every time a new wire harp is wound. Once the sanding is complete, clean the platform below the Nylon piece as well as the Nylon piece itself with ethanol in order to rid of the surfaces of any particulates. Or for even better practice put a Kimwipe under the Nylon piece prior to the sanding step to catch falling particulates and then clean the piece with ethanol.
3. Check to see if the WPM motor controller is set to 0 (dial is turned all the way counterclockwise) and its switch is set to the OFF position.
4. Plug in the power strip, which is labeled the Wiremold Outlet Center, into a dirty power outlet.

5. Flip the red switch on the power strip, the wpm DC motor, and the Neat-1 Controller to the ON position.
6. Wipe down the curved ends of the rotatable stage with ethanol and then place a piece of Mylar double sided tape, which is long enough to cover the total wire winding distance, onto the curved edges; as seen in Fig. B.2 and B.3. If the Mylar tape will not stick to the rotatable stage, wipe down the curved ends with acetone, then isopropanol, then ethanol. The Mylar tape that is placed in the groove is meant to catch epoxy that may flow into the groove after application of the epoxy in step 15. The Mylar tape that is placed on the top and bottom of the curved edges is meant to affix the wires in place such that the wires will not be disturbed. A tip is to stick one end of the tape to the surface, keep the rest of the tape taut, and then lay down the remainder of the tape. One can also tap the tape down to eliminate air bubbles, but make sure to do this step with the plastic covering still attached to the tape adhesive. Rotate the stage as needed.
7. Set the NEAT-1 Controller RATE to a high number (typically 10). A higher number creates less mechanical noise from the Neat-1 Preset Indexer, or stepper motor. Check to make sure the REMOTE-LOCAL switch is set to LOCAL. When the switch is set to LOCAL, the Preset Indexer will move in response to a pulse from the Controller. When the switch is set to REMOTE, no pulse will reach the Indexer. Set the mode switch to RUN. In the RUN mode the motor will rotate so long as the REVERSE or FORWARD button is depressed. The rate of rotation is controlled by turning the RATE knob and was operated at 10 typically for the reason listed above. Depress the FORWARD button until the LED for the reverse limit switch lights (labeled as limits) up. Toggle the RESET switch to set the LED display to 0. Depress the REVERSE button until the LED display reads to some number slightly greater than -14036 (this is for winding on the left board). Set the

mode switch to JOG and depress the REVERSE button until the LED displays -14036. When the mode is set to JOG, the motor will take one step clockwise if the FORWARD button is depressed, and one step counterclockwise if the REVERSE button is depressed. The LED display will function as a position register. Set the mode switch to PRESET. Once the indexer is set to PRESET mode and the FORWARD or REVERSE button is depressed, the motor will move a predetermined number of steps corresponding to 6 digit preset switches on the NEAT-1 controller. Once the NEAT-1 controller is in PRESET mode it will move in the direction of the last specified direction (i.e., use the REVERSE function last if winding from left to right.) Depressing the REVERSE button, which was done above in JOG mode, orders the Indexer to step from left to right because the lead screw will rotate counterclockwise. The wire is unwound more consistently when the indexer is translated from left to right, as opposed to from right to left.

8. Set the 6 digit preset switches on the Neat-1 Controller according to the desired spacing between wound wires. The preset switch to the far right is the least significant digit and corresponds to a 0.001 inch step. Note that setting the Full/Half switch to HALF will make this digit correspond to a 0.0005 inch step. Typically this switch will be set to HALF at the value of 000079 (corresponds to 1mm).
9. Clean surface of pcb using flux remover, followed by propanol, followed by ethanol. Unscrew the mounting screws, seen in Fig. B.5, on the mountable plate. Place the printed circuit board on the mountable plate. Then, use the allen screws to connect the circuit board to the mountable plate. If desired, tape may be used instead of the allen screws to mount the printed circuit board onto the mountable plate. One may mount printed circuit boards to the sister mountable plate. The mountable plates are labeled TOP A and TOP B. Use of both mountable plates conserves the use of the gold plated tungsten wire, which is a fairly expensive wire.

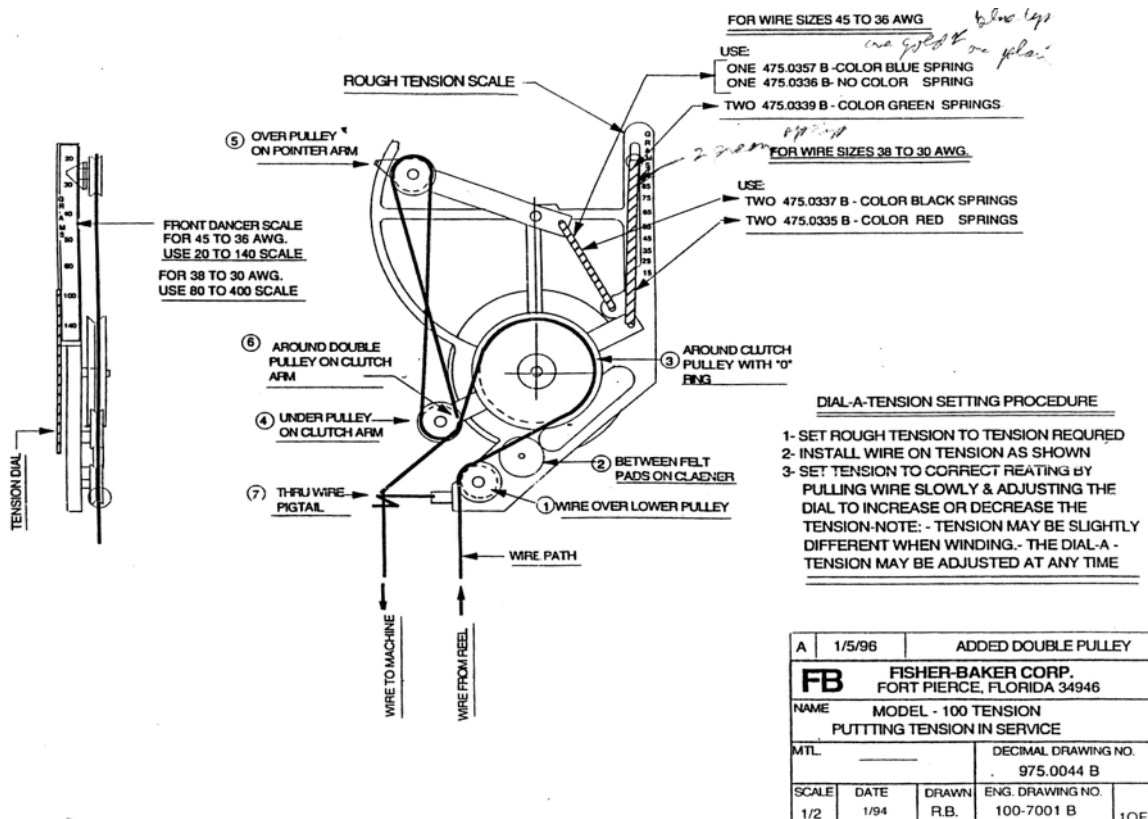


FIGURE B.4: The DIAL-A-Tension device, which is a part of the Cat Whisker Despooler, with all of its labeled components

10. Squirt a small amount of ethanol to the cleaner pulley shown indicated by (2) in Fig. B.4. One has the option to hold a drip pan underneath the cleaner pulley to collect excess ethanol. It is important to clean any residue off the wire especially if the wire plane will be used for a detector.
11. String the wire in the DIAL-A-TENSION device as indicated in Fig. B.4. Tape the wire to the underside of the mountable plate labeled TOP B. Tape to the mark labeled with the white paint for winding a wire plane in the left third of the mountable plate. The mountable plate can be seen in Fig. B.5. Taping the wire can be seen in Fig. B.6 where the center position is used. Note this guide will be focusing on the right side of TOP B.

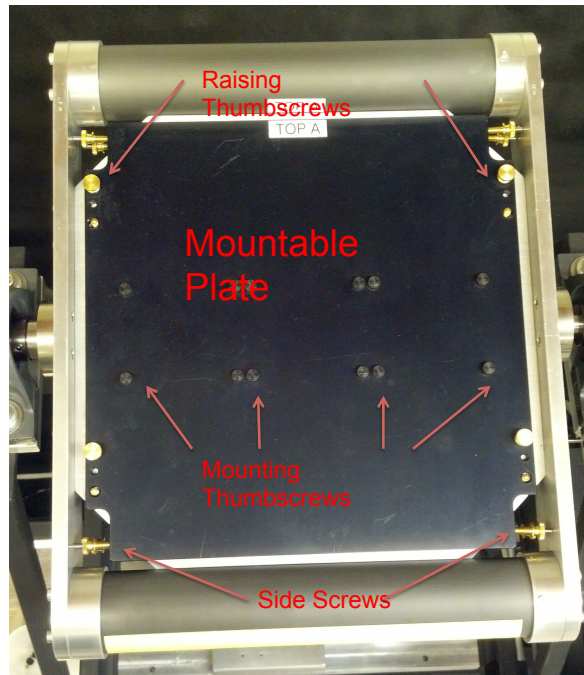


FIGURE B.5: The mountable plate, a part of the rotatable stage, is displayed here with its associated screws. Note allen head screws (4/40) work better than thumb screws shown because they don't interfere with the wire placement

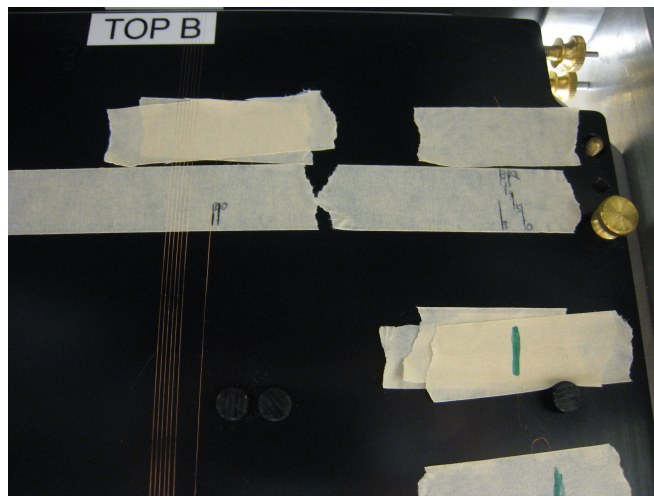


FIGURE B.6: Depiction of how the wire should be taped to the TOP B mountable plate

12. Remove the cover on the Mylar tape. This will help keep the wires in place as the rotatable stage rotates.
13. Use the WPM motor controller dial to adjust the motor to the desired speed (typically the 4th black tick mark) for wire winding. The speed need not be set to 4, but is left up to the discretion of the user since the Cat Whisker Despooler corrects for tension changes. The winder was typically operated at the 4th tick mark because the wire spool seemed to unwind consistently at this speed. Furthermore, if the plate is rotating too slowly, then you could get a double pulse in the photodiode and cause your spacing to be double the set value. Note that the first few rotations do not yield accurate spacing between the wires. To account for this, allow the wire to wind 2-4 times past the right most side of the active area.
14. After the desired wire winding is complete, use the motor controller dial to decelerate the rotatable stage until it is perpendicular with the floor. The label Top A should be visible on the rotatable stage. Set the WPM motor controller dial to 0.
15. Mix up some fast drying epoxy (typically Hardman Double Bubble Epoxy Extra Fast Setting) and dribble it on the curved edges of the rotatable plate. One should dribble the epoxy such that it covers the edged surface where the curved edge slopes into the groove. Fig. B.7 illustrates where the epoxy should be dribbled over the surface. The rotatable stage will need to be rotated such that each curved edge faces upward during this step. Sufficient time should also be given for the epoxy to dry before applying epoxy to the other curved edge. This layer of epoxy will affix the wires in place at the curved edges. This way one can detach excess wire from the ends of the printed circuit board on TOP A independent of the wires attached to the printed circuit board on TOP B. One detaches the excess wire in Step 21 when the wire plane on the printed circuit board is epoxied, and one is ready to remove the printed circuit board from the mountable plate.



FIGURE B.7: Red lines are drawn in to show where the epoxy should be dribbled onto the curved edge of the rotatable plate

16. Unscrew the 4 side screws, seen in Fig. B.5, into the mountable plate. Unscrew the 4 raising thumbscrews, also seen in Fig. B.5, and remove them from the mountable plate. Screw the raising thumbscrews into the holes adjacent to the holes where they were unscrewed from. This process will raise the mountable plate upwards. Raise the mountable plate until the wires sit just above the PCB. The wires should just begin to touch the PCB. You should be certain that the mountable plate is level at this point. Turn off the rotatable stage.
17. Use the side screws shown in Fig. B.5 to align the wires over the pads that will be soldered. First align the right side, then the left, and finally the middle. Tighten the side screws to keep the board in place after the wires are aligned.
18. Cut a Mylar sheet using the scribed aluminum template to make thin strips. The Mylar strips need to be long enough to cover the width of the wire plane. Mix Epon 828 Resin with Versamid 140 (70:30 w/w). To accomplish this use syringes to dispense the epoxy resin and curing agent into a weigh boat. I have found that a total mass of 3 grams works well for purpose. Apply the epoxy in a thin layer over 2 Mylar strips. Place a Kimwipe over where the active area of the wire harp will be. This will prevent any epoxy from dripping onto the active area of the wire harp. Place the Mylar strips over the wires on both ends of the PCB. Do not tap the Mylar strip as this could re-position the wires.

19. Place a Kimwipe over where the active area of the wire harp will be. This will prevent any solder flakes from sticking to the wires during the soldering step. I used 63/37 fine solder.
20. Verify that the wires are soldered to each pad by using a probe and the magnifier. It is recommended that each wire is checked at least three times.
21. Use an X-ACTO knife to cut the wires in order to separate the printed circuit board from the rotatable stage. The easiest way to do this is to hold the X-ACTO knife in place and use a probe to gently press the wire against the knife edge. Be careful not to push the knife too hard as this could damage the PCB. Unscrew the mounting thumbscrews and remove the PCB from the mountable plate.
22. Screw the 4 raising thumbscrews back so the mountable plate connects to the rotatable stage. Unscrew the 4 side screws away from the mountable plate so that the mountable plate cannot move from side to side.
23. Squirt flux remover over wire harp. Then squirt isopropanol over the wire harp to remove any solder flakes. Clean the wire harp thoroughly by squirting ethanol over the active area. Otherwise, a noticeable residue will be left behind by the isopropanol. Repeat as needed taking care not to apply any pressure to the wire harp.
24. Once the PCB has been removed from TOP A, perform Steps 16–23 on the other printed circuit board located on TOP B.
25. Dispose of the unused wire. Remove the tape from the rotatable stage and dispose of it. Remove any epoxy that adhered to the curved edges of the rotatable stage by using isopropanol and ethanol. Turn off the Neat-1 Controller, DC motor, and the power strip switch. Unplug the power strip from the outlet.

B.2 Troubleshooting the wire winder

1. Problem: The wire is oscillating at the point above the spool of wire and before the Cat Whisker Despooler.

Solution: If one is using a spool of wire that is not wound properly it can cause the wire to wiggle while it is being unspooled. This can lead to a misplacement of the wire on the table. In the event of this problem, the spool should be changed or the DC wpm motor speed should be lowered.

2. Problem: The uppermost lever arm, number (5) in Fig. B.4, undergoes a fast “scissoring motion” with the lever arm directly underneath.

Solution: The DC motor speed should be lowered. If lowering the speed doesn’t solve the problem, then the problem may be that the spool is not properly wound and the wire cannot be correctly unspooled. Also, it is important that the spool surrounds the rod concentrically, or the spool will not rotate uniformly.

3. Problem: The tension is not remaining constant in the wire.

Solution: The tension wheel, located on the backside of the Cat Whisker Despooler, cannot be adjusted to the highest or lowest tension setting or else it will skew the position of the pulleys. Set the tension wheel to somewhere in the middle tension range.

4. Problem: The Neat-1 Preset Indexer makes a creak, reminiscent of metal scraping metal, every time it steps. This is an indication that the lead screw and nut have become dirty. Wire placement error will result from a dirty lead screw and nut. This problem may also arise from lack of grease.

Solution: The threaded screw of the stepper motor should be thoroughly cleaned to rid it of excess grease and dirt. The threaded screw should then be re-greased

with a Triflow aerosol lubricant, or equivalent grease. If the sound persists, it may be that the bearings are failing or perhaps a particulate has been lodged in the bearings.

5. Problem: There is random, imprecise winding. This problem is not a result of Problem 2 or 4.

Solution: The wire can wear a groove into the white, Nylon piece immediately above the Preset Indexer. One should sand this down to rid the piece of grooves with 600 grade silicon carbide sandpaper.

Appendix C

Delay board characterization

It was necessary to characterize the delay boards for the simulations performed in Section 4.3. The goal was to measure the signal delay, dispersion, and attenuation as a function of delay board position. The electronic diagram for these measurements can be found in Fig. D.11. The first test was to measure the delay as a function of delay board position for both delay boards. The result is presented in Fig. C.1. The 1ns/tap delay boards has a total delay length ~ 58 ns, while the 0.5ns/tap delay boards have a total delay length of ~ 27 ns. The delay length has a linear relationship with position as expected.

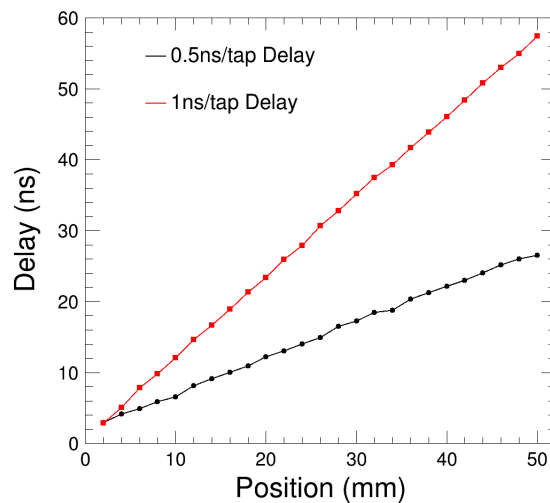


FIGURE C.1: Time delay as a function of delay board position for delay boards only.

A schematic for how the risetime was determined can be found in Fig. C.2. The following steps were used in determination of this risetime: 1) calculate the average height (H), 2) calculate 50% of H, record trace with Δ_{tb} and Δ_{tf} , calculate the maximum and minimum timing, and calculate $t_{10\%}$ and $t_{90\%}$. The result of the risetime measurements

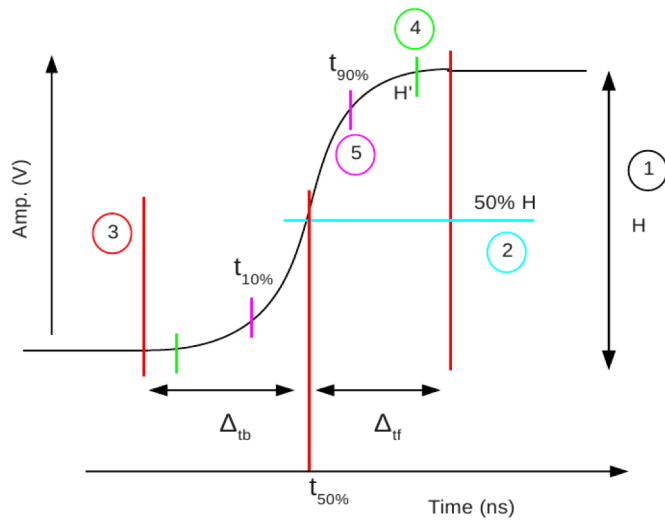


FIGURE C.2: Schematic for risetime determination in the delay board characterization.

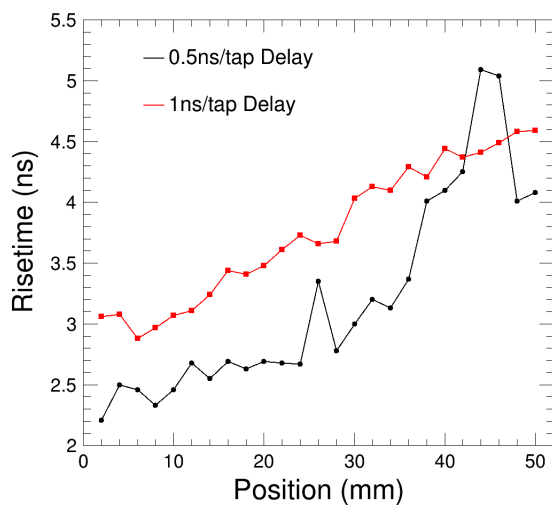


FIGURE C.3: Risetime as a function of delay board position for delay boards only.

for both delay boards are presented in Fig. C.3. The risetime varies from 3.5 ns to 4.6 ns for the 1 ns/tap delay board, while the risetime varies from 2.2 ns to 5.1 ns for the 0.5ns/tap delay board. The relationship is approximately linear in the case of the 1 ns/tap delay boards and it is roughly linear for the 0.5ns/tap delay board case. The 0.5ns/tap delay board risetimes do not seem to follow as systematic of a trend as the 1 ns/tap delay boards. The attenuation as a function of position for each delay board is presented in Fig. C.4. The attenuation factor, A_{out}/A_{inp} , for the 1ns/tap delay boards is a maximum of $\sim 33\%$, while the attenuation factor for the 0.5ns/tap delay boards is a maximum of $\sim 86\%$. The dependence of attenuation with position is approximately linear for each delay board.

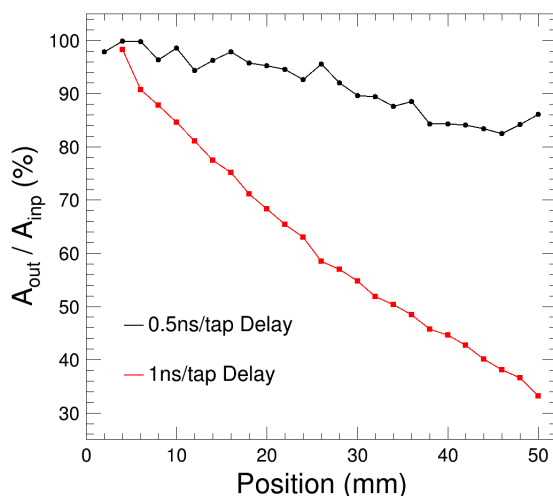


FIGURE C.4: Attenuation as a function of delay board position for delay boards only.

We then turned our attention towards measurements with the delay coupled to the SW board. The delay time dependence as a function of position is presented in Fig. C.5. This relationship remains largely unchanged from that previously measured case. The risetime distribution for each delay board position is presented in Fig. C.6. The risetime increases from ~ 2.6 to ~ 5.8 ns across the full length of the 1 ns/tap delay board, while the risetime increases from ~ 2.4 ns to ~ 6.2 ns for the 0.5 ns/tap delay boards. There

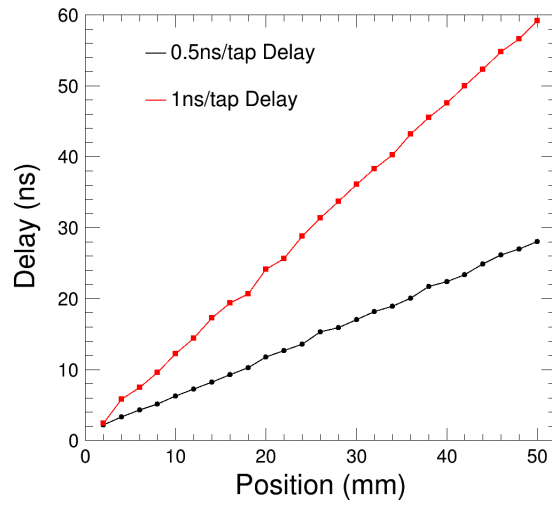


FIGURE C.5: Time delay as a function of delay board position for delay + SW boards.

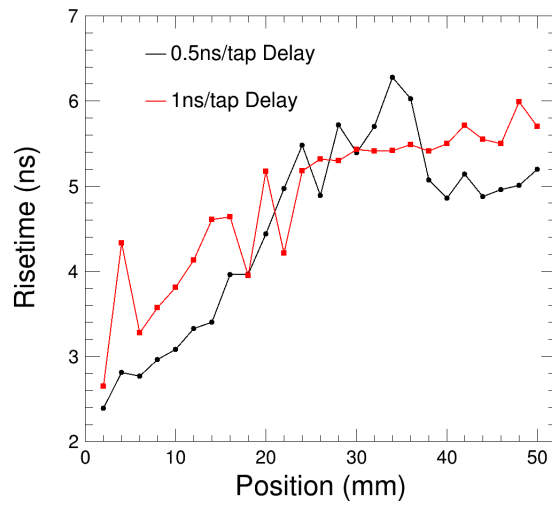


FIGURE C.6: Risetime as a function of delay board position for delay + SW boards.

is some strange non-linear dependence observed especially in the case of the 0.5 ns/tap delay boards. Furthermore, the inherent transition time of 3 to 4 ns of SW signals, when added to the 2.5 to 6 ns range risetimes, further solidifies that the variation in the transition time from 3 to 12 ns was caused by predominantly by the delay boards. The attenuation for each delay board position is presented in Fig. C.7. The total attenuation for the 1ns/tap delay boards is $\sim 33\%$, while the total attenuation for the 0.5ns/tap delay boards is $\sim 78\%$.

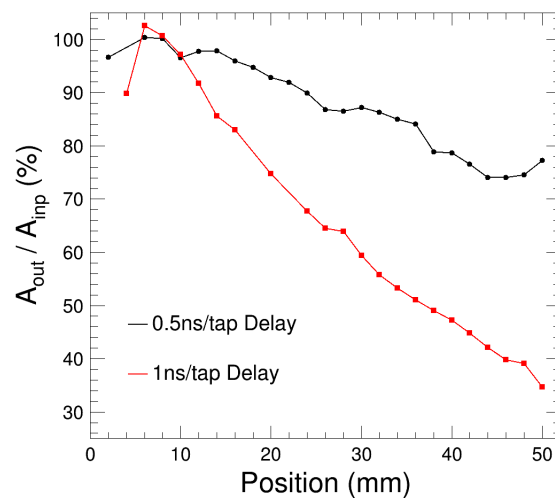


FIGURE C.7: Attenuation as a function of delay board position for delay + SW boards.

Appendix D

Electronics Diagrams

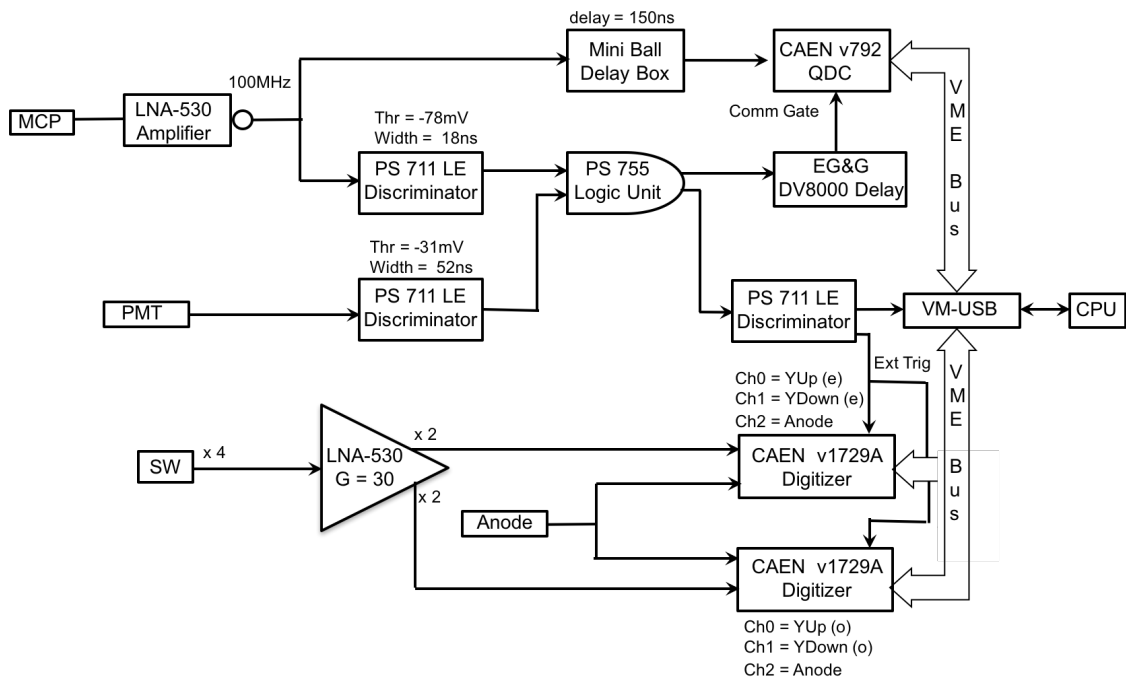


FIGURE D.1: Electronics diagram for work presented in Section 2.1.5.3.

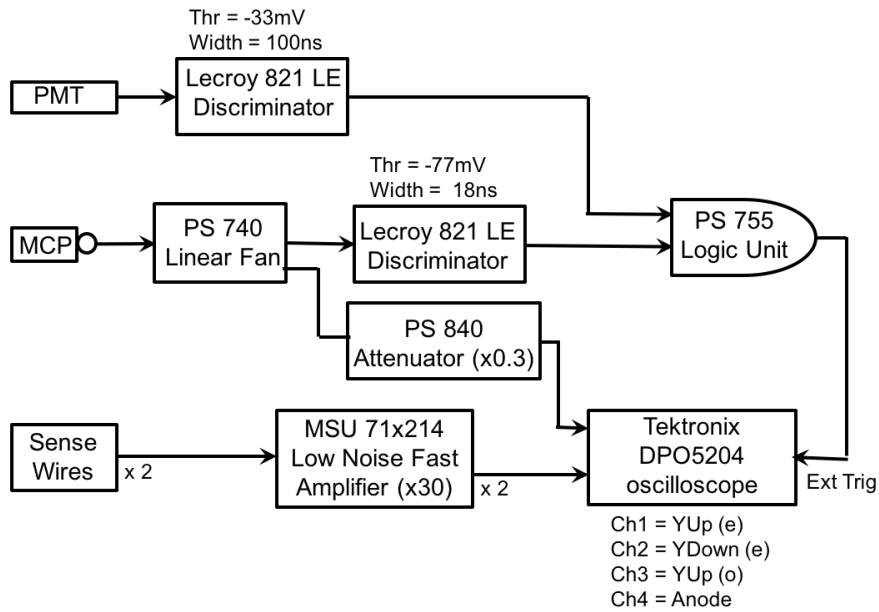


FIGURE D.2: Electronics diagram for work presented in Section 2.1.5.4.

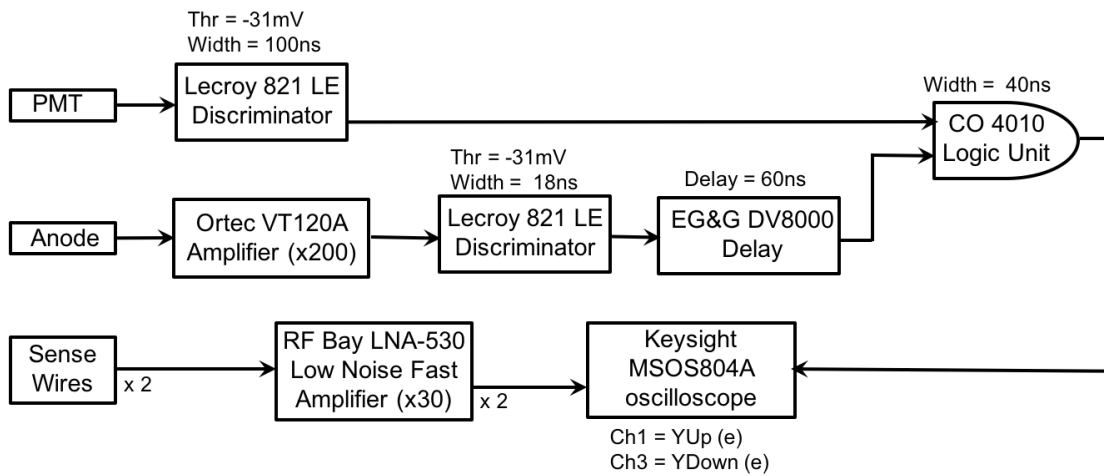


FIGURE D.3: Electronics diagram for work presented in Section 2.1.5.4.

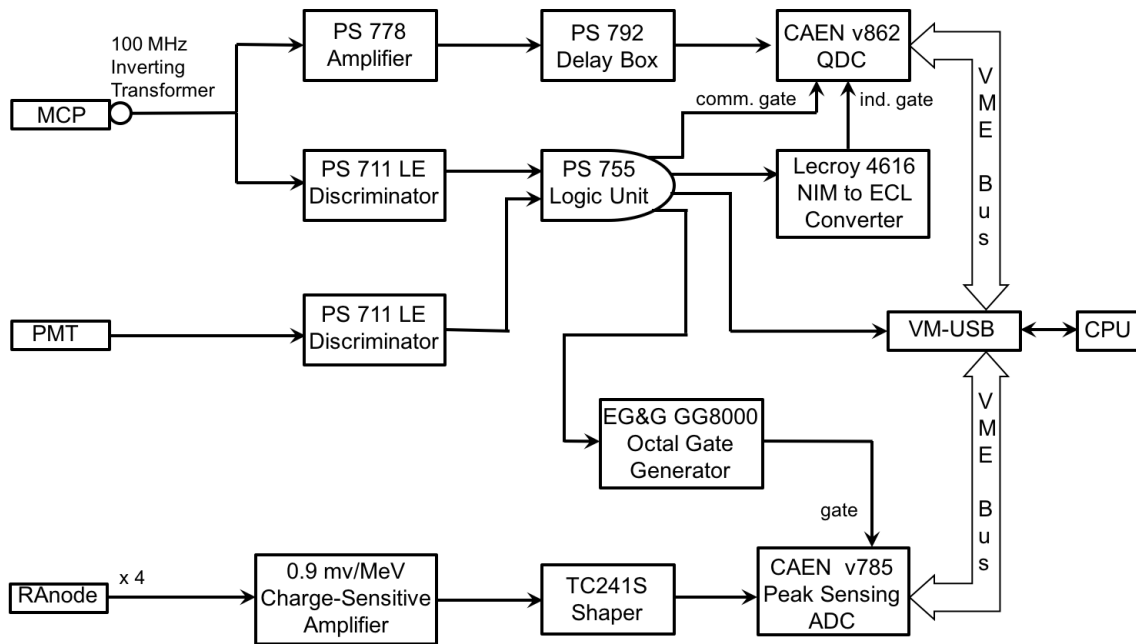


FIGURE D.4: Electronics diagram for work presented in Section 2.2.2.

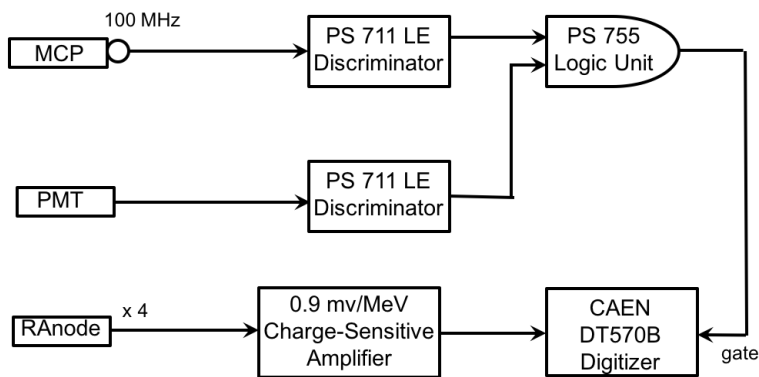


FIGURE D.5: Electronics diagram for work presented in Section 2.2.3.1.

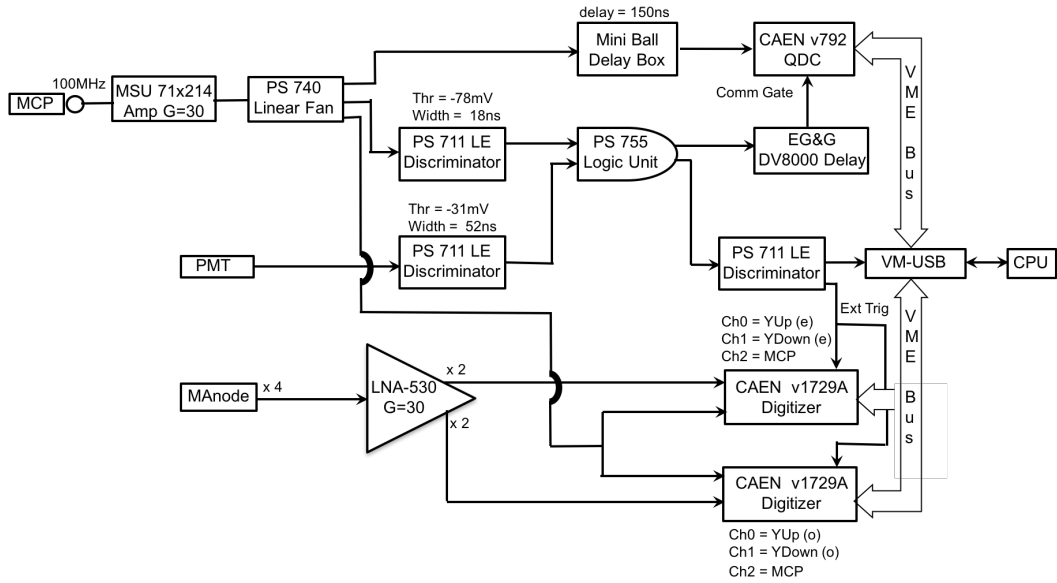


FIGURE D.6: Electronics diagram for work presented in Section 2.3.

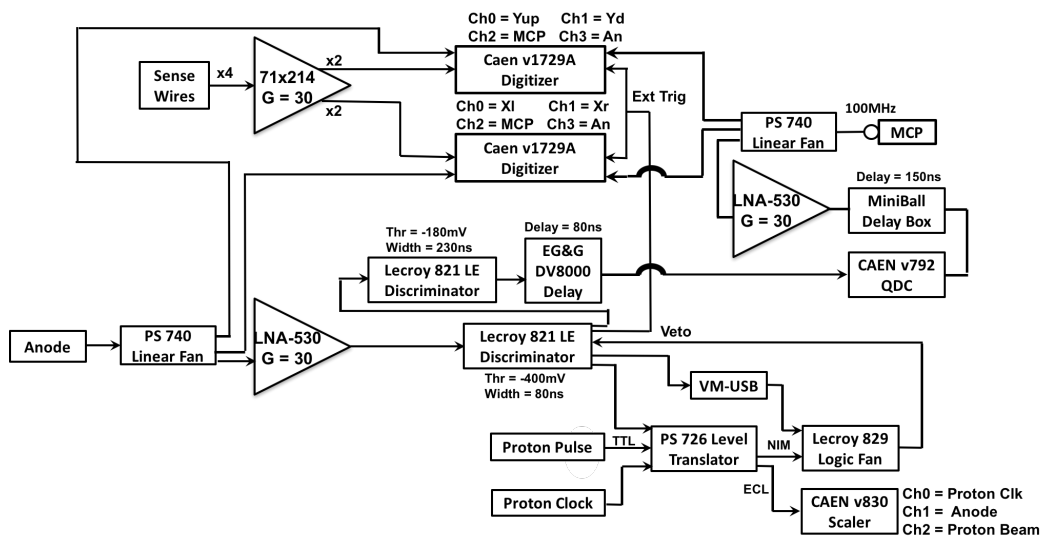


FIGURE D.7: Electronics diagram for work presented in Section 3.1.6.

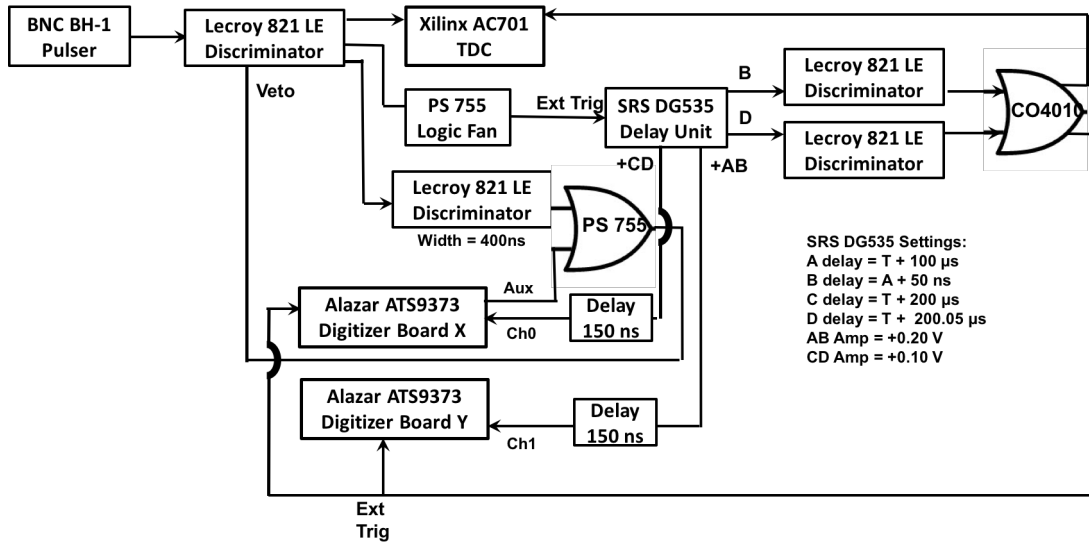


FIGURE D.8: Electronics diagram for work presented in Section 3.1.7.

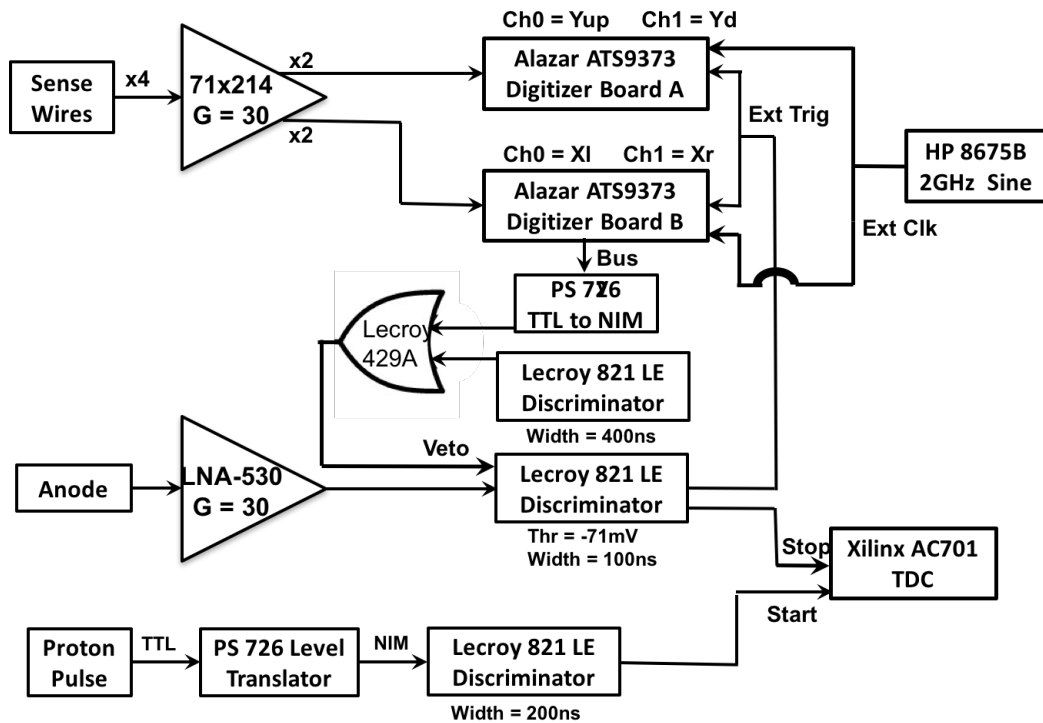


FIGURE D.9: Electronics diagram for work presented in Section 3.1.8.

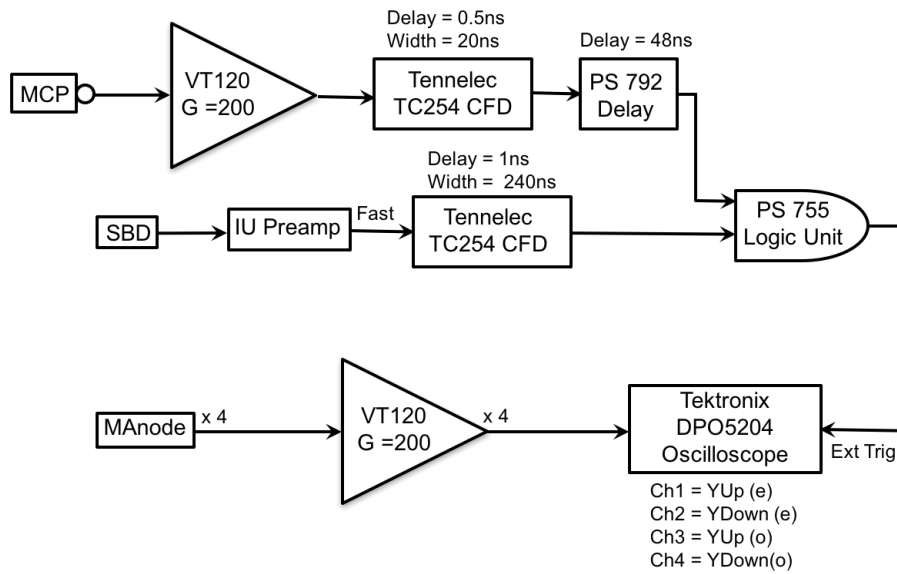


FIGURE D.10: Electronics diagram for work presented in Section 3.2.3.

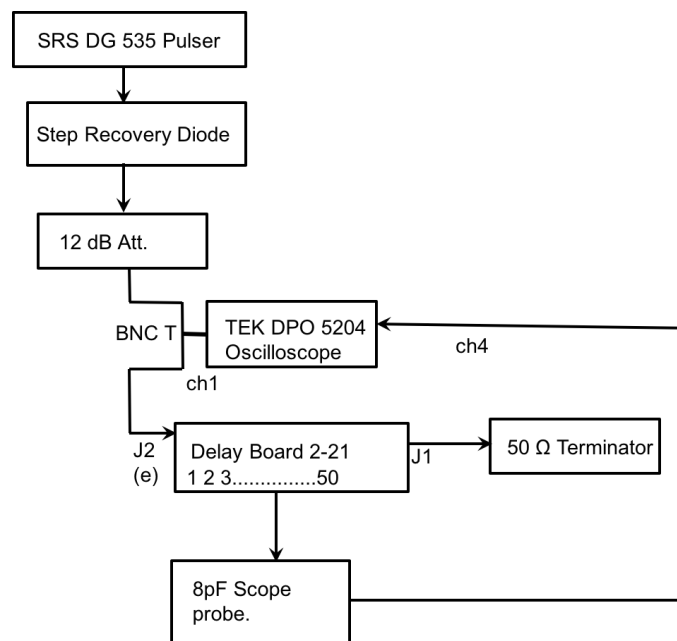


FIGURE D.11: Electronics diagram for work presented in Appendix C.

Appendix E

Program directories

- SW1D Analysis 2 GS/s
/nfshome/lucy/brywiggi/PSMCP/Analysis/SWDiff_Ana/
RawAnalyseReg.C
RawAnalyseReg.h
Makefile
- SW1D Analysis 10 GS/s 50 ns
/nfshome/calvin/brywiggi/PSMCP/Analysis/Ana_SW1D_10GHz/
Delay_1nspertap/CaseStructureMethod/
Analyze.C
Analyze.h
Makefile
- SW1D Analysis 10 GS/s 25 ns
/nfshome/calvin/brywiggi/PSMCP/Analysis/Ana_SW1D_10GHz/
Delay_pt5nspertap/LNA530Amp/
Analyze.C
Analyze.h
Makefile
- SW1D Analysis 20 GS/s
/nfshome/calvin/brywiggi/PSMCP/Analysis/Ana_SW1D_20GHz/

Analyze.C

Analyze.h

Makefile

- RA DSP analysis

/nfshome/woodstock/dsiwal/OrganizedCodes/StandaloneDSPCode/

digitalshapers.cpp

digitalshapers.h

pulsetobinary.cpp

gauss.setup

trapz.setup

Makefile

- MAnode analysis

/nfshome/lucy/brywiggi/PSMCP/Analysis/MAnode_Ana/

RawAnalyseReg.C

RawAnalyseReg.h

Makefile

- NRad Dec16 analysis online and offline

/nfshome/calvin/brywiggi/PSMCP/Analysis/Ana_NRad/

OnlineAnalysis_Dec16/

RawAnalyse_SH.C

RawAnalyse.h

fileList.txt

Makefile

/nfshome/calvin/brywiggi/PSMCP/Analysis/Ana_NRad/OfflineAnalysis/

RawAnalyse_SH.C

RawAnalyse.h

fileList.txt

Makefile

- NRad June17 analysis online and offline

/nfshome/calvin/brywiggi/PSMCP/Analysis/Ana_NRad/

ATS9373_Digitizer_June17Expt/

Analyze.C

Analyze.h

Makefile

/nfshome/calvin/brywiggi/PSMCP/Analysis/Ana_NRad/

OfflineAnalysis_June17Expt/

Analyze.C

Analyze.h

Makefile

- E×B analysis

/nfshome/lucy/brywiggi/PSMCP/Analysis/DSMCP_with_MAnode/

Differential_Readout/CFDProcessing_Source_241Am_10uCi_4000VGrid/

RawAnalyseReg.C

RawAnalyseReg.h

Makefile

- Electron cloud growth calculations

/nfshome/woodstock/dsiwal/OrganizedCodes/ChargeCloudRadius/
eCloudRadius.cpp

Makefile

- Electron cloud pore calculations

/data/f1/Backups/From_12/PSMCP/Simulation/MCP_Stack_Sim/

McpStackSimBase.C

McpStackSimBase.h

OnePoreOverlap.C

OnePoreOverlap.h

TwoPoreOverlap.C

TwoPoreOverlap.h

ThreePoreOverlap.C

ThreePoreOverlap.h

- $E \times B$ SIMION results

/nfshome/tournesol/brywiggi/Papers/NIM17_DSMCP/Plot/

Plot_YPos_2Panel.C

Plot_FinalPositionSIMION.C

- $E \times B$ mapping B Field

/nfshome/tournesol/brywiggi/Papers/NIM17_DSMCP/Plot/

Post_Submission_Plots/

By_plot_TH3F_measured.C

- SW1D simulations

/nfshome/garfield/undergrad/Zarya/

SWSimSignal_2.C

Analyze.h

Makefile

- Delay board calculations

/nfshome/woodstock/dsiwal/OrganizedCodes/

DelayAndGridBoardCharactCode/

dispersion.C

- RAQ paper + figures

/nfshome/tournesol/desouza/FromLute/desouza/2dmcp/RSI_RA/

rsi_ra.tex

/nfshome/lucy/brywiggi/PSMCP/Figures/Rev_Sci_Instrum_2015_Paper/

MCP_PulseHeightDistribution.C

Raw2D.C

Qtot_vs_Qmcp.C

/nfshome/lucy/brywiggi/PSMCP/Analysis/ResolutionvsMCP-RADist/

Resolution_vs_Distance_WithInset.C

FWHM_deltaV_Qmcp_2panel.C

radiusvstime.C

/nfshome/woodstock/dsiwal/MCPsim/resultsv6/summing.C

- RADSP Paper + figures

/nfshome/tournesol/desouza/FromLute/desouza/Pulse_Shape_MCP
pulse_shape_MCP.tex

/nfshome/woodstock/dsiwal/RiseTimeNIM/files_Used_for_NIMpaper/
figures.C
FWHM_vs_Slitno_v2.C

- E×B Paper + figures

/nfshome/garfield/desouza/NIM17_PS_DSMCP/

/nfshome/tournesol/brywiggi/Papers/NIM17_DSMCP/Plot/
Post_Submission_Plots/
PlotTCorrelrev.C
PlotPositionrev.C
FWHM_vs_YPosition.C
PlotSlitwithIntrRsrev.C
By_plot_TH3F_measured.C
Plot_YPosSim_2Panelrev.C
Plot_FinalPositionSIMIONrev.C

- SW1D Paper + figures

/nfshome/garfield/desouza/SenseWires1D/

SW1D_NIM.tex

/nfshome/calvin/brywiggi/PSMCP/Papers/SenseWires1D_NIM17/Macros/

Plot_MCPChargepC.C

Plot_YPosition.C

Plot_YPosition_Raw.C

/nfshome/tournesol/undergrad/Zarya/FFT_Code_only/

ResolutionPlotMacro.C

Bibliography

- [1] R. T. deSouza, Z. Q. Gosser, and S. Hudan. Using induced signals to sense position from a microchannel plate detector. *Rev. Sci. Instrum.*, 83:053305, 2012.
- [2] R. T. deSouza, B. B. Wiggins, and D. Siwal. Sensing an electron cloud emanating from a microchannel plate stack. *IEEE Nucl. Sci. Symp. Med. Imaging Conf.*, page 4018747, 2015.
- [3] 2017. URL <https://www.hamamatsu.com/eu/en/index.html>.
- [4] 2017. URL <http://www.photonis.com/>.
- [5] ArraySL-4-30035-CER, 2017. URL <http://sens1.com>.
- [6] P. Buzhan, B. Dolgoshein, A. Ilyin, V. Kaplin, S. Klemin, R. Mirzoyan, E. Popova, and M. Teshima. The cross-talk problem in SiPMs and their use as light sensors for imaging atmospheric Cherenkov telescopes. *Nucl. Instr. Meth. Phys. Res. A*, 610: 131–134, 2009.
- [7] J. L. Wiza. Microchannel plate detectors. *Nucl. Instr. Meth. Phys. Res.*, 162: 587–601, 1979.
- [8] P. Schagen. Image tubes with channel electron multiplication. *Advances in image pick-up and display*, 1:1–69, 1974.
- [9] A. S. Tremsin, W. B. Feller, and R. G. Downing. Efficiency optimization of microchannel plate (MCP) neutron imaging detectors. I. Square channels with ^{10}B doping. *Nucl. Instr. Meth. Phys. Res. A*, 539:278–311, 2005.

- [10] W. J. Williams. Neutron radiography and tomography: Determining and optimizing resolution of neutron sensitive multi channel plate detectors. Master's thesis, Oregon State University, 2013.
- [11] Hamamatsu Photonics K. K. *Photomultiplier Tubes Basics and Applications*. 3rd edition, 2007.
- [12] Del mar photonics, inc., 2017. URL http://www.dmphotronics.com/MCP_MCPImageIntensifiers/microchannel_plates.htm.
- [13] Corning 8161 glass, 1960. US Patent 2, 964, 414.
- [14] T. Mizogawa, M. Sato, M. Yoshino, Y. Itoh, and Y. Awaya. A two-dimensional position-sensitive anode for microchannel plates based on the "MBWC" technique. *Nucl. Instr. Meth. Phys. Res. A*, 387:395–400, 1997.
- [15] M. Lampton. The microchannel image intensifier. *Sci. Am.*, 245:62–71, 1981.
- [16] S. A. Watson. The DARHT camera. *Los Alamos Science*, 28:92–95, 2003.
- [17] National Research Council. Evaluating testing, costs, and benefits of advanced spectroscopic portals for screening cargo at ports of entry: Interim report(abbreviated version). 2009.
- [18] A. S. Tremsin, J. B. McPhate, J. V. Vallerga, O. H. W. Siegmund, W. B. Feller, E. Lehmann, L. G. Butler, and M. Dawson. High-resolution neutron microtomography with noiseless neutron counting detector. *Nucl. Instr. Meth. Phys. Res. A*, 652:400–403, 2011.
- [19] O. Jagutzki, V. Dangendorf, R. Lauck, A. Czasch, and J. Milnes. A position- and time-sensitive photon-counting detector with delay- line read-out. *Proc. SPIE*, 6585: 65851C, 2007.

- [20] D. Shapira, T. A. Lewis, and L. D. Hulett. A fast and accurate position-sensitive timing detector based on secondary electron emission. *Nucl. Instr. Meth. Phys. Res. A*, 454:409–420, 2000.
- [21] B. B. Wiggins, Varinderjit Singh, J. Vadas, J. Huston, T. K. Steinbach, S. Hudan, and R. T. deSouza. Development of a compact $E \times B$ microchannel plate detector for beam imaging. *Nucl. Instr. Meth. Phys. Res. A*, 866:202–206, 2017.
- [22] K. Inami, T. Mori, T. Matsumura, K. Kurimoto, S. Hasegawa, Y. Suzuki, T. Murase, Y. Yurikusa, M. Akatsu, Y. Enari, T. Hokuue, A. Tomita, N. Kishimoto, T. Ohshima, T. Ihara, and H. Nishizawa. Cross-talk suppressed multi-anode MCP-PMT. *Nucl. Instr. Meth. Phys. Res. A*, 592:247–253, 2008.
- [23] W.-S. Choong. Investigation of a multi-anode microchannel plate PMT for time-of-flight PET. *IEEE Trans. Nucl. Sci.*, 57:2417–2423, 2010.
- [24] W. Becker. Advanced time-correlated single photon counting techniques. *Springer Series in Chemical Physics*, 81, 2005.
- [25] L. Renaud, G. Da Costa, M. Bouet, and B. Deconihout. Design of a fast multi-hit position sensitive detector based on a CCD camera. *Nucl. Instr. Meth. Phys. Res. A*, 477:150–154, 2002.
- [26] S. Eliseev, K. Blaum, M. Block, C. Droese, M. Goncharov, E. Minaya Ramirez, D. A. Nesterenko, Yu. N. Novikov, and L. Schweikhard. Phase-Imaging Ion-Cyclotron-Resonance measurements for short-lived nuclides. *Phys. Rev. Lett.*, 110:082501, 2013.
- [27] F. Österdahl, S. Rosén, V. Bednarska, A. Petrignani, F. Hellberg, M. Larsson, and W. J. van der Zande. Position- and time-sensitive coincident detection of fragments from the dissociative recombination of O_2^+ using a single hexanode delay-line detector. *J. Phys. Conf. Ser.*, 4:286–289, 2005.

- [28] V. Emiliani, D. Sanvitto, M. Tramier, T. Piolot, Z. Petrasek, K. Kemnitz, C. Durieux, and M. Coppey-Moisan. Low-intensity two-dimensional imaging of fluorescence lifetimes in living cells. *Appl. Phys. Lett.*, 83:2471–2473, 2003.
- [29] W. E. Byrne, C-W. Chiu, J-H. Guo, F. Sannibale, J. S. Hull, O. H. W. Siegmund, A. S. Tremsin, and J. V. Vallerga. Bunch diffusion measurements at the advanced light source. *Proceedings of European Particle Accelerator Conference, EPAC'06, Edinburgh*, page THPLS079, June 2006.
- [30] X. Michalet, R. A. Colyer, J. Antelman, O. H. W. Siegmund, A. Tremsin, J. V. Vallerga, and S. Weiss. Single-quantum dot imaging with a photon counting camera. *Curr. Pharm. Biotechnol.*, 10:543–558, 2009.
- [31] M. B. Williams, S. E. Sobottka, and J. A. Shepherd. Delay line readout of microchannel plates in a prototype position-sensitive photomultiplier tube. *Nucl. Instr. Meth. Phys. Res. A*, 302:105–112, 1991.
- [32] I. Yoshikawa, A. Yamazaki, G. Murakami, K. Yoshioka, S. Kameda, F. Ezawa, T. Toyota, W. Miyake, M. Taguchi, M. Kikuchi, and M. Nakamura. Telescope of extreme ultraviolet (TEX) onboard SELENE: science from the moon. *Earth Planets Space*, 60:407–416, 2008.
- [33] D. C. Barbacci, D. H. Russell, J. A. Schultz, J. Holocek, S. Ulrich, W. Burton, and M. Van Stipdonk. Multi-anode detection in electrospray ionization time-of-flight mass spectrometry. *J. Am. Soc. Mass Spectrom.*, 9:1328–1333, 1998.
- [34] Y. He, J. F. Poehlman, A. W. Alexander, K. Boraas, and J. P. Reilly. One hundred anode microchannel plate ion detector. *Rev. Sci. Instrum.*, 82:085106, 2011.
- [35] C. G. Enke, S. J. Ray, A. W. Graham, E. A. Dennis, G. M. Hieftje, A. J. Carado, C. J. Barinaga, and D. W. Koppenaal. Distance-of-flight mass spectrometry: A new

- paradigm for mass separation and detection. *Annu. Rev. Anal. Chem.*, 5:487–504, 2012.
- [36] Quantar Technology, Inc, 2017. URL <http://www.quantar.com/>.
- [37] RoentDek – Handels GmbH, 2017. URL <http://www.roentdek.com/>.
- [38] Sensor Sciences, LLC, 2017. URL <http://sensorsciences.com/>.
- [39] X-Spectrum, 2017. URL <http://www.x-spectrum.de/>.
- [40] G. W. Fraser. X- and γ -ray imaging using microchannel plates. *Nucl. Instr. Meth. Phys. Res.*, 221:115–130, 1984.
- [41] O. Siegmund, A. Tremsin, J. Vallerga, and J. McPhate. Microchannel plate cross-strip detectors with high spatial and temporal resolution. *Nucl. Instr. Meth. Phys. Res. A*, 610:118–122, 2009.
- [42] M. Lampton and C. W. Carlson. Low-distortion resistive anodes for two-dimensional position-sensitive MCP systems. *Rev. Sci. Instrum.*, 50:1093–1097, 1979.
- [43] B. B. Wiggins, E. Richardson, D. Siwal, S. Hudan, and R. T. deSouza. Optimizing the position resolution of a z-stack microchannel plate resistive anode detector for low intensity signals. *Rev. Sci. Instrum.*, 86:083303, 2015.
- [44] D. Siwal, B. B. Wiggins, and R. T. deSouza. Using pulse shape analysis to improve the position resolution of a resistive anode microchannel plate detector. *Nucl. Instrum. and Meth. A*, 804:144–148, 2015.
- [45] X. Llopart, M. Campbell, D. San Segundo, E. Pernigotti, and R. Dinapoli. Medipix2, a 64k pixel read out chip with 55 μm square elements working in single photon counting mode. *IEEE Trans. Nucl. Sci.*, 49:2279–2283, 2002.

- [46] R. Hong, A. Leredde, Y. Bagdasarova, X. Fléchar, A. García, M. Kossin, M. G. Sternberg, H. E. Swanson, and D. W. Zumwalt. High accuracy position response calibration method for a micro-channel plate ion detector. *Nucl. instrum. and Meth. A*, 835:42–50, 2016.
- [47] A. S. Tremsin. High resolution particle counting detectors with microchannel plates and their applications in materials research, astrophysics, biomedical imaging and synchrotron instrumentation, LBL Instrumentation Colloquium, 2016.
- [48] P. Downie, D. Litchfield, R. Parsons, D. J. Reynolds, and I. Powis. High-resolution position-sensing resistive anode microchannel plate detector systems suitable for megahertz count-rates. *Meas. Sci. Technol.*, 4:1293–1296, 1993.
- [49] J. G. Timothy. The development and test of multi-anode microchannel array detector systems II. Soft X-Ray detectors. *Progress Report for NASA Grant NAG5-622 for the period 1*, 1986.
- [50] Quantar Technology, 3300 series open-face MCP/RAE sensors, installation and maintenance manual, 2013.
- [51] C. Firmani, E. Ruiz, C. W. Carlson, M. Lampton, and F. Paresce. High-resolution imaging with a two-dimensional resistive anode photon counter. *Rev. Sci. Instrum.*, 53:570–574, 1982.
- [52] R. F. Floryan and C. B. Johnson. Resistive anode photomultiplier tube optimum operating conditions for photon correlation experiments. *Rev. Sci. Instrum.*, 60:339–343, 1989.
- [53] G. Murakami, K. Yoshioka, and I. Yoshikawa. High-resolution imaging detector using five microchannel plates and a resistive anode encoder. *Appl. Opt.*, 49:2985–2993, 2010.

- [54] M. Campbell. 10 years of the medipix2 collaboration. *Nucl. Instr. Meth. Phys. Res. A*, 633:S1–S10, 2011.
- [55] O. Jagutzki, V. Mergel, K. Ullmann-Pfleger, L. Spielberger, U. Spillman, R. Dörner, and H. Schmidt-Böcking. A broad-application microchannel-plate detector system for advanced particle or photon detection tasks: large area imaging, precise multi-hit timing information and high detection rate. *Nucl. Instr. Meth. Phys. Res. A*, 477:244–249, 2002.
- [56] G. Charpak, R. Bouclier, T. Bressani, J. Favier, and Č. Zupančič. The use of multiwire proportional counters to select and localize charged particles. *Nucl. Instr. Meth. Phys. Res.*, 62:262–268, 1968.
- [57] G. Charpak and F. Sauli. The multistep avalanche chamber: A new high-rate, high-accuracy gaseous detector. *Phys. Lett.*, 78:523–528, 1978.
- [58] The Nobel Prize in Physics 1992, 2017. URL https://www.nobelprize.org/nobel_prizes/physics/laureates/1992/.
- [59] T. A. Bredeweg. *Heavy-Ion-Induced Ternary Fission as a Probe of the Dynamical Decay of Excited Nuclei*. PhD thesis, Indiana University, 2001.
- [60] Molecular Photonics Group, 2017. URL <http://faculty.chem.queensu.ca/people/faculty/stolow/Research/Facilities.html>.
- [61] Z. Gosser. Using induced signals to sense position with a microchannel plate detector. Master’s thesis, Indiana University, 2012.
- [62] H. Rothard, K. O. Groeneveld, and J. Kemmler. *Particle Induced Electron Emission Part II*. Springer, 1992.

- [63] J. Villette, M. Barat, and P. Roncin. Calibration of a multiple microchannel plate detectors system by α -induced secondary electrons. *Rev. Sci. Instrum.*, 71:2367–2370, 2000.
- [64] Potomac Photonics, 2017. URL <http://www.potomac-laser.com>.
- [65] T. H. Hoenderken, C. W. Hagen, J. E. Barth, P. Kruit, and G. O. Nützel. Influence of the microchannel plate and anode gap parameters on the spatial resolution of an image intensifier. *J. Vac. Sci. Technol. B*, 19:843–850, 2001.
- [66] J. L. Wiza, P. R. Henkel, and R. L. Roy. Improved microchannel plate performance with a resistive anode encoder. *Rev. Sci. Instrum.*, 48:1217–1218, 1977.
- [67] B. Davin, R. T. deSouza, R. Yanez, Y. Larochelle, R. Alfaro, H. S. Xu, A. Alexander, K. Bastin, L. Beaulieu, J. Dorsett, G. Fleener, L. Gelovani, T. Lefort, J. Poehlman, R. J. Charity, L. G. Sobotka, J. Elson, A. Wagner, T. X. Liu, X.D. Liu, W. G. Lynch, L. Morris, R. Shomin, W. P. Tan, M. B. Tsang, G. Verde, and J. Yurkon. Lassa: a large area silicon strip array for isotopic identification of charged particles. *Nucl. Instr. Meth. Phys. Res. A*, 473:302–318, 2001.
- [68] CAEN Technologies, Inc, 2017. URL <http://www.caen.it>.
- [69] S. Kalbitzer and W. Melzer. On the charge dividing mechanism in position sensitive detectors. *Nucl. Instr. Meth.*, 56:301–304, 1967.
- [70] R. Brun and F. Rademakers. ROOT – an object oriented data analysis framework. *Nucl. Instr. Meth. Phys. Res. A*, 389:81–86, 1997.
- [71] S. W. Smith. *The Scientist and Engineer’s Guide to Digital Signal Processing*. California Technical Pub, 1997.

- [72] T. Kihm, V. F. Bobrakov, and H. V. Klapdor-Kleingrothaus. A digital multi-channel spectroscopy system with 100 MHz flash adc module for the GENIUS-TF and GENIUS projects. *Nucl. Instr. Meth. Phys. Res. A*, 498:334–339, 2003.
- [73] F. Dietrich, J. Hall, and C. Logan. Conceptual design for a neutron imaging system for thick target analysis operating in the 10–15 MeV energy range. *AIP Conference Proceedings*, 392:837, 1997.
- [74] J. Zhang, D. Kramer, R. Shimoi, Y. Ono, E. Lehmann, A. Wokaun, K. Shinohara, and G. G. Scherer. In situ diagnostic of two-phase flow phenomena in polymer electrolyte fuel cells by neutron imaging Part B. material variations. *Electrochim. Acta*, 51:2715–2727, 2006.
- [75] K. J. Coakley, D. F. Vecchia, D. S. Hussey, and D. L. Jacobson. Neutron tomography of a fuel cell: Statistical learning implementation of a penalized likelihood method. *IEEE Trans. Nucl. Sci.*, 60:3945–3954, 2013.
- [76] X. Liu, T. A. Trabold, J. J. Gagliardo, D. L. Jacobson, and D. S. Hussey. Neutron imaging of water accumulation in the active area and channel-to-manifold transitions of a PEMFC. *Proc. ASME 11th Fuel Cell Science*, page V001T01A010, 2014.
- [77] K. Iwase, H. Sato, S. Harjo, T. Kamiyama, T. Ito, S. Takata, K. Aizawa, and Y. Kiyonagi. In situ lattice strain mapping during tensile loading using the neutron transmission and diffraction methods. *J. Appl. Cryst.*, 45:113–118, 2012.
- [78] Y. Kiyonagi, T. Kamiyama, K. Kino, H. Sato, S. Sato, and S. Uno. Pulsed neutron imaging using 2-dimensional position sensitive detectors. *J. Instrum.*, 9:C07012, 2014.
- [79] B. Abbey, S. Y. Zhang, W. Vorster, and A. M. Korsunsky. Reconstruction of axisymmetric strain distributions via neutron strain tomography. *Nucl. Instr. Meth. Phys. Res. B*, 270:28–35, 2012.

- [80] G. Chen and R. C. Lanza. Fast neutron resonance radiography for elemental imaging: theory and applications. *IEEE Trans. Nucl. Sci.*, 49:1919–1924, 2002.
- [81] N. Kardjilov, E. Lehmann, E. Steichele, and P. Vontobel. Phase-contrast radiography with a polychromatic neutron beam. *Nucl. Instrum. Meth. Phys. Res. A*, 527:519–530, 2004.
- [82] F. Pfeiffer, C. Grünzweig, O. Bunk, G. Frei, E. Lehmann, and C. David. Neutron phase imaging and tomography. *Phys. Rev. Lett.*, 96:215505, 2006.
- [83] M. Strobl, N. Kardjilov, A. Hilger, E. Jericha, G. Badurek, and I. Manke. Imaging with polarized neutrons. *Physica B*, 404:2611–2614, 2009.
- [84] M. Strobl, A. S. Tremsin, A. Hilger, F. Wieder, N. Kardjilov, I. Manke, W. G. Bouwman, and J. Plomp. TOF-SEMSANS Time-of-flight spin-echo modulated small-angle neutron scattering. *J. Appl. Phys.*, 112:014503, 2012.
- [85] T. C. Grünzweig, J. Kopecek, B. Betz, A. Kaestner, K. Jefimovs, J. Kohlbrecher, U. Gasser, O. Bunk, C. David, E. Lehmann, T. Donath, and F. Pfeiffer. Quantification of the neutron dark-field imaging signal in grating interferometry. *Phys. Rev. B*, 88:125104, 2013.
- [86] I. Manke, N. Kardjilov, R. Schäfer, A. Hilger, M. Strobl, M. Dawson, C. Grünzweig, G. Behr, M. Hentschel, C. David, A. Kupsch, A. Lange, and J. Banhart. Three-dimensional imaging of magnetic domains. *Nat. Comm.*, 1:171–179, 2010.
- [87] T. Wang, S. R. Parnell, W. A. Hamilton, H. Kaiser, A. L. Washington, D. V. Baxter, and R. Pynn. Neutron spin manipulation devices using YBCO films. *J. Phys. Conf. Ser.*, 528:012024, 2014.
- [88] R. Gahler, R. Golub, and T. Keller. Neutron resonance spin echo— a new tool for high resolution spectroscopy. *Physica B*, 180&181:899–902, 1992.

- [89] D. V. Baxter, J. Leung, Helmut Kaiser, S. Ansell, G. Muhrer, E. B. Iverson, and P. D. Fergusson. Neutron moderator development research at the low energy neutron source. *Phys. Proc.*, 26:117–123, 2012.
- [90] E. B. Iverson, D. V. Baxter, G. Muhrer, S. Ansell, R. Dalglish, F. X. Gallmeier, H. Kaiser, and W. Lu. Enhancing neutron beam production with a convoluted moderator. *Nucl. Instr. Meth. Phys. Res. A*, 762:31–41, 2014.
- [91] F. Li, S. R. Parnell, W. A. Hamilton, B. B. Maranville, T. Wang, R. Semerad, D. V. Baxter, J. T. Cremer, and R. Pynn. Superconducting magnetic Wollaston prism for neutron spin encoding. *Rev. Sci. Instrum.*, 85:053303, 2014.
- [92] Surface Concept, Imaging neutron detection with time resolution, 2017. URL <http://surface-concept.com/>.
- [93] S. D. Pinto, R. Ortega, S. Ritzau, D. Pasquale, B. Laprade, S. Mrotek, S. Gardell, Z. Zhou, J. Plomp, L. van Eijck, H. Bilheux, and I. Dhiman. Neutron imaging and tomography with MCPs. *arXiv:1710.02614 [physics.ins-det]*, 2017.
- [94] E. H. Lehmann, G. Frei, G. Kühne, and P. Boillat. The micro-setup for neutron imaging: A major step forward to improve the spatial resolution. *Nucl. Instr. Meth. Phys. Res. A*, 576:389, 2007.
- [95] A. S. Tremsin, J. V. Vallergha, J. B. McPhate, O. H. W. Siegmund, W. B. Feller, L. Crow, and R. G. Cooper. On the possibility to image thermal and cold neutron with sub-15 μm spatial resolution. *Nucl. Instr. and Meth. A*, 592:374–384, 2008.
- [96] W. B. Feller. Neutron and photon detector workshop MCP detector development, Nova Scientific, Inc., 2012.
- [97] J. F. Ziegler, M. D. Ziegler, and J. P. Biersack. SRIM – The stopping and range of ions in matter (2010). *Nucl. Instr. Meth. Phys. Res. B*, 268:1818–1823, 2010.

- [98] NOVA Scientific, Inc., 2017. URL <http://www.novascientific.com/>.
- [99] D. V. Baxter, J. M. Cameron, M. B. Leuschner, H. O. Meyer, H. Nann, and W. M. Snow. LENS—a pulsed neutron source for education and research. *Nucl. Instr. Meth. Phys. Res. A*, 542:28–31, 2005.
- [100] C. M. Lavelle, D. V. Baxter, A. Bogdanov, V. P. Derenchuk, H. Kaiser, M. B. Leuschner, M. A. Lone, W. Lozowski, H. Nann, B.v. Przewoski, N. Remmes, T. Rinckel, Y. Shin, W. M. Snow, and P. E. Sokol. Neutronic design and measured performance of the low energy neutron source target moderator reflector assembly. *Nucl. Instr. Meth. Phys. Res. A*, 587:324–341, 2008.
- [101] D. V. Baxter, S. Aldaihan, S. R. Parnell, R. Pynn, P. E. Sokol, W. M. Snow, and T. Rinckel. LENS: 2013 facility overview. *Phys. Proc.*, 60:175–180, 2014.
- [102] M. Strobl, I. Manke, N. Kardjilov, A. Hilger, M. Dawson, and J. Banhart. Advances in neutron radiography and tomography. *J. Phys. D: Appl. Phys.*, 42:243001, 2009.
- [103] M. A. Lone, A. M. Ross, J. S. Fraser, S. O. Schrieber, S. A. Kushneriuk, and W. N. Selander. Low energy ${}^7\text{Li}(p,n){}^7\text{Be}$ neutron source (CANUTRON). *Chalk River Nuclear Laboratories*, PASS-18-5-R:AECL-7413, 1982.
- [104] S. O. Schriber, M. A. Lone, B. G. Chidley, M. S. de Jong, S. A. Kushneriuk, and W. N. Selander. A compact neutron source for research and industrial applications. *IEEE Trans. Nucl. Sci.*, NS-30:1668–1670, 1983.
- [105] M. A. Lone, A. J. Ferguson, and B. C. Robertson. Characteristics of neutrons from Be targets bombarded with protons, deuterons and alpha particles. *Nucl. Instr. Meth. Phys. Res.*, 189:515–523, 1981.
- [106] M. Drogg. Drogg-2000: Neutron source reactions. IAEA-NDS-87, 2001.

- [107] M. Matoš, A. Estradé, H. Schatz, D. Bazin, M. Famiano, A. Gade, S. George, W. G. Lynch, Z. Meisel, M. Portillo, A. Rogers, D. Shapira, A. Stolz, M. Wallace, and J. Yurkon. Time-of-flight mass measurements of exotic nuclei. *Nucl. Instr. Meth. Phys. Res. A*, 696:171–179, 2012.
- [108] A. M. Rogers, A. Sanetullaev, W. G. Lynch, M. B. Tsang, J. Lee, D. Bazin, D. Coupland, V. Henzl, D. Henzlova, M. Kilburn, M. S. Wallace, M. Youngs, F. Delaunay, M. Famiano, D. Shapira, K. L. Jones, K. T. Schmitt, and Z. Y. Sun. Tracking rare-isotope beams with microchannel plates. *Nucl. Instr. Meth. Phys. Res. A*, 795:325–334, 2015.
- [109] J. D. Bowman and R. H. Heffner. A novel zero time detector for heavy ion spectroscopy. *Nucl. Instr. Meth. Phys. Res.*, 148:503–509, 1978.
- [110] R. H. Kraus Jr., D. J. Vieira, H. Wollnik, and J. M. Wouters. Large-area fast-timing detectors developed for the TOFI spectrometer. *Nucl. Instr. Meth. Phys. Res. A*, 264:327–332, 1988.
- [111] T. Odenweller, H. Noll, K. Sapotta, R. E. Renfordt, and R. Bass. A gridless position sensitive time-zero detector for heavy ions. *Nucl. Instr. Meth. Phys. Res.*, 198:263–267, 1982.
- [112] T. K. Steinbach, M. J. Rudolph, Z. Q. Gosser, K. Brown, B. Floyd, S. Hudan, R. T. deSouza, J. F. Liang, D. Shapira, and M. Famiano. Measuring the fusion cross-section of light nuclei with low-intensity beams. *Nucl. Instr. Meth. Phys. Res. A*, 743:5–13, 2014.
- [113] T. K. Steinbach, J. Vadas, J. Schmidt, C. Haycraft, S. Hudan, R. T. deSouza, L. T. Baby, S. A. Kuvin, I. Wiedenhöver, A. S. Umar, and V. E. Oberacker. Sub-barrier enhancement of fusion as compared to a microscopic method in $^{18}\text{O} + ^{12}\text{C}$. *Phys. Rev. C*, 90:041603(R), 2014.

- [114] T. K. Steinbach. *Near and sub-barrier fusion of neutron-rich oxygen and carbon nuclei using low-intensity beams*. PhD thesis, Indiana University, 2016.
- [115] Varinderjit Singh, J. Vadas, T. K. Steinbach, B. B. Wiggins, S. Hudan, R. T. deSouza, Zidu Lin, C. J. Horowitz, L. T. Baby, S. A. Kuvin, Vandana Tripathi, and I. Wiedenhöver. Fusion enhancement at near and sub-barrier energies in $^{19}\text{O} + ^{12}\text{C}$. *Phys. Lett. B*, 765:99–103, 2017.
- [116] Master Magnetics, Inc., 2017. URL www.magnetsource.com.
- [117] R. T. deSouza, A. Alexander, K. Brown, B. Floyd, Z. Q. Gosser, S. Hudan, J. Poehlman, and M. J. Rudolph. Sub-nanosecond time-of-flight for segmented silicon detectors. *Nucl. Instr. Meth. Phys. Res. A*, 632:133–136, 2011.
- [118] M. Saito, Y. Saito, and K. Asamura. Spatial charge cloud size of microchannel plates. *Rev. Sci. Instrum.*, 78:023302, 2007.
- [119] A. S. Tremsin and O. H. W. Siegmund. Spatial distribution of electron cloud footprints from microchannel plates: Measurements and modeling. *Rev. Sci. Instrum.*, 70:3282–3288, 1999.
- [120] SIMION, 2017. URL <http://www.simion.com>.
- [121] Alpha Lab, Inc., DC Gaussmeter GM1-ST, 2017. URL <http://www.trifield.com/content/dc-gaussmeter-model-gm1-st/>.
- [122] D. R. Beaulieu, D. Gorelikov, P. de Rouffignac, K. Saadatmand, K. Stenton, N. Sullivan, and A. S. Tremsin. Nano-engineered ultra-high-gain microchannel plates. *Nucl. Instr. Meth. Phys. Res. A*, 607:81–84, 2009.
- [123] V. T. Jordanov and G. F. Knoll. Digital synthesis of pulse shapes in real time for high resolution radiation spectroscopy. *Nucl. Instr. Meth. Phys. Res. A*, 345:337–345, 1994.

- [124] V. T. Jordanov, G. F. Knoll, A. C. Huber, and J. A. Pantazis. Digital techniques for real-time pulse shaping in radiation measurements. *Nucl. Instr. Meth. Phys. Res. A*, 353:261–264, 1994.
- [125] V. Radeka. Trapezoidal filtering of signals from large germanium detectors at high rates. *Nucl. Instr. Meth. Phys. Res. A*, 99:525–539, 1972.

Bryan Blake Wiggins

Department of Chemistry and Center for Exploration of Energy and Matter

Indiana University, Bloomington, IN 47408

brywiggi@indiana.edu

EXECUTIVE SUMMARY

PhD graduate seeking a position involving construction and development of detectors. Analytical chemist specialized in detector development, engineering, and digital-signal processing. Experienced in developing a novel imaging detector from start to finish.

EDUCATION

- Ph.D. Analytical Chemistry, Graduation: December 2017
Indiana University, Bloomington, IN
Research Advisor: Dr. Romualdo T. deSouza
Thesis: "Using Induced Signals to Develop a Position-Sensitive Microchannel Plate Detector"
- B.S. Chemistry, 2012
Georgia Southern University, Statesboro, GA
Research Advisor: Dr. Brian Koehler
Thesis: "Variation in Lachrymatory Factor and Certain Other Compound between Layers in Yellow Onion"

EXPERIENCE

PhD – Analytical Chemistry

June 2012 – December 2017

Indiana University, Bloomington, IN

Designed, constructed, and characterized a novel 2D imaging detector (microchannel plate or MCP based technology).

Employed digital-signal processing techniques to optimize the detector readout and achieve a spatial resolution of 98 μm FWHM.

Undergraduate Research Associate

Oct. 2010 - May 2012

Georgia Southern University, Statesboro, GA

Performed a flavor-profile analysis on *Allium cepa*.

Used gas chromatography (GC-MS and GC-FID) to study the chemistry associated with onion flavor.

Supplemental Instructor

Sept. 2011 – May 2012

Georgia Southern University, Statesboro, GA

Lead a discussion course for general chemistry.

Sales Associate

Apr. 2008 – July 2010

Polk's Fresh Market Savannah, GA

Worked in most aspects of the company: cashier, catering services, and store setup

TECHNICAL SKILLS

Laboratory

- Detector development for position-sensitive MCP detectors: novel induced signal approach, resistive anode, multi-anode, ExB Detector coupled to a multi-anode
- Electronics: NIM, VME, CAMAC, PCIE
- Detector Operation: microchannel plates, surface barrier detectors, plastic scintillators and photomultiplier tubes, gas-ionization chambers, annular silicon detectors
- Ultra-high vacuum techniques
- Separations: GC-MS, GC-FID
- Programs: Mastercam (CAD), SpecTcl, SIMION, SRIM, Adobe Photoshop, PeakSimple
- Machining

Computer

- Programing: ROOT, C++, LabVIEW, and LaTeX
- CAD: Mastercam
- Programs: SpecTcl, SIMION, SRIM, Video Copilot, Adobe Photoshop, PeakSimple

HONORS AND AWARDS

| | |
|--------------------------------------------------------------|-------------|
| Outstanding Poster Award, SSAP Symposium | 2015 |
| Undergraduate Analytical Chemistry Award, ACS | 2012 |
| Honors Program Research Stipend, Georgia Southern University | 2011 |
| Honors Program, Georgia Southern University | 2009 - 2012 |
| Zell Miller scholarship | 2009 - 2012 |

SUPERVISORY EXPERIENCE

Directly Supervised 1 *Undergraduate Student*, Indiana University, 2017.
Directly Supervised 1 *High School Intern*, Indiana University, 2015 – 2017.
Directly Supervised 2 *Undergraduate Students*, Indiana University, 2015.
Directly Supervised 1 *Undergraduate Student*, Indiana University, 2014.
Directly Supervised 1 *High School Intern*, Indiana University, 2014.

PROFESSIONAL OUTREACH

| | |
|-------------------------------------------------------------------------------------------------------------|---------------------|
| <u>Tour Guide of the Center for Exploration of Energy and Matter</u> Indiana University, Bloomington, IN | Feb. 2013 - Present |
| <u>Discussion Leader</u> Gordon Research Seminar, New London, NH | June 18, 2017 |

PROFESSIONAL AFFILIATIONS

American Chemical Society
American Physical Society

TEACHING

| | |
|-------------------------------------------------------------------------------------|-------------|
| “Nuclear Chemistry” (Discussion), Indiana University | Fall 2016 |
| “Nuclear Chemistry” (Discussion), Indiana University | Fall 2014 |
| “Bioanalytical Chemistry” (Lab), Indiana University | Spring 2013 |
| “Principles of Chemistry and Biochemistry II” (Discussion), Indiana University | Fall 2012 |
| “Principles of Chemistry for Engineers (Discussion), Georgia Southern University | Spring 2012 |
| “Principles of Chemistry for Engineers (Discussion), Georgia Southern University | Fall 2011 |

PUBLICATIONS

Refereed Journals

1. Slow neutron radiography with induced signals in a microchannel plate detector, B. B. Wiggins and R. T. deSouza, *Nucl. Instr. Meth. In Phys. Res. A* (In Preparation).
2. Probing the fusion of neutron-rich nuclei with re-accelerated radioactive beams, J. Vadas, Varinderjit Singh, B. B. Wiggins, J. Huston, S. Hudan, R. T. deSouza, Z. Lin, C. J. Horowitz, A. Chbihi, D. Ackermann, M. Famiano, and K. Brown, *PRL* (Submitted 2017).
3. Achieving high spatial resolution using a microchannel plate detector with an economic and scalable approach, B. B. Wiggins, Z. O. deSouza, J. Vadas, A. Alexander, S. Hudan, and R. T. deSouza, *Nucl. Instr. Meth. In Phys. Res. A872, 144* (2017). <https://doi.org/10.1016/j.nima.2017.08.032>
4. Development of a compact ExB microchannel plate detector for beam imaging, B. B. Wiggins, Varinderjit Singh, J. Vadas, J. Huston, T. K. Steinbach, S. Hudan, and R. T. deSouza, *Nucl. Instr. Meth. In Phys. Res. A866, 202* (2017). <https://doi.org/10.1016/j.nima.2017.06.006>
5. Fusion Enhancement at near and sub-barrier energies in $^{19}\text{O} + ^{12}\text{C}$, Varinderjit Singh, J. Vadas, T.K. Steinbach, B.B. Wiggins, S. Hudan, R.T. deSouza, Zidu Lin, C.J. Horowitz, L.T. Baby, S.A. Kuvin, Vandana Tripathi, I. Wiedenhover, A.S. Umar, *Phys. Lett. B765, 99* (2017). <http://dx.doi.org/10.1016/j.physletb.2016.12.017>
6. High-rate axial-field ionization chamber for particle identification of radioactive beams, J. Vadas, Varinderjit Singh, G. Visser, A. Alexander, S. Hudan, J. Huston, B. B. Wiggins, A. Chbihi, M. Famiano, M.M. Bischak, R. T. deSouza, *Nucl. Instr. Meth. In Phys. Res. A837, 28* (2016). <http://dx.doi.org/10.1016/j.nima.2016.08.056>
7. Optimizing the position resolution of a Z-stack microchannel plate resistive anode detector for low intensity signals, B.B. Wiggins, E. Richardson, D. Siwal, S. Hudan, R.T. deSouza, *Rev. Sci. Instrum.* 86, 083303 (2015). <http://dx.doi.org/10.1063/1.4927457>

8. Using pulse shape analysis to improve the position resolution of a resistive anode microchannel plate detector, D. Siwal, B. B. Wiggins, R.T. deSouza, *Nucl. Instr. Meth. In Phys. Res.* A804, 144 (2015).
<http://dx.doi.org/10.1016/j.nima.2015.09.056>

Refereed Conference Proceedings

1. Sensing an electron cloud emanating from a microchannel plate stack, R.T. deSouza, B. B. Wiggins, D. Siwal, *Nuclear Science Symposium and Medical Imaging Confence*, IEEE Xplore (2015).
<http://dx.doi.org/10.1109/NSSMIC.2015.7581939>

INVITED TALKS

1. B. B. Wiggins and R.T. deSouza, “Sensing the position of a single electron using induced signals”; Georgia Southern University, Statesboro, GA, September 2016.

CONTRIBUTED PRESENTATIONS

1. B. B. Wiggins, J. Vadas, T. K. Steinbach, J. Huston, Z. deSouza, V. Singh, S. Hudan, R. T. deSouza, “Exploring the Spatial Resolution of Position-Sensitive Microchannel Plate Detectors”; Poster Presentation at the Gordon Research Conference, New London, NH, June 19-20, 2017.
2. B. B. Wiggins, Varinderjit Singh, T. K. Steinbach, J. Vadas, J. Huston, S. Hudan, R. T. deSouza, L. T. Baby, S. A. Kuvin, V. Tripathi, I. Wiedenhöver, “Probing the skin of neutron-rich light nuclei using low energy fusion reactions”; Keynote Session at the Gordon Research Seminar, New London, NH, June 17, 2017.
3. B. B. Wiggins, J. Vadas, T. K. Steinbach, J. Huston, Z. deSouza, V. Singh, S. Hudan, R. T. deSouza, “Exploring the Spatial Resolution of Position-Sensitive Microchannel Plate Detectors”; Poster Presentation at the Gordon Research Seminar, New London, NH, June 17, 2017.